DESIGN, FABRICATION, AND CHARACTERIZATION OF FIBROUS ACOUSTIC SENSORS FOR BIOACOUSTICS APPLICATIONS

LI WENBO

PhD

The Hong Kong Polytechnic University

2026

The Hong Kong Polytechnic University

School of Fashion and Textiles

Design, Fabrication, and Characterization of Fibrous Acoustic Sensors for Bioacoustics Applications

Li Wenbo

A thesis submitted in partial fulfillment of the requirements for

the degree of Doctor of Philosophy

August 2025

CERTIFICATE OF ORIGINALITY

I hereby declare that this thesis is my own work and that, to the best of my knowledge and belief, it reproduces no material previously published or written, nor material that has been accepted for the award of any other degree or diploma, except where due acknowledgement has been made in the text.

_____ (Signed)

____Li Wenbo____ (Name of student)

Abstract

Audible sound, spanning 20–20 kHz, is one of the most fundamental forms of human perception and communication, with applications extending from diagnostics and human-machine interaction to voice recognition. The rapid miniaturization and integration of microelectronics have fueled the growth of wearable electronics, enabling continuous physiological monitoring, personalized diagnostics, and seamless data acquisition. Within this context, acoustic sensing has become a key modality for health monitoring due to its ability to non-invasively capture subtle physiological vibrations. However, current wearable acoustic sensors face significant challenges, including limited sensitivity, mechanical mismatch between rigid electrodes and soft substrates, compromised comfort during prolonged wear, and instability or poor repeatability of physiological signal acquisition under dynamic conditions.

This work addresses these limitations by developing a flexible, low-density, anisotropic electrospun piezoelectric nanofiber membrane integrated into a shape-adaptive wearable acoustic sensor with high sensitivity, broad frequency response, and mechanical robustness. Using PVDF-TER as the flexible polymer matrix and incorporating BTO nanoparticles, highly aligned nanofibers with strong dipole orientation were fabricated via controlled electrospinning. The synergistic effects of BTO-induced heterogeneous nucleation and interfacial polarization increased the all-trans (*TTTT*) phase content to approximately 92%, yielding a piezoelectric constant d_{33} of –30.9 pC·N^{-1} and a transverse coefficient d_{31} of 45.5 pC·N^{-1}. The porous microstructure reduced the apparent dielectric constant, enabling a high g_{33} and

efficient electromechanical coupling while maintaining mechanical compliance suitable for skin-conformal applications.

To overcome the limitations of rigid electrodes, a conformal and durable silver nanowires (AgNWs) network was deposited via solution electrospraying. This flexible electrode maintained stable conductivity even after 10,000 bending cycles, demonstrating superior fatigue resistance commred to sputtered metallic electrodes. A multilayer diaphragm-cavity architecture was then designed to enhance acoustic impedance matching and amplify low-frequency response while preserving lightweight comfort. Initial prototypes achieved a flat frequency response across 20–600 Hz, with a sensitivity of approximately 47 $mV \cdot Pa^{-1}$.

To further broaden the bandwidth, a hybrid hard-soft clamping strategy was implemented to significantly increase the effective boundary stiffness of the diaphragm. This structure clarified boundary vibrations and extended the frequency response up to 1 kHz. Calibrated acoustic tests showed a low-frequency sensitivity of 76.6 $mV \cdot Pa^{-1}$ at 150 Hz, and a relatively flat mid-to-high frequency response averaging 36 $mV \cdot Pa^{-1}$, with stable dynamic performance across a 50–90 dB SPL range and high signal-to-noise ratio (SNR).

In vivo evaluations demonstrated the sensor's capability for high-fidelity physiological signal acquisition. Pulse monitoring produced stable amplitudes with distinct pulse-wave features, while heart sound detection enabled clear identification of the first and second heart sounds (S1 and S2) and the observation of S2 splitting. Lung sound

measurements captured broadband energy distributions with dominant frequencies between 100–800 Hz, consistent with clinical auscultation standards.

This research establishes a scalable design and fabrication framework for high-performance, wearable piezoelectric acoustic sensors, integrating optimized electrospun membranes, flexible electrodes, and shape-adaptive device architectures. The acoustic system offers high sensitivity, broad frequency coverage, mechanical durability, and environmental stability, demonstrating strong potential for continuous, reliable bioacoustic monitoring in personalized healthcare and intelligent wearable systems.

Publications

Referred Journal Paper

1. Advances in Bioacoustics Sensing and Signal Processing Technologies. Under review.
2. A Skin-Conformal Piezoelectric Acoustic Sensor Based on Electrospun Nanowebs for Bioacoustics Monitoring. To be submitted.

Referred Conference Papers

Oral Presentation

Wenbo LI, Jingyang WU, Chengyu LI, Xiaoming TAO. Design, Fabrication, and Characterization of Fibrous Acoustic Sensing Membranes for Biomedical Applications. The Fiber Society's Spring 2025 Conference, May 21–23, 2025, Hong Kong.

Acknowledgements

Time flies, and now it is finally my turn to write down my thoughts and gratitude in the acknowledgments section of my doctoral dissertation. Looking back on my entire PhD journey, from the initial curiosity and excitement when I first arrived at PolyU, to the struggles and confusion in the middle, and finally to the calmness I feel now as I write this, the process has been filled with countless tears and growth.

First and foremost, I would like to express my sincere gratitude to Professor Tao Xiaoming. Thank you for taking me into your group halfway through my program and for giving me the opportunity to continue my research under your guidance. Professor Tao is a true role model for me as a woman in science; from her, I have seen the possibilities of perseverance, dedication, and responsibility that transcend age. I am deeply grateful for her trust in allowing me to participate in the piezoelectric acoustic project. Throughout the implementation of this project, I have learned so much, devoted so much, and, at times, struggled deeply. I am truly thankful for Professor Tao's invaluable guidance and her directional advice, which, looking back, often proved to be pivotal in shaping the course of my work.

I would also like to thank Professor Chen Wei, who first recruited me and guided me at the start of this journey. Thank you for giving me this opportunity and for teaching me that in research, one must maintain a certain sharpness and persistence to develop independent insights and ideas.

My heartfelt thanks also go to the members of our acoustic project team, Dr. Li Chengyu

and Mr. Wu Jingyang. It is because of our mutual trust and seamless collaboration that this project was able to progress smoothly. I am especially grateful to Mr. Wu for his support in device simulation and design, and to Dr. Li for his generous help with signal acquisition and computational setups. My gratitude also extends to every member of Professor Tao's group. Thank you for welcoming me and helping me integrate so quickly into the team, which allowed me to carry out my experiments with confidence and efficiency. I would also like to thank my family and friends for their companionship, support, and encouragement throughout these years. You have given me so much help in my daily life and comforted me during my lowest moments, making the tough days of my PhD much warmer and more bearable.

Lastly, my deepest gratitude goes to my beloved husband, Dr. Zhao Zehao, and to my family. Thank you for your unconditional support, encouragement, and companionship, which have been the strongest foundation that allowed me to persevere through every challenge. Above all, I want to thank myself for enduring, for persisting, and for never giving up despite the hardships. I have crossed countless mountains to get here, and though the journey has been bitter and cold, it has also been deeply rewarding. Well done, Li Wenbo.

Table of Contents

List of Figures

Fig. 2.10 (a) Schematic of acoustic device with electrodes patterned on top and bottom surface of PVDF film. (b) Photograph of the PVDF sensor encapsulated in PDMS cylinder. (c) The sensitivity of PVDF acoustic device inside an air pressure chamber. Sound pressure was delivered at two levels (80 and 100 dB). Inset shows air pressure chamber.

Fig. 2.11 (a) Conceptual illustration of organ of Corti in mammalian cochlea. (b) Optical image of the frequency separator with PAS. The inset shows a single PAS unit conformally attached on cylinder. (f) A vibration displacement and a piezoelectric signal generated in the frequency range of 100–1600 Hz.

Fig. 2.12 The principle of electrospinning. (a) Basic setup of electrospinning. (b) A snapshot of an electrospinning jet with well-developed loops from the nozzle.

Fig. 2.13 Schematic illustrations of the preparation of aligned electrospun nanofibers (a) dynamic near-field electrospinning technique, (b) high-speed rotating drum.

Fig. 2.14 Schematic diagram of electrode integration. (a) metal coating, (b) metal plate, (c) magnetron sputtering, and (d) spray coating.

Fig. 2.15 Performance requirements and selection criteria for various bioacoustics sensors.

Fig. 2.16 (a) Lung Sound Auscultation Trainer "LUNG" ver.2, a mannequin simulator for lung sound auscultation. (b) Wireless acoustic monitoring systems for neonatal respiration and chronic pulmonary disease patients; (i) Monitoring respiratory sound

intensity in ten neonates in the neonatal intensive care unit (NICU) (ii) Comparative respiratory rate monitoring between healthy subjects and chronic pulmonary disease patients. (c) Comparison of signal amplitudes between soft acoustic sensors and rigid devices under static and dynamic conditions, demonstrating noise immunity and motion artifact suppression capabilities.

Fig. 3.1 Schematic diagram of fabrication of high-oriented nanofiber film via electrospinning.

Fig. 3.2 Schematic illustration of the tensile testing setup for determining the piezoelectric coefficient d_{31}.

Fig. 3.3 (a), (b), and (c) are typical morphology pictures via SEM of the nanofiber membranes with variable content of polymer solutions from 12% to 18%; (d), (e), and (f) are the oriented nanofibers with different collection speeds and humidity; (g), (h), and (i) are the diameter and distribution of the above corresponding nanofibers. (Scalebar: 50 μm)

Fig. 3.4 (a) The XRD spectrum of the nanofibers of PVDF-TER random, aligned membranes. (b) The FTIR spectrum of the PVDF-TER nanofibers with gradient-content BTO doping (from 0–24% doping ratio, 4% as gradient). (c) The calculated crystallization of β-phase content corresponding to the FTIR spectrum. (d) The DSC (heating rate of 10 K/min) curve of the pure PVDF-TER and PVDF-TER doping with 16% BTO electrospun membranes and corresponding calculated crystallinity. (e)

Schematic illustration of the BTO incorporation enhances the performance of composite piezoelectric polymers.

Fig. 3.5 (a) Schematic diagram of the coordinate axes for the PVDF-TER/BTO_{16} nanofiber film and a single fiber. (b) and (c) 2D GIWAX patterns with the incident X-ray beam parallel to and perpendicular to the fiber axis, respectively. (d) 1D GIWAX curve showing the 110/200 diffraction plane (β phase) of PVDF-TER and the tetragonal phase of the BTO nanoparticles.

Fig. 3.6 3D height (a) and tapping phase (b) of the PVDF-TER/BTO nanofibers characterized by atomic force microscopy (tapping， 5 μm × 5 μm). (c) The SEM image of the PVDF-TER/16%BTO membrane demonstrates the well-alignment of the nanofibers (Scalebar: 50 μm). (d) The enlarged image of nanofibers (Scalebar: 10 μm). The BTO (<99nm) nanoparticles are fully dispersed within the fibers. (e) and (f) are the EDS element analysis and related mapping of Barium.

Fig. 3.7 (a) The strain-stress curve of the various electrospun nanofibers from different tensile directions (parallel to and perpendicular to the fiber), and (b) the corresponding calculated Young's modulus. (compared with the dense commercial PVDF film under same thickness: 2.2 GPa).

Fig. 3.8 Schematic illustration (a) and photographs (b) of fiber electrode fabrication and encapsulation for the PVDF-TER/BTO electrospun film. (The twisted fiber in the optical picture shows its high flexibility.)

Fig. 3.9 The charge transfer versus the different tensile stress. (a) Low tensile stress region of 0–1.0 N. (b) High tensile stress region of 1.2–2.0 N. (c) Result of transferred charges versus applied tensile stress with the calculated dynamic sensitivity variations under low (blue) and high (pink) tensile stress region. (d) The comparison of d_{31} value of PVDF-TER/BTO nanofibers with other works and commercial PVDF films.

Fig. 3.10 (a) The optical image for measuring the piezoelectric coefficient. (b) PFM butterfly amplitude loop and (c) PFM phase of the nanofibers under a direct current (DC) bias ± 30V.

Fig. 3.11 (a) Periodic voltage output under different loads. (b) The variation of peak voltage with the applied force. (c) Voltage outputs at various frequencies (1–3 Hz) at a constant bending radius (10 mm) with varying fiber orientation angles (0°, 30°, 45°, and 90°) relative to stress direction. (d) Voltage outputs under different bending radii (5–15 mm) at various fiber orientations.

Fig. 4.1 Electrodes fabrication schematic diagram: (Left) silver nanowires (AgNWs) are deposited on electrospun film via electrospraying; (right) copper atoms are sputtered by magnetron sputtering on electrospun film.

Fig. 4.2 Fabrication process flow diagram of the device assembly.

Fig. 4.3 The full-scale acoustic chamber image for acoustic response testing (upper). Sound insulation from noise background: sound-absorbing cotton (thickness: 8 cm),

interference shielding with copper mesh grounding. Schematic illustration of the real-time acquisition system for acoustic testing (bottom).

Fig. 4.4 Effect of Triton X-100 concentration on the spreading behavior of AgNW ink on electrospun membranes. (a) Schematic illustration of the AgNWs ink formulation containing different concentrations of Triton X-100 applied onto an electrospun mat. (b) Contact angle (CA) images of AgNWs droplets with increasing Triton X-100 concentrations (0–0.1 wt%). (c) Time-resolved droplet profiles of 0.05 wt% TX-100-modified AgNW ink during spreading.

Fig. 4.5 Evaluation of surface conductivity and morphology of AgNWs electrodes with different Triton X-100 concentrations. (a–c) Real-time sheet resistance measurements of electrospun PVDF-based films with (a) AgNWs only, (b) AgNWs with 0.1% Triton X-100, and (c) AgNWs with 0.2% Triton X-100, respectively, measured under consistent conditions. (d–f) Corresponding optical microscopy images of the AgNWs layer on fiber surfaces from (a–c), demonstrating the improved uniformity and coverage with increasing Triton content. (g) Schematic illustration of the spreading behavior of AgNWs droplets during deposition.

Fig. 4.6 (a) I–V curves of AgNW-based electrodes under different bending radii (r = 2.0, 1.5, 1.0, and 0.5 cm). (b) SEM image of AgNW electrode after bending (r=0.5 cm). (c) I–V curves of Cu electrodes under various bending radii (same with AgNW-based electrodes). (d) SEM of Cu electrode after r = 0.5 cm bending.

Fig. 4.7 (a) Photographs of the cyclic bending test setup with a fixed curvature radius of 1.0 cm using a motorized bending apparatus. (b) Relative resistance change ($\Delta R/R_0$) of the AgNWs electrode over 10,000 bending cycles under a constant bending curvature. Inset: enlarged view of $\Delta R/R_0$ fluctuation during cycles 9000–9010, indicating stable and repeatable resistance response.

Fig. 4.8 (a) Schematic diagram showing the layered structure: TPU shell, PVDF-BTO piezoelectric layer, PU foam, vibration membrane, and silicone skin-contact layer. (b) Photographs of the assembled device: top view showing the key sensing unit integration and bottom view showing the full-scale device. (c) Measured total thickness of the integrated sensor (~7.4 mm) using a digital micrometer. (The color legend below indicates the material assignment of each structural layer).

Fig. 4.9 Modeling and experimental validation of cavity-backed coupling of the acoustic sensor. (a) Cross-section and COMSOL setup of the sensor showing the diaphragm and TPU frame forming the back cavity. (b) 3D concept of the top cover and back cavity. (c) Simulated frequency response: sound pressure at the device (SPL for device), at the diaphragm surface (SPL for vibration membrane), and the resulting gain (ratio), demonstrating passive amplification by the cavity. (d) Measured response: voltage sensitivity with and without the cavity and the derived gain.

Fig. 4.10 Time-domain comparison between the input sweep audio (20–1000 Hz) and the sensor output. (a): reference input audio waveform (5–25 s, A.U.). (b) sensor corresponding voltage output and FFT analysis (c).

Fig. 5.1 System schematic and hardware implementation of the wireless acoustic monitoring module. (a) Block diagram of the wireless multi-channel acoustic acquisition and transmission system. (b) Photograph of the assembled hardware module integrated with a rechargeable lithium battery, PCB board.

Fig. 5.2 Standard auscultation sites for pulmonary and cardiac acoustic signals. (a) Anterior view illustrating five classical auscultation points for heart sounds. (b) Posterior view showing eight standard auscultation sites for lung sounds.

Fig. 5.3 Simulation of modal displacement and electrical response with and without copper ring. (a, b) show the first and higher-order modes without the copper ring; (c, d) show the corresponding modes with the copper ring. (e) Simulated electrical output of the device under frequency sweep from 20–1000 Hz. The red curve represents the sensor with the copper ring, and the blue curve without it.

Fig. 5.4 Characterization of acoustic sensing performance. (a) Frequency-domain voltage output of the device under a broadband acoustic input (200–1000 Hz). (b) Frequency-dependent calculated sensitivity (mV/Pa), inset: enlarged sensitivity of frequency range 200–1000 Hz. (c) Time-domain and corresponding FFT process (d) voltage output in response to 94 dB sound signals at 200 Hz and 900 Hz. (e) Polar plot of directional sensitivity under sound incidence from different angles. (f) Output amplitude versus SPL ranging from 50 to 90 dB.

Fig. 5.5 Playback platform and reconstruction of physiological sounds. (a) PTFE chamber with an internal loudspeaker covered by a silicone membrane that emulates

skin motion; the sensor is placed on top to sense a mixture of airborne and structure-borne excitations. (b) A segment of normal heart sound was played back at 50 dBZ in the acoustic enclosure. The device output was recorded and compared with the original input. Time-domain traces (left) and STFT spectrograms (right).

Fig. 5.6 In-vivo recordings at three anatomical sites. Icons on top indicate sensor placement. (a) Chest placement. The blue segment corresponds to breath-hold and the orange segment corresponds to spontaneous breathing. (b) Neck placement. The inset zooms into one breathing cycle. (c) Wrist placement. The inset marks several pulse peaks P for heart rate and rhythm estimation.

Fig. 5.7 Cardiac sound detection and band separation in vivo. (a) Chest recording and three-band decomposition: original trace (top), respiratory component (≈0–0.4 Hz, green), pulse/BCG band (≈0–10 Hz, red), and heart-sound band (>20 Hz, blue). (b) Overlay of the bands. The heart-sound channel resolves S1–S2 pairs and shows an instance of S2 splitting during inspiration. (c) Zoomed segment of the heart-sound channel with S1 and S2 labels; example S1–S2 and S2–S1 intervals are indicated. (d) STFT spectrogram (0–200 Hz, color in dBV).

Fig. 5.8 In-vivo lung sound recording at the right middle lobe. (a) Time-domain signal from the chest: the blue trace is the raw voltage and the red trace is the same signal after a 100 Hz high-pass filter, which suppresses low-frequency chest motion while preserving the broadband lung component, and (b)corresponding STFT spectrogram. The noise floor is relatively flat with no strong tonal artifacts.

List of Tables

List of Abbreviations

PAS	Piezoelectric Acoustic Sensor(s)
FPAS	Flexible Piezoelectric Acoustic Sensor(s)
MEMS	Micro-Electro-Mechanical Systems
PVDF	Polyvinylidene Fluoride
P(VDF-TrFE)	Poly(vinylidene fluoride-co-trifluoroethylene)
P(VDF-TrFE-CFE)	Poly(vinylidene fluoride-co-trifluoroethylene-co-chlorotrifluoroethylene)
PVDF-TER	P(VDF-TrFE-CFE) Terpolymer
BTO	Barium Titanate ($BaTiO_3$)
PZT	Lead Zirconate Titanate
AgNWs	Silver Nanowires
CNTs	Carbon Nanotubes
rGO	Reduced Graphene Oxide
PDMS	Polydimethylsiloxane
TPU	Thermoplastic Polyurethane
PI	Polyimide (e.g., Kapton)
EVA	Ethylene-Vinyl Acetate
PC	Polycarbonate
Cu	Copper
SNR	Signal-to-Noise Ratio
SPL	Sound Pressure Level

FFT	Fast Fourier Transform
STFT	Short-Time Fourier Transform
SEM	Scanning Electron Microscope
FTIR	Fourier Transform Infrared Spectroscopy
EDS	Energy Dispersive X-ray Spectroscopy
XRD	X-ray Diffraction
DSC	Differential Scanning Calorimetry
GIWAXS	Grazing-Incidence Wide-Angle X-ray Scattering
AFM	Atomic Force Microscopy
PFM	Piezoelectric Force Microscopy
PVD	Physical Vapor Deposition
COMSOL	COMSOL Multiphysics (Simulation Software)
DAQ	Data Acquisition
NI	National Instruments
INA	Instrumentation Amplifier
MCU	Microcontroller Unit
HMI	Human-Machine Interaction
IoT	Internet of Things
RFE	Relaxor Ferroelectric Behavior
MWS	Maxwell-Wagner-Sillars (interfacial polarization)
EDLC	Electric Double-Layer Capacitor / Formation

PML	Perfectly Matched Layer (simulation boundary condition)
EMI	Electromagnetic Interference
NICU	Neonatal Intensive Care Unit
COPD	Chronic Obstructive Pulmonary Disease
S1	First Heart Sound
S2	Second Heart Sound
UT	Upstroke Time (pulse wave analysis)
%MAP	Normalized Mean Arterial Pressure (index, pulse wave analysis)
PCB	Printed Circuit Board
IMU	Inertial Measurement Unit
PC	Personal Computer
FDM	Fused Deposition Modeling (3D Printing)
UV	Ultraviolet

CHAPTER 1 INTRODUCTION

1.1 Research Background

Audible sound, spanning the range of 20–20 kHz, is one of the most fundamental media of human perception and communication, playing an irreplaceable role in healthcare, human-machine interaction, and environmental sensing.[1, 2] Over the years, the perception and utilization of sound have advanced dramatically, moving beyond traditional applications in communication to modern fields such as real-time diagnostics and intelligent interfaces. With the rapid miniaturization and integration of microelectronics, wearable electronics have emerged as transformative platforms, enabling continuous physiological monitoring, personalized diagnostics, and seamless data acquisition.[3-5] The widespread availability of smartphones, advances in ergonomic design, and demand for lightweight, compact, and high-performance sensors have further accelerated the growth of wearable technologies. In this context, acoustic sensors, capable of detecting low-level physiological sounds such as heartbeats, respiratory patterns, and gastrointestinal activity, are becoming increasingly important. This progress brings new challenges to acoustic sensors, which must meet stringent requirements for miniaturization, flexibility, and reliability.[6-8]

The evolution of acoustic sensors reflects these changing demands. From traditional carbon microphones to miniaturized MEMS-based devices and, more recently, to flexible thin-film and textile-based acoustic sensors, each development stage has expanded the possibilities of bioacoustic applications. In particular, the integration of

acoustic sensors with soft and conformable substrates made it possible to design skin-adaptive, unobtrusive devices capable of detecting subtle physiological sounds such as heartbeats, respiratory sounds, and bowel sounds.[8, 9] These physiological signals typically occur in low-frequency ranges, often below 1 kHz, and at relatively low sound pressure levels, typically between 30 and 60 dB.[10-12] Such characteristics place high demands on both the sensitivity and frequency bandwidth of wearable sensors to ensure reliable and high-fidelity monitoring in diverse and dynamic conditions.

Piezoelectric materials have emerged as one of the most promising solutions for wearable acoustic sensing. Their intrinsic ability to directly convert mechanical energy into electrical signals allows for self-powered operation, while their broad bandwidth and rapid response enable accurate capture of complex sound signals.[13, 14] Among these, poly(vinylidene fluoride) (PVDF) and its copolymers have gained considerable attention due to their combination of flexibility, biocompatibility, and ease of processing, making them naturally compatible with wearable applications.[15] When processed into fibrous membranes via electrospinning[16, 17], these polymers exhibit highly aligned nanofiber architectures with high β-phase content, low modulus, and strong in-plane and out-of-plane piezoelectric coupling. These characteristics enhance their electromechanical response while maintaining the softness and conformability necessary for intimate skin integration, allowing precise detection of subtle physiological vibrations during long-term use.

Despite these inherent advantages, several challenges still hinder the full potential of

wearable piezoelectric acoustic sensors in real-world applications. The piezoelectric coefficients and electromechanical coupling factors of polymer-based films remain significantly lower than those of ceramic materials, which limits the sensitivity and fidelity of the output signals. Moreover, the longitudinal piezoelectric mode overlooks the transverse working mode, which is more sensitive to surface vibrations and plays a critical role in acoustic signal transduction. At the device level, the integration of rigid metallic electrodes with soft electrospun substrates introduces mechanical mismatch, leading to cracking, delamination, or loss of conductivity during repeated bending or prolonged deformation. These failures compromise signal stability and long-term durability. Additionally, existing packaging and device designs often prioritize protection and structural rigidity over comfort and adaptability, reducing wearability during extended use. Beyond these material and structural issues, the non-stationary and highly variable nature of physiological sounds-along with susceptibility to motion artifacts and ambient noise-further complicates consistent and reproducible signal acquisition.

This thesis addresses these challenges through a comprehensive strategy that integrates material innovation, electrode design, and structural optimization. By enhancing dipole alignment through electrospinning and incorporating ceramic nanoparticles, anisotropic nanofiber membranes with high crystallinity and directional sensitivity are developed as the core sensing unit. The fabrication of a flexible silver nanowire electrode via electrospraying ensures strong adhesion, low resistance, and excellent fatigue resistance under cyclic deformation, overcoming the limitations of rigid electrodes. At

the device level, multilayer diaphragm-cavity architecture is engineered to enhance acoustic impedance matching and low-frequency amplification of the acoustic sensor while maintaining comfort, ensuring stable operation even during long-term wear. Finite element modeling is employed to analyze acoustic-mechanical interactions within the device, guiding the optimization of its resonance modes and frequency response.

Comprehensive acoustic characterization demonstrates the high sensitivity, wide bandwidth, and stable dynamic range of the developed devices under standardized conditions, while durability testing under varied humidity, temperature, and mechanical fatigue confirms their reliability in real-world environments. Finally, in vivo evaluations validate the ability of the sensors to capture high-fidelity physiological signals, including heart sounds, lung sounds, and bowel sounds, enabling their potential application in continuous, non-invasive health monitoring.

Overall, this work establishes a high-sensitivity, flexible, and durable system for wearable acoustic sensing, providing a scalable framework for next-generation health monitoring technologies. By addressing the limitations of piezoelectric polymers through materials engineering and structural design, and by integrating flexible electrodes and adaptive device architectures, this research not only enhances performance and reliability but also lays the groundwork for the development of multi-modal, textile-integrated, and intelligent wearable systems for advanced biomedical applications.

1.2 Problem Statement

Wearable acoustic sensors hold significant potential for next-generation health monitoring devices. Although wearable sensing technologies have advanced considerably over the past decade, they are still in the early stages of development compared with mature commercial electronic devices. For practical applications, wearable acoustic sensors must simultaneously deliver high sensitivity, wide frequency response, mechanical flexibility, and long-term stability**,** while maintaining comfort and conformability for daily, long-duration use. Achieving these multifunctional requirements remains a major challenge. Another critical issue lies in the integration and adaptability of sensing components. Most current acoustic sensors are designed as rigid, stand-alone modules that are difficult to integrate seamlessly into textiles or flexible substrates, limiting their applicability in wearable platforms. Based on these challenges, the primary research problems addressed in this thesis are summarized as follows:

1. **Insufficient durability and stability in practical applications**

   For wearable health monitoring, acoustic sensors are required to maintain reliable performance under continuous mechanical deformation, cyclic fatigue, and diverse environmental conditions, including variations in humidity and temperature. However, current studies rarely address these critical factors. In particular, the long-term mechanical and electrical stability of flexible electrodes, which are essential for maintaining consistent signal transduction under bending, stretching, and

repeated dynamic loading, remains underexplored. Delamination, microcracking, or resistance drift of the electrode layers often leads to degraded sensitivity and unreliable outputs during prolonged operation. This lack of systematic evaluation of the device's durability including fatigue behavior, interfacial adhesion between the piezoelectric layer and the flexible electrode, and signal consistency under complex environmental stresses hampers the establishment of design guidelines for practical, wearable applications. Therefore, there is an urgent need to develop acoustic sensors with mechanically robust, environmentally resilient, and electrically stable architectures, ensuring consistent performance and durability in real-world conditions.

2. Inherent limitations of polymer-based piezoelectric materials

PVDF and its copolymers are widely used in acoustic sensors due to their flexibility, biocompatibility, and facile processability and self-powering. However, their relatively low piezoelectric coefficients and electromechanical coupling factors, compared to ceramic-based materials, significantly limit their sensitivity and signal fidelity. Moreover, most studies primarily focus on the longitudinal piezoelectric response (d_{33}) while overlooking the transverse piezoelectric effect (d_{31}), which is critical for accurately capturing complex acoustic vibrations in wearable applications. Therefore, acoustic sensors designed to operate in the in-plane piezoelectric mode, owing to their superior sensitivity to vibration, offer enhanced potential for achieving high-performance wearable acoustic sensing.

3. **Limited integration and wearability of conventional acoustic sensors**

Current acoustic sensors primarily rely on the piezoelectric effect to convert sound waves into electrical signals and are typically fabricated as independent electronic modules. While they are widely applied in medical and health monitoring fields, their reliance on external devices for data acquisition and processing restricts their portability and integration into wearable platforms. Although the emergence of acoustic fabrics offers enhanced wearability and comfort, enabling integration into clothing or daily-use textiles for continuous physiological monitoring, the development of fibrous acoustic sensors that maintain high sensitivity and a broad frequency response remains limited.

1.3 Research Objectives

This work aims to develop a next-generation acoustic sensor based on electrospun piezoelectric fibrous membranes for bioacoustics applications. By coupling the longitudinal (d_{33}) and transverse (d_{31}) piezoelectric working modes, the proposed sensor is designed to sensitively detect weak physiological acoustic signals with aimed frequency bandwidth, while maintaining flexibility, durability, and wearability for continuous health monitoring. To address the current limitations of conventional sensors such as low sensitivity, insufficient electrode stability, and poor environmental adaptability, the following specific objectives are proposed: 1) constructing stable flexible, high piezoelectric sensing elements; 2) designing the wearable acoustic device; 3) investigating performance and practical validations for reliability devices.

1. Design, fabricate, and characterize electrospun PVDF-based composite membranes doped with piezoelectric ceramics, featuring high fiber alignment, low density, enhanced piezoelectric performance, coupled in-plane and out-of-plane working modes, and excellent mechanical compliance, to ensure reliability as acoustic sensing units.
2. Integrate flexible, conformal, and bend-resistant AgNW electrodes with the electrospun membranes to ensure stable electromechanical transduction. These optimized sensing units are then assembled into cavity-coupled, shape-adaptive acoustic devices to achieve enhanced low-frequency amplification, wearability, and operational reliability.
3. Enhance the performance and bandwidth of the acoustic sensors by introducing a hybrid soft-rigid boundary design to achieve precise vibration control while maintaining comfort. A series of standardized evaluations will be conducted to assess dynamic response, frequency bandwidth, signal-to-noise ratio, and sensitivity. Finally, real physiological signal monitoring will be performed to validate practical feasibility and identify remaining challenges for future wearable health-monitoring applications.

1.4 Research Methodology

To address the identified research problems, this work adopts the following methodology:

M1: Fabrication and optimization of high orientation electrospun piezoelectric

fibrous membranes.

Electrospinning is employed to prepare piezoelectric fibrous membranes to enhance piezoelectric performance. The spinning parameters, including solution concentration, voltage, and collector design, are systematically optimized to achieve high fiber alignment, porous structure, and high β-phase crystallinity. These features provide superior in-plane and out-of-plane piezoelectric coupling, high sensitivity, and excellent mechanical compliance for wearable acoustic applications. Morphological, structural, and electrical properties are analyzed through SEM, XRD, FTIR, and PFM to establish the structure–property relationships.

M2: Integration of flexible, stable, and conductive AgNW electrodes.

Electrospraying techniques are used to deposit conformal silver nanowire (AgNW) electrodes on the electrospun membranes. The electrode layer is optimized for low sheet resistance, strong adhesion, and high flexibility, ensuring reliable signal transduction during repeated bending and dynamic loading. Mechanical stability, fatigue resistance, and long-term electrical reliability of the integrated electrodes are systematically evaluated under cyclic deformation and environmental stress conditions.

M3: Design and assembly of low frequency shape-adaptive acoustic devices.

A multilayer diaphragm-cavity-sensor structure is developed to achieve low-frequency amplification and enhanced acoustic coupling. The design includes a soft outer diaphragm for skin conformability and an air cavity to amplify acoustic signals, while

maintaining a compact, wearable configuration. Structural parameters such as diaphragm thickness, cavity dimensions, and boundary stiffness are tuned for optimal frequency response and signal fidelity.

M4: Simulation and modeling for structural optimization.

Finite element modeling (FEM) using COMSOL Multiphysics is performed to analyze the acoustic–mechanical interactions within the device. The simulations evaluate membrane displacement, cavity resonance modes, and sound pressure amplification under different boundary conditions. The modeling results guide the design optimization for broadband response and high sensitivity.

M5: Performance characterization and physiological signal validation.

The acoustic sensors are comprehensively characterized using standardized sound pressure tests to evaluate sensitivity, frequency response, dynamic range, and signal-to-noise ratio. Environmental stability tests are conducted to examine the effects of humidity and temperature variations. Finally, the sensor performance is validated by real-world physiological signal acquisition, including heart sounds, breath sounds, and other biomedical acoustic signals, to assess practical applicability and reliability for long-term wearable monitoring.

1.5 Research Significance

Developing wearable acoustic sensors with high sensitivity, flexibility, and long-term stability is critical for continuous physiological signal monitoring. Traditional

electronic stethoscopes often suffer from rigid form factors, poor skin conformity, and limited frequency response, which hinders their applicability in real-world, long-duration health tracking. In contrast, flexible acoustic sensing devices offer promising potential for non-invasive, comfortable, and real-time health monitoring applications. This thesis explores the design, fabrication, and evaluation of a shape-adaptive piezoelectric acoustic sensor based on electrospun fiber films, and delivers the following key outcomes:

1. A high-performance piezoelectric nanofiber membrane with enhanced β-phase content, mechanical softness, and anisotropic alignment. The electrospun PVDF-based film achieves superior piezoelectric output and mechanical compliance, enabling sensitive detection of weak acoustic signals. Compared to traditional dense PVDF films, the porous, fibrous structure ensures low modulus and improved conformability to skin surfaces, which is essential for wearable applications.
2. A flexible and robust electrode integrated using solution-based AgNW spraying, achieving stable conductivity (2.3Ω/sq) and mechanical durability. Unlike conventional sputtered metal electrodes, the sprayed AgNW network maintains reliable electrical contact under repeated bending (10,000+ cycles) and provides excellent adhesion to the nanofiber substrate. This approach supports low-cost, scalable fabrication of flexible sensing units.
3. A multilayer diaphragm-cavity-sensor architecture was designed to enhance acoustic coupling and directionality with the validation of Finite element simulations. The hybrid soft-rigid boundary design improves effective stiffness and

expands the frequency response bandwidth up to 1 kHz. The built-in air cavity also amplifies low-frequency sound pressure, enhancing signal amplitude in the 20–150 Hz range, which is critical for heart and lung sound monitoring.

4. The fabricated device demonstrated effective detection of real physiological signals including heartbeats and breath sounds. The sensor output shows high SNR, clear periodic features, and stable baseline under long-term wear. This confirms its practical potential for future wearable health-monitoring systems, especially for early disease screening and continuous monitoring.

1.6 Outlines of the Thesis

In this thesis, a shape-adaptive acoustic sensor was developed for physiological sound monitoring, featuring an anisotropic piezoelectric sensing unit integrated with flexible electrodes. The device exhibits high piezoelectric performance, mechanical flexibility, high sensitivity, and directional selectivity. This content is stated in six chapters and the main focal points are briefed as follows:

Chapter 1 introduces the background and significance of wearable acoustic sensors, emphasizing the necessity of physiological signal monitoring. It also states the existing problems in current technologies and provides a detailed account of the research objectives, methodologies, and significance.

Chapter 2 provides a comprehensive overview of the working principles and applications of current wearable acoustic sensors. It further reviews the development of piezoelectric materials, outlines the frontiers research in piezoelectric acoustic sensing,

and highlights the existing challenges and future development trends. In addition, the performance metrics relevant to acoustic sensing and the corresponding protocols for physiological evaluation are also discussed.

Chapter 3 focuses on the fabrication of high-performance piezoelectric films via electrospinning. Through systematic optimization of spinning parameters and polymer composition, electrospun nanofiber membranes with enhanced β-phase content and anisotropic fiber orientation were achieved. Key processing-structure-property relationships were investigated, including the influence of fiber alignment, porosity, and crystallinity on the piezoelectric output. The resulting films exhibit favorable mechanical compliance, high piezoelectric constant and voltage constant, and are suitable for integration into wearable acoustic sensing systems.

Chapter 4 presents the structural design and assembly of a flexible acoustic sensing device based on electrospun piezoelectric films. A silver nanowire-based conformal and conductive flexible electrode was integrated to ensure mechanical durability and signal stability. The device adopts a multilayer diaphragm-cavity architecture to enhance acoustic coupling and skin adaptability. Finite element simulation was conducted to investigate the acoustic-mechanical interactions within the device, confirming the amplification effect of the cavity structure in the low-frequency range.

Chapter 5 focuses on the mechanical optimization and functional evaluation of the acoustic sensing device. To address the limited frequency response in previous designs, a hybrid boundary strategy combining rigid and soft constraints was introduced to

enhance the effective stiffness of the vibrating membrane. This structural reinforcement significantly extended the device's response bandwidth. Standardized acoustic calibration demonstrated high sensitivity across a wide frequency range. Finally, the device was validated through real-time acquisition of physiological sounds, including heart and lung signals, confirming its potential for long-term wearable health monitoring.

Chapter 6 summarizes the key findings of this work while acknowledging the current limitations. It also outlines feasible directions for future development, including material optimization, structural integration, and potential applications in broader physiological monitoring scenarios.

CHAPTER 2 LITERATURE REVIEW

2.1 Definition and classification of acoustic sensors

Acoustic sensors are transducers that convert pressure fluctuations or particle motion in a medium (air, liquids, or solids) into measurable electrical signals (charge, voltage, current, resistance, or capacitance) for detection and analysis. They can be classified by transduction mechanism into capacitive, piezoresistive, triboelectric, and piezoelectric devices. Each mechanism presents distinct trade-offs in sensitivity, bandwidth, noise, power requirements, environmental stability, and form factor, so the optimal choice depends on the application context (from airborne sound and structural vibration to bioacoustics) (Table 2.1). The following subsections outline these mechanisms in turn and compare their performance, with particular attention to design choices relevant to wearable and biomedical sensing.

Piezoresistive effect

The working principle of piezoresistive acoustic sensors relies on the variation in electrical resistance of sensing materials in response to mechanically induced deformation caused by incident sound waves. Owing to their intrinsic flexibility and skin-conformability, these sensors are well-suited for capturing physiological signals such as vocal vibrations and laryngeal movements. The fundamental expression describing the relative resistance change is [18, 19]:

$$\frac{\Delta R}{R_0} = \varepsilon(1 + 2\nu) + \frac{\Delta \rho}{\rho} \quad (1)$$

where ε denotes the mechanical strain ($\Delta L/L_0$), ν is the Poisson's ratio of the material,

and the first term of the above equation accounts for geometrical deformation-induced resistance changes. The second term reflects changes in intrinsic resistivity, governed by modifications in the electronic properties of the material.[20]

Piezoresistive acoustic sensors exhibit considerable versatility in materials and structural design, as illustrated in **Fig. 2.1**. For instance, a 3D interlayered structure of bacterial cellulose and MXene on paper substrate (**Fig. 2.1a**) enhanced conductive contacts for high sensitivity under low pressure, though with limitations in humidity stability. A subsequent design using a PDMS elastomer embedded with MXene micro-pyramids **(Fig. 2.1b**) introduced dual geometric and electronic modulation, achieving broad bandwidth (0.1–3 kHz) and high SNR (up to 50 dB). In another approach, side-chain engineering of conjugated polymers **(Fig. 2.1c**) extended charge carrier lifetime and improved responsivity to weak acoustic stimuli, making such sensors ideal for voice interaction and emotion-aware systems.

The dominant resistance modulation mechanisms vary by material: metallic films use crack-based changes, semiconductors and polymers rely on electronic resistivity modulation, and nanoscale materials such as graphene or carbon nanotubes exploit quantum tunneling effects. Structural innovations from 1D fiber stacks and 2D micropatterned arrays to 3D molecularly tuned films enable high-fidelity acoustic transduction while maintaining flexibility. Despite challenges including humidity susceptibility, limited bandwidth, and durability, ongoing advances in multi-scale material and structural engineering are accelerating the adoption of piezoresistive

acoustic sensors in voice analytics, human-machine interfaces, and health monitoring systems.

Capacitive effect

Capacitive effect function by transducing mechanically induced vibrations from incident sound waves into periodic fluctuations in capacitance, thereby enabling acoustic perception and signal conversion.[21] The underlying working principle follows the classic parallel-plate capacitor model[22]:

$$C = \frac{\varepsilon_r \varepsilon_0 A}{d} \tag{2}$$

where ε_r is the relative permittivity of the dielectric medium, ε_0 is the vacuum permittivity, A is the effective overlapping area of the electrodes, and d is the interelectrode distance. When sound waves impinge on the diaphragm, the resulting mechanical deformation modulates d, causing cyclical changes in capacitance that encode the acoustic signal.

Conventional capacitive sensors are typically based on rigid Micro-Electro-Mechanical Systems (MEMS) architectures, comprising silicon substrates with air gaps as dielectric layers and metallic diaphragms serving as deformable electrodes.[23, 24] While widely adopted in commercial microphones, these structures suffer from brittleness and fabrication complexity, rendering them less suitable for emerging applications in flexible and wearable electronics. To address these limitations, research has increasingly shifted toward the development of flexible capacitive acoustic sensors, emphasizing the coupled optimization of deformable diaphragms[25, 26], compliant

electrodes[27-29], and soft dielectric layers.[30-32] As illustrated in **Fig. 2.1d–f**, several innovative strategies have emerged. A flexible electret-based sensor with a patterned porous diaphragm and elastomeric nanodroplet masses (**Fig. 2.1d**) achieved high sensitivity (2.2 V/Pa), flat frequency response from 80–3000 Hz, and very low power consumption by retaining permanent polarization, eliminating the need for an external bias. Another approach used a dielectric elastomer layer with interlocked microcone structures made of CNT-doped PDMS (**Fig. 2.1e**) to minimize viscoelastic and interfacial losses. This design enabled vibration detection beyond 10 kHz with 0.2 Hz resolution, making it suitable for artificial cochlea and high-fidelity sensing. For underwater and low-frequency applications, an ionic hydrogel-based sensor with a pyramid array dielectric (**Fig. 2.1f**) demonstrated a receiving sensitivity of –159.7 dB (20–125 Hz) and a minimum detectable pressure of 0.3 Pa by leveraging electric double-layer (EDL) formation and non-Faradaic junction effects.

Beyond these structural innovations, emerging dielectric materials such as high-permittivity polymers doped with conductive/ dielectric/magnetic fillers (e.g., CNTs@PDMS[33], $CaCu_3Ti_4O_{12}$@TPU[34]), ionic or fluidic gels[35, 36], and microporous aerogels[37, 38] have been introduced to enhance capacitive responsivity and suppress environmental interference. Additionally, gradient-wrinkled interfaces and microstructured elastomers have improved sensitivity and expanded the operational frequency range. For flexible electrode design, conductive polymers (e.g., PEDOT:PSS, AgNws, graphene, and CNTs have been widely integrated, offering excellent mechanical compliance, electrical stability, and long-term durability under dynamic

conditions. These advances collectively enable a new generation of skin-conformable, highly sensitive capacitive acoustic sensors for wearable bioacoustics monitoring.

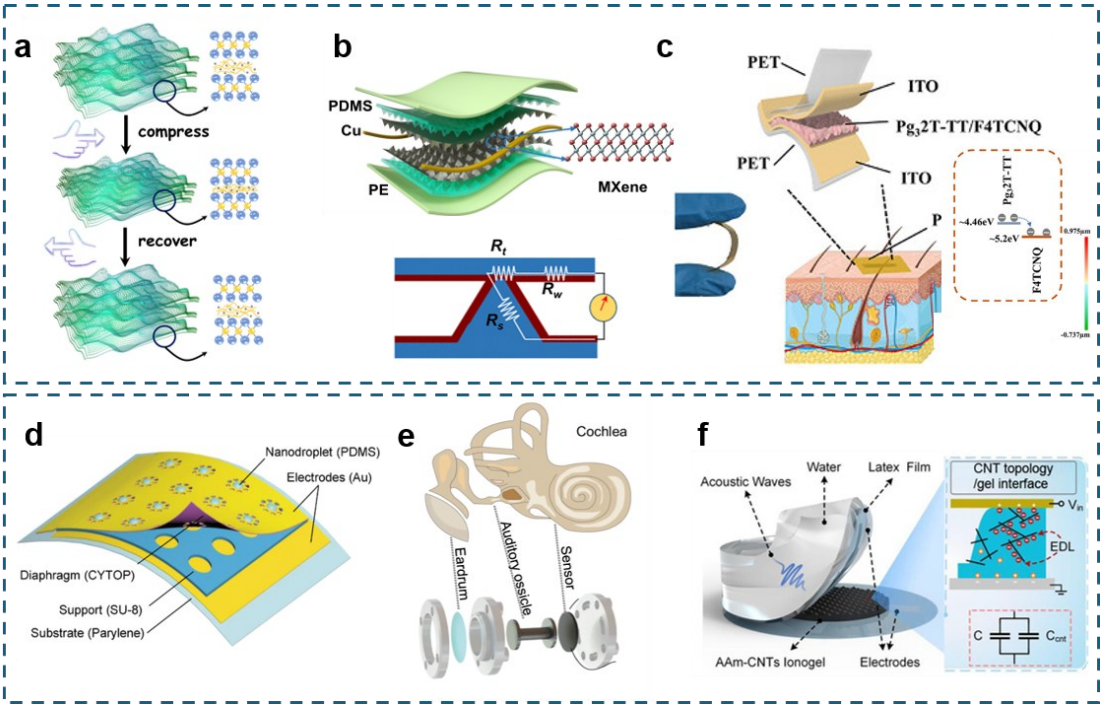

Fig. 2.1 Piezoresistive and capacitive acoustic sensors with various mechanisms and dielectrics. (a) Inner-microstructure changes of the MXene/BC film to construct conductive contact pathways. (b) Schematic illustration of the MXene eardrum device with micropyramid structure. The lower diagram is the equivalent circuit of the two-stage amplification piezoresistive sensor. (c) Schematic diagrams of the conjugated polymer sensor for speech sound recognition. The inset shows the electrons transfer between the HOMO-LUMO energy levels to increase the charge density of the film. (d) Diagram of skin-attachable electret-powered capacitive auditory sensor. (e) Schematic of the artificial system for sound detection using capacitive sensor with bonded interface structure. (f) An ionic gel-based hydrophone when sensing sound pressure. The inset is the sensing mechanism of CNTs topological network.

Triboelectric effect

In 2012, triboelectric nanogenerators (TENGs) were first demonstrated[39] and have enjoyed broad applications in wearable electronics and self-powered sensors,[40-43] owing to their fast response, high sensitivity, and potential for high integration.[44-47] The working principle of TENGs relies on the combined effects of triboelectrification and electrostatic induction.[39] Among the four basic working modes,[48] the contact-separation mode is the most widely employed, particularly in vibration energy harvesting and biomechanical energy conversion.[49-51] During the contact phase, two materials with differing electron affinities tend to contact under external mechanical force, generating opposite charges on their surfaces. When the materials are subsequently separated, a potential difference is created between the two electrodes due to the remaining surface charges. This drives electron flow through an external load, generating current. By repeating the contact and separation process, alternating current is produced. The resulting displacement current (J_D) can be expressed by introducing a surface polarization charge density (P_S),

$$J_D = \frac{\partial D}{\partial t} = \varepsilon \frac{\partial E}{\partial t} + \frac{\partial P_S}{\partial t} \quad (3)$$

where D is the displacement field, ε is the permittivity of the medium, E is the electric field, and P_S is the polarization attributed to surface polarization charges contributed from piezoelectric and or triboelectric effect.[52]

Recently, triboelectric acoustic sensors have gained momentum in bioacoustics field, particularly in applications such as voice recognition,[53, 54] human-machine

interaction (HMI),[47, 55] and health monitoring.[56, 57] These applications often rely on multilayer thin-film configurations with spacers to enable contact-separation modes, offering ultrabroadband frequency responses and high sensitivity. [58-60] However, the inherent rigidity and poor breathability of such structures limit their use in long-term wearable settings.[54, 61] To overcome these issues, flexible fibrous or textile-based triboelectric sensors have been developed, combining wearability with comfort without compromising performance. [62, 63]

As illustrated in **Fig. 2.2**, diverse structural strategies further enhance TENG acoustic sensors. Bioinspired surface microstructures such as conical micropillar arrays (**Fig. 2.2a**) increase the contact area and improve sensitivity within 50–80 dB. Internal material designs including core–shell microspheres and gradient porous composites (**Fig. 2.2b**) enable frequency selectivity across a broad band (e.g., 145–9000 Hz) and noise-robust operation. Furthermore, nanofiber-based systems **(Fig. 2.2c**) leverage electrospun mats with intrinsic air gaps to achieve high low-frequency sensitivity, ideal for capturing physiological acoustics like heartbeats. All-nanofiber sandwich configurations with built-in air gaps **(Fig. 2.2d**) achieve ultrahigh sensitivity (e.g., 10050.6 mV Pa^{-1} at low frequencies) and allow visualized acoustic-to-optical signal conversion. Moreover, wearable triboelectric textiles (**Fig. 2.2e**) offer high breathability and wide bandwidth (up to 5000 Hz) with excellent signal-to-noise ratio (e.g., 61 dB), ideal for real-world voice detection. In addition to macroscopic structural optimizations, micro/nanoscale engineering, such as surface morphology control and internal material tuning, is essential for enhancing triboelectric performance.

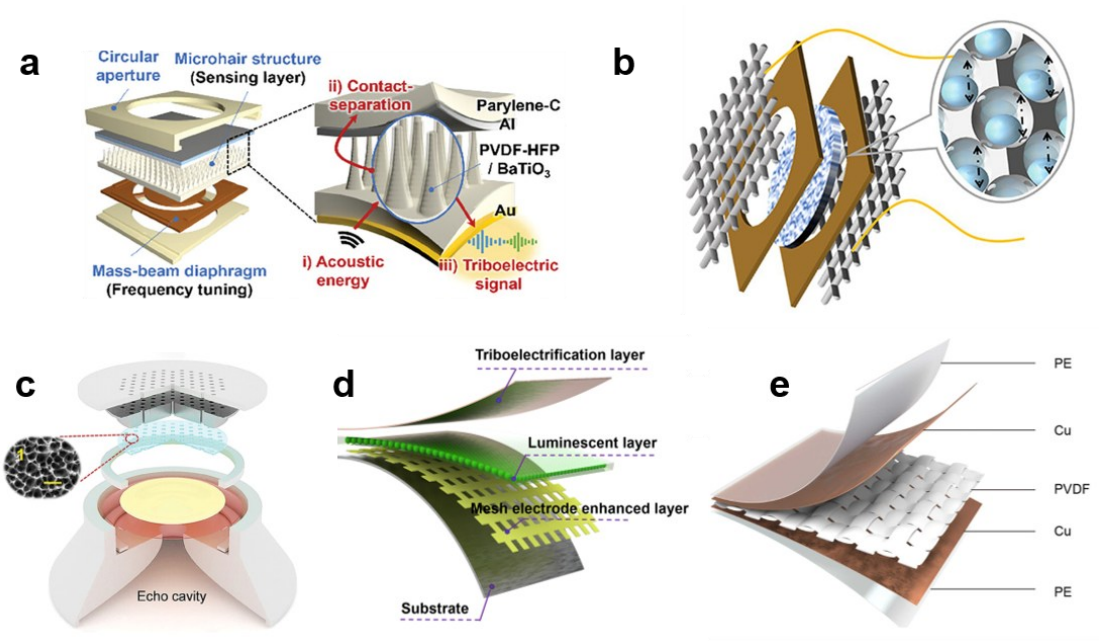

Fig. 2.2 (a) Schematic of a frequency-tuning wearable acoustic device with surface morphological engineering. (b) an acoustic core-shell resonance harvester from nanoscale material optimization. (c) Diagram of a triboelectric stethoscope for cardiac sound sensing. (d) Dual-sensing mode acoustic transducer via electrospun. (e) Triboelectric-based acoustic fabrics with woven structure.

Piezoelectric effect

The piezoelectric effect was first proposed by the Curie brothers in 1880. It includes two phenomena: the direct piezoelectric effect and the reverse piezoelectric effect. As shown in **Fig. 2.3**, the direct piezoelectric effect refers to the phenomenon where induced electrical charges appear on the surface of a piezoelectric crystal when it is deformed under an external force in a specific direction[64-66]. This deformation causes the centers of positive and negative charges to no longer overlap, creating dipole moments. The accumulated charges are linearly proportional to the external force.

When the deformed crystal is connected to an external load, free electrons are driven to flow through the external circuit to achieve dynamic equilibrium[67, 68]. The converse piezoelectric effect, on the other hand, occurs when an external electric field is applied to a piezoelectric crystal. This causes piezoelectric stress within the crystal, leading to piezoelectric deformation[69, 70]. This deformation is macroscopically evident as mechanical deformation and is linearly proportional to the strength of the applied electric field.

Piezoelectric effect have been extensively utilized in acoustic and vibration sensing owing to their self-powered operation, fast response time, and reliable electromechanical coupling.[71-74] Their working principle is based on the bidirectional conversion between mechanical and electrical energy, governed by the constitutive piezoelectric equations[75]:

$$S = s^E T + dE \tag{4}$$

$$D = dT + \epsilon^T E \tag{5}$$

where T and E denote the stress tensor and electric field vector, respectively, and S and D represent the strain and electric displacement of the material. The coefficients s^E, d and ϵ^T correspond to the elastic compliance (at constant electric field), the piezoelectric coupling coefficient (pC/N or pm/V), and the permittivity (at constant stress). As indicated, the piezoelectric constant (*d)* is a critical parameter governing the performance of piezoelectric transducers.

Today, piezoelectric sensor is receiving increasing attention. Compared to capacitive

and piezoresistive devices, piezoelectric effect exhibit higher sensitivity within the audible sound frequency range[76, 77]. By applying the excellent piezoelectric materials with high piezoelectric coefficients and outstanding structure design, multiple resonating vibratory parts can be created in one device. In contrast to triboelectric acoustic sensors, the sensitivity of piezoelectric sensor does not diminish under the influence of temperature and humidity environments, due to the inherent stability of piezoelectric materials[78]. Additionally, they can operate without external power supply, significantly contributing to energy conservation.

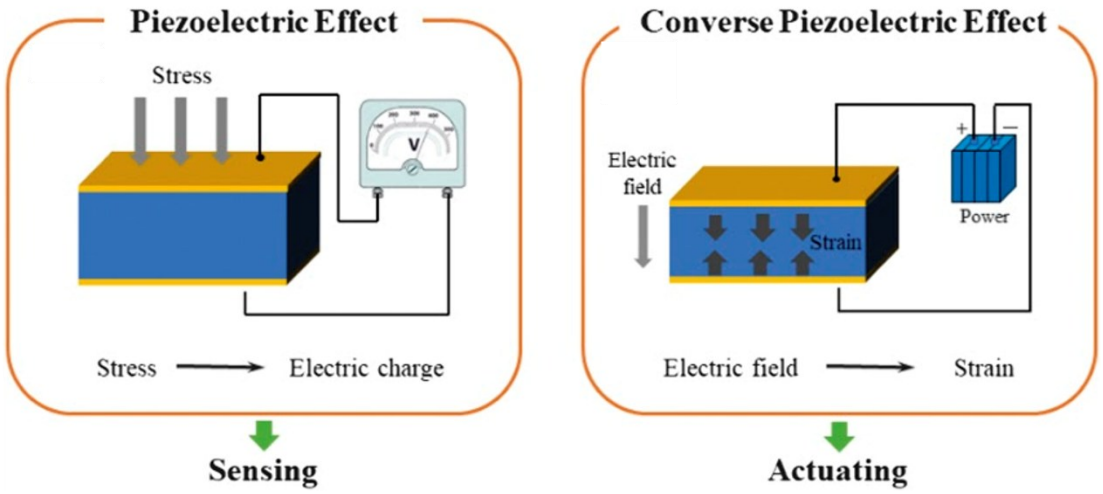

Fig. 2.3 Schematic diagram of the direct piezoelectric effect, the converse piezoelectric effect[79].

Table 2.1 Comparison of acoustic sensing mechanisms.

Factor	Capacitive effect	Piezoresistive effect	Triboelectric effect	Piezoelectric effect
Primary output	Capacitance	Resistance	Charge/voltage	Direct charge/voltage

Factor	Capacitive effect	Piezoresistive effect	Triboelectric effect	Piezoelectric effect
Self-powered sensing	No	No	Yes	Yes
Sensitivity	High	Medium-high	Medium	High
Bandwidth	Wide	Moderate	Low-Moderate	Wide
Noise characteristics	Very low	Thermal drift is significant	Irregular	Low intrinsic
Environmental stability	Sensitive to humidity/contamination	Temperature/humidity drift	Humidity sensitive	High
Flexibility & conformability	Limited	High (polymer composites)	High (soft polymers/textiles)	High (soft polymers/fiber)
Wearability	Good	Good	Moderate	Excellent

2.2 Novel piezoelectric acoustic sensors (PAS)

2.2.1 Working mode of PAS

Generally, d_{31} and d_{33} coefficients are two key parameters for piezoelectric materials that describe the electro-mechanical conversion efficiency in different directions. For d_{33} mode (longitudinal mode), the d_{33} coefficient indicates the electric field generated in the same direction as the main axis (usually the thickness direction) when the material is compressed or stretched. This is known as the longitudinal piezoelectric effect. As shown in **Fig. 2.4a**, if force is applied to the top and bottom of a piezoelectric material, and the voltage generated between the top and bottom is measured, the piezoelectric response in this case is described by the d_{33} coefficient. Piezoelectric material generates charge along the thickness direction and the charge distribution is along the thickness of the material in this mode. Therefore, inspired by human outer ear hair cells, the architectures of PAS in d_{33} working mode are usually fabricated in micro-

cone or pyramid pattern to increase the contact areas with sound waves to enhance the absorption of sound energy which further enhancing output performance and sensitivity of PAS[80]. This makes them particularly suitable for applications requiring high-precision acoustic measurements, such as biomedical monitoring, speech recognition (**Fig. 2.4c**).

For d_{31} mode (transverse mode), the d_{31} coefficient represents the electric potential generated in a plane perpendicular to the direction of applied force (such as the length direction). If force is applied on one side of the piezoelectric material (along its length or width) and the voltage is measured on the sides perpendicular to the direction of force, the piezoelectric response in this situation is described by the d_{31} coefficient. **Fig. 2.4b** demonstrates the working mechanism of d_{31} mode, piezoelectric material generates charge along the length direction of the material (parallel to the electrode plane) and the charge distribution is along the length of the material[80]. Thus, the PAS in d_{31} working mode are typical metal–insulator–metal (MIM) sandwich structure whose electrodes are on the top and bottom of piezoelectric layers. This makes such PAS more suitable for the flexible acoustic device (**Fig. 2.4d**).

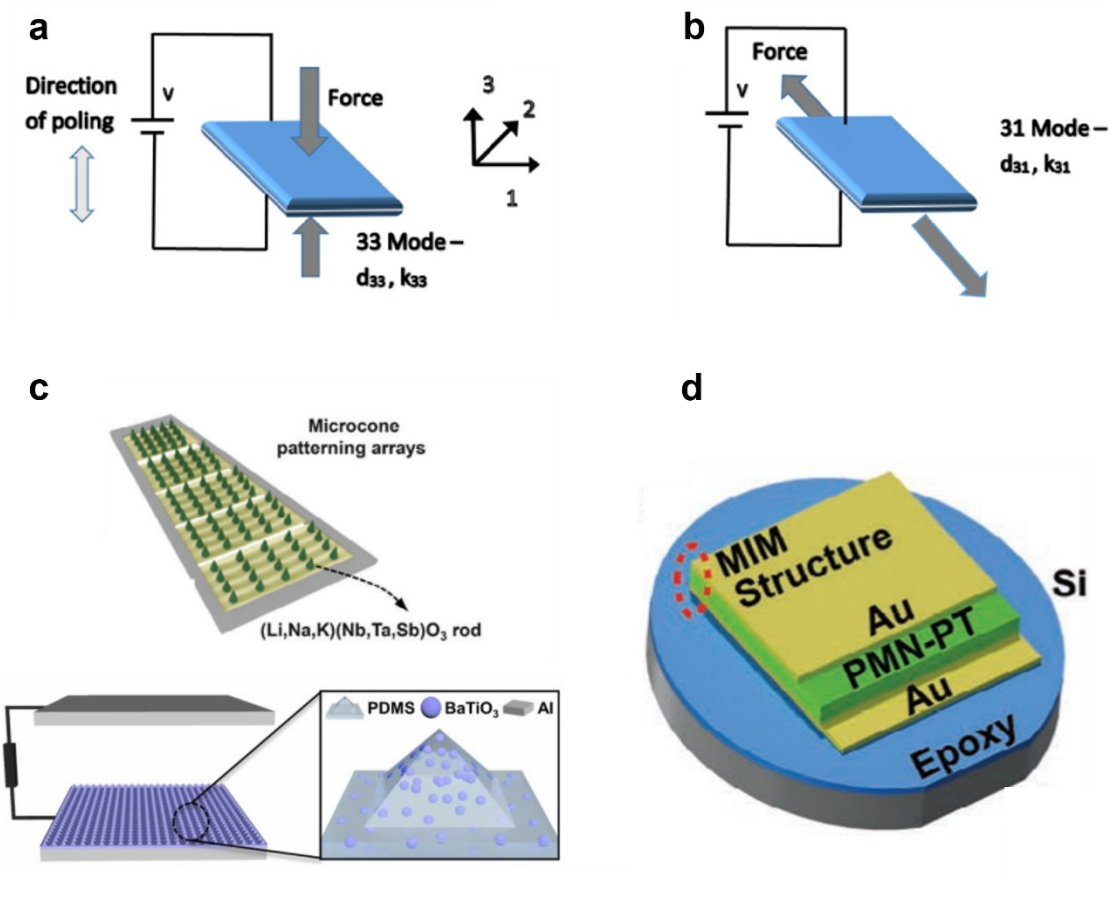

Fig. 2.4 The working modes of PAS and corresponding architectures. (a) d_{33} mode, (b) d_{31} mode.[73, 80] (c) The micro-cone (upper) and pyramid patterns(lower) utilized in d_{33} mode. (d) The MIM sandwich structure utilized in d_{31} mode[81].

2.2.2 Piezoelectric materials

Piezoelectric materials, which exhibit the piezoelectric effect, are categorized into organic and inorganic types. Each type has its unique characteristics and applications. The domain of piezoelectric materials has progressed substantially, transitioning from natural ceramics to engineered composites with a clear trajectory toward enhanced mechanical compliance, functional stability, and energy conversion efficiency.[82-84] Traditional piezoelectric materials such as single crystals (e.g., PMN-PT) and ceramics

(e.g., PZT) have been extensively commercialized for acoustic sensing applications.[85, 86] However, their intrinsic brittleness and rigidity severely constrain their integration into emerging flexible and wearable technology platforms. To overcome these structural limitations, synthetic polymer-based piezoelectrics, most notably polyvinylidene fluoride (PVDF) and its copolymer PVDF-TrFE, have emerged as leading candidates for wearable acoustic sensors, owing to their inherent flexibility, low mass density, facile processability, and favorable biocompatibility.[76, 87-89] Nonetheless, these polymers typically exhibit lower electromechanical coupling coefficients than ceramic counterparts, which compromises energy transduction efficiency.[89] Moreover, their relatively poor thermal stability and mechanical robustness can result in performance degradation under prolonged operation or dynamic loading.[90] Current research has shifted toward developing hybrid composites to reconcile the trade-offs between flexibility and functional performance, wherein piezoelectric ceramics (e.g., $BaTiO_3$) or functional nanofillers (e.g., rGO) are incorporated into polymer matrices.[91-93] This materials engineering strategy seeks to synergistically combine the mechanical adaptability of polymers with the superior piezoelectric characteristics of ceramics, while concurrently enhancing thermal and structural stability. In addition to the above composites, piezoelectrets, an emerging class of porous materials exhibiting piezoelectric-like behavior through quasi-permanent internal charge polarization, have garnered increasing interest for acoustic sensing applications. Characterized by their ultralight weight, mechanical flexibility and high piezoelectric coefficient, piezoelectrets also represent a promising alternative

for future acoustic sensors.[94, 95]

Piezoelectric ceramics

As the most common form of inorganic piezoelectric materials, represented by ferroelectric ceramics like Lead Zirconate Titanate (PZT)[96-98], Barium Titanate ($BaTiO_3$)[99, 100], piezoelectric ceramics demonstrate excellent piezoelectric properties at certain temperatures and are widely used in sensors[101, 102], transducers[103], and precision positioning devices[104-106]. The advantage of piezoelectric ceramics lies in their high piezoelectric coefficients (d_{33}) and electromechanical coupling coefficients (k_{33}), but they are also quite brittle and sensitive to mechanical stress.

Taking $BaTiO_3$ as an example, it belongs to the perovskite structure of ferroelectric ceramics and is widely used in the piezoelectric field. As shown in **Fig. 2.5**, $BaTiO_3$ can be considered to be constructed from TiO_6 and BaO_{12} frameworks, forming an octahedral structure. In this structure, Ti^{4+} is located at the center of the oxygen octahedron, while Ba^{2+} is situated in the gaps between the oxygen octahedral structures[107, 108]. It exhibits several crystal phases, including hexagonal, cubic, tetragonal, orthorhombic, and trigonal phases. As the temperature changes, $BaTiO_3$ undergoes the following phase transitions: from the cubic paraelectric phase (1460–130 °C) to the tetragonal phase with strong ferroelectricity (130–5 °C), then to the orthorhombic phase under 5°C, and finally to the trigonal phase at approximately –90 °C. At room temperature, $BaTiO_3$ exhibits strong piezoelectric and ferroelectric

properties, characterized by a strong spontaneous polarization along [001] direction. When the temperature exceeds above 120 °C, the $BaTiO_3$ crystal transitions to a cubic crystal system, and its piezoelectric and ferroelectric properties disappear[108, 109].

In summary, $BaTiO_3$ exhibits a large electromechanical coupling coefficient and piezoelectric constant, moderate mechanical quality factor, and relatively low dielectric loss. However, its low Curie temperature (T_c = 120 °C) and phase transitions near the room temperature leads to a narrow operational temperature range[110, 111]. Besides, the brittleness of piezoelectric ceramics makes it challenging to combine with flexible substrates to meet wearable characteristics. This combination of properties makes $BaTiO_3$ particularly useful in certain applications but limits its use in others, especially where flexibility and high-temperature stability are required.

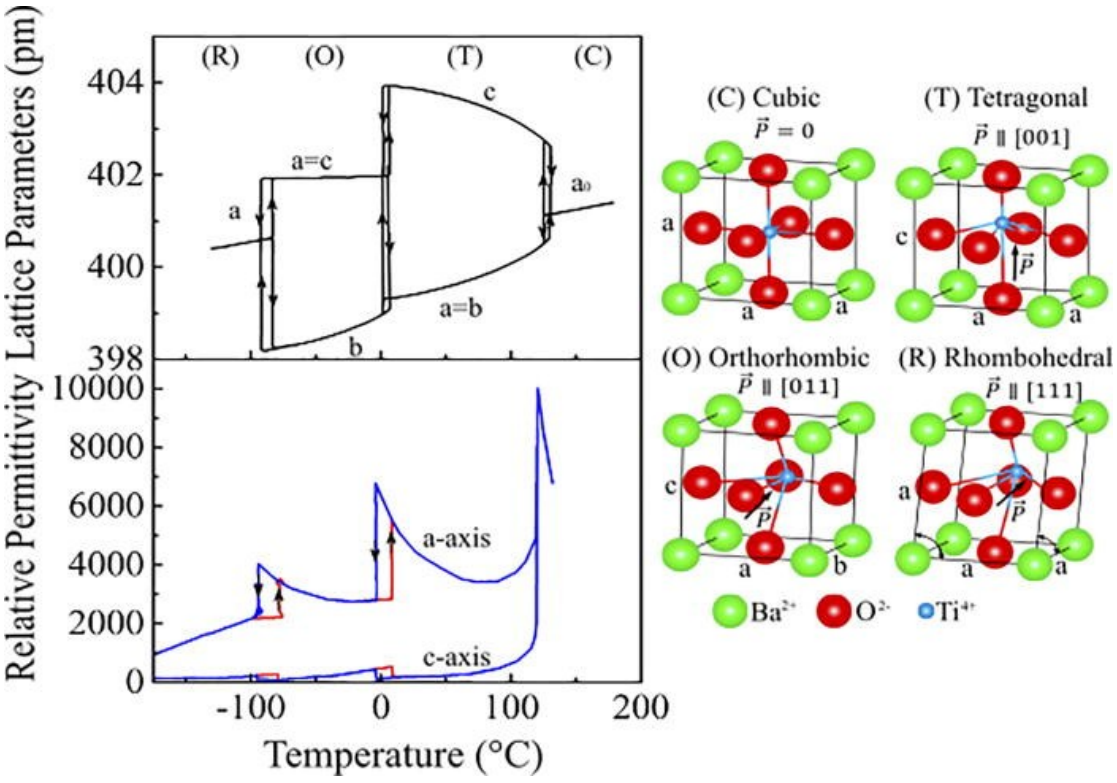

Fig. 2.5 Changes in primite-cell lattice parameters and anomalies in relative permittivity during the sequence of phase transitions in $BaTiO_3$ along with the temperature changes. The right side of the figure illustrates the crystal structure of the cubic prototype phase and the unit cell distortions in each of the ferroelectric phases of $BaTiO_3$[109].

Piezoelectric polymers

Poly(vinylidene fluoride) (PVDF), is a polymorphic polymer whose piezoelectric and ferroelectric properties were discovered around 1970[112, 113]. It mainly characterized by four crystal structures: α, β, γ, δ phases and three different types of polymer chain conformations: TTTT, TG^+TG^-, and $T_3G^+T_3G^-$[114, 115]. **Fig. 2.6a and b** represent the most typical PVDF crystal structures, respectively. The α phase belongs to the monoclinic crystal system, where the molecular chains are in a TGTG' twisted configuration. In this phase, the dipole moments of two molecular chains in each unit cell are arranged antiparallel to the chain axis, leading to the cancellation of these dipole moments. Therefore, the α phase is non-polar and does not exhibit piezoelectric properties. It is also the most stable of all the crystal structures of PVDF[116]. While the β phase is part of the orthorhombic crystal system, with the molecular chains in a TTTT trans configuration (as depicted in **Fig. 2.6b**). In this phase, the dipole moments of the two molecular chains in each unit cell are parallel and oriented in the same direction[115]. This arrangement results in the superposition of the dipole moments' polarity, thereby contributing to the highest piezoelectric properties in β phase. Compared with the piezoelectric ceramics, PVDF has the internal merits of pliability,

low acoustic impedance, and compatibility with soft substrate. However, its low electromechanical coupling factor and piezoelectric coefficient substantially limits its applications.

To improve the piezoelectric performance, various PVDF-co polymers have been development as shown in the **Fig. 2.6c**. Poly(vinylidene fluoride co-trifluoroethylene (P(VDF-TrFE)) is widely utilized in the piezoelectric device as the inducing of large size TrFE unit can strict the transformation from β phase to α phase and contribute to a higher crystallinity in polymers[117, 118]. While the relatively low electromechanical performance still impedes such polymers to be commercialized. Recently, Poly(vinylidene fluorideco-trifluoroethylene-co-chlorotrifluoroethylene) (P(VDF-TrFE-CFE)) springs with high dielectric constant which belongs to a family of novel ferroelectric polymer materials [106]. For this ternary polymer composite, the existence of TrFE and CFE can increase the interchain distance and weaken the intermolecular interaction of PVDF. Thus, the large ferroelectric domains were split into nano-sized domains bringing relaxor ferroelectric behavior (RFE) with high dielectric constant and resulting in high piezoelectric coefficients which are the key parameters to the high sensitivity of final acoustic sensors [89, 119].

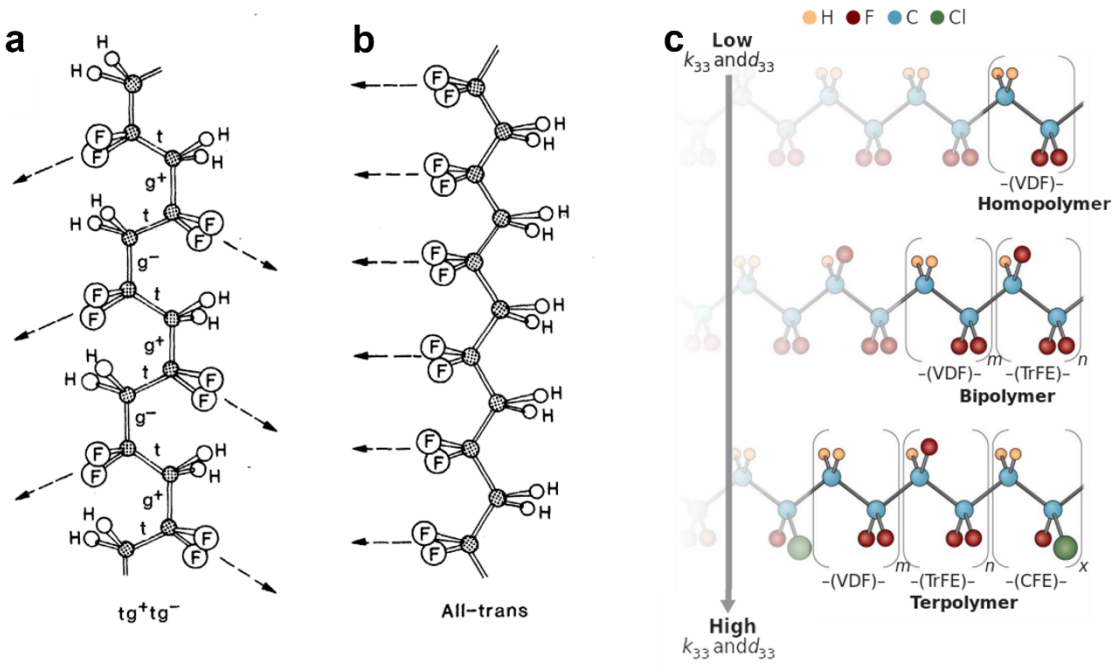

Fig. 2.6 The crystal structures of PVDF with α phase (a) and β phase (b)[115]. (c) The development of PVDF-co polymers with the increasing k_{33} and d_{33}[120].

Piezoelectric composites

Table 2.2 summarized the key parameters of k_{33} and d_{33} of the PVDF based copolymers and make a comparison with typical piezoelectric ceramics. As shown in the table, the piezoelectric constant of PVDF-TrFE-CFE is comparative with the $BaTiO_3$ while it is still lower than PZT. Some researchers have addressed this constraint by combining the advantages of piezoelectric ceramics and piezoelectric polymers, producing composite piezoelectric materials that are not only flexible but also exhibit a high piezoelectric coefficient. For example, Yan et al. [4] used PVDF-TrFE/$BaTiO_3$ to create a fibrous, flexible piezoelectric transducer through thermal drawing, inspired by the tympanic membrane in human auditory system. This innovation resulted in a highly sensitive

acoustic fabric which can detect tenuous 10^{-7}-atmosphere pressure waves at audible frequencies. Deng et.al utilized the inorganic perovskite $CsPbBr_3$ (CPB) incorporated with PVDF via electrospinning to prepare CPB/PVDF composites.[121] Both the CPB and PVDF are poled during the electrospinning process and the output performance of these composites is 8.4 times higher than the pure PVDF web. These successful cases indicate that the development of piezoelectric composites is the trend for future wearable piezoelectric devices.

Table 2.2 The comparison of electromechanical coupling factor (k_{33}) and piezoelectric coefficient (d_{33}) between different piezoelectric materials.

Materials	PVDF [122]	PVDF-TrFE [123]	PVDF-TrFE-CFE [124]	$BaTiO_3$ [125]	PZT [97]
k_{33}	23%	27%	55%	50%	80%
d_{33} (pm/V)	–35	–63.5	–400	193	800

2.2.3 Flexible piezoelectric acoustic sensor (FPAS)

The rapid electromechanical response of piezoelectric materials makes them highly suitable for acoustic sensing. Structural design plays a vital role in enhancing the performance of flexible piezoelectric acoustic sensors (FPAS). Early designs often employed MEMS-based structures such as cantilevers and diaphragms in a conventional sandwich configuration with top and bottom electrodes. With the development of Internet of Things (IoT) and flexible electronic technologies, there is a

continuous evolution towards miniaturization, flexibility, high sensitivity, and multifunctional integration. Nowadays, various structural strategies have been employed to amplify mechanical deformation and thus enhance signal output (**Fig. 2.7**).

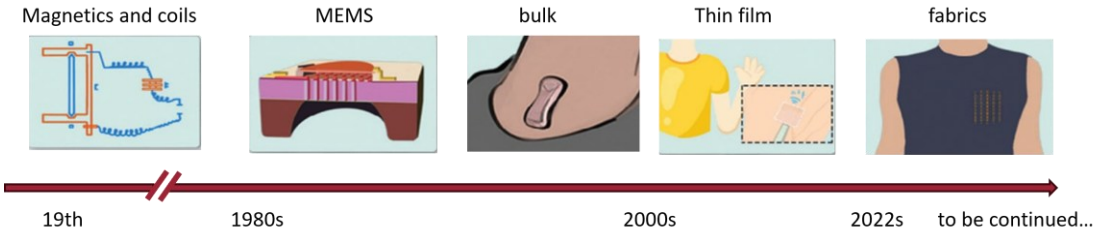

Fig. 2.7 The development and future trends of acoustic sensors.

Structure design

More recently, advances in bioinspired design have led to new developments of FPAS. For example, inspired by the cochlear amplifier function of outer hair cells in the human ear, a flexible piezoelectric sensor was developed using a printed micro-cone array based on a lead-free multicomponent perovskite material (**Fig. 2.8a**).[73] Through orientation engineering and the formation of quasi-morphotropic phase boundaries between two orthogonal phases, the stress transfer and strain expansion in niobate rods were enhanced, resulting in improved piezoelectric performance. Moreover, the patterned micro-cone geometry increased the contact area with incoming sound waves, thereby amplifying vibration and acoustic absorption. The resulting device demonstrated a high sensitivity of 150.63 mV Pa^{-1} across a frequency range of 100–3000 Hz, along with notable directional responsiveness.

In many cases, the fabrication process can also help tailor flexibility and piezoelectric

properties, particularly the d_{31} coefficient, through mechanical alignment. Inspired by the sound conduction mechanism of the human tympanic membrane, a thermally drawn piezoelectric fiber with a d_{31} coefficient reaching ~46 pC N^{-1} was reported.[4] When integrated onto an anisotropic textile substrate with high Young's modulus, the structure amplified the mechanical vibration (**Fig. 2.8b**). This acoustic fabric demonstrated nanoscale vibration sensitivity, capable of detecting sound pressures as low as 10^{-7} atm, with potential applications in bidirectional audio communication and sound source localization. Beyond thin films, piezoelectric nanofibers, owing to their low acoustic impedance, high surface-to-volume ratio, and porous structure, have also been widely explored in acoustic sensors. One notable example is a bioinspired auditory system that combines piezoelectric nanofiber arrays with machine learning **(Fig. 2.8c**).[88] A spiral trampoline structure composed of radially arranged nanofibers with gradient lengths and orientations was used to encode acoustic information physically. Resonant gradients produced frequency-selective mechanical responses; channel-to-channel differences mimicked time-delay cues, while the asymmetric geometry enabled directional spectral filtering. With the aid of deep learning algorithms, the system achieved full 3D spatial sound localization.

In addition, piezoelectrets-ferroelectric polymers with engineered voids and tunable dipole alignment are gaining attention for their mechanical flexibility and adjustable piezoelectric performance. A recent example is a dual-layer porous piezoelectrets patch with electromagnetic shielding, designed for detecting subtle physiological sounds (**Fig. 2.8d**). The artificial pores enhanced dipole density, yielding a high dynamic sensitivity

of 591 pC kPa^{-1} in the 0–8 kPa range. Meanwhile, the shielding layer reduced harmonic interference by over 20 dB.[94] This device demonstrated accurate detection of heart sounds, respiratory signals, speech, coughing, and swallowing, indicating its potential for digital stethoscope applications.

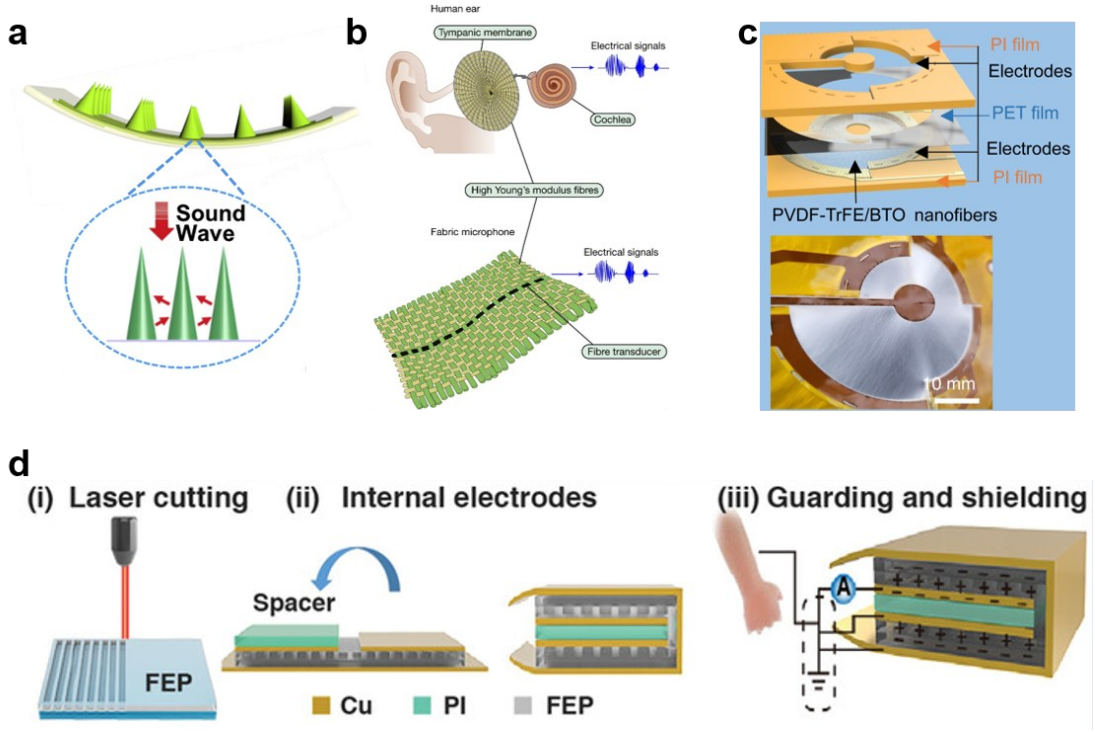

Fig. 2.8 Representative works on PAS with various designs and fabrication techniques. (a) Schematic illustrations of flexible piezoelectric sensor with micro-cone array. The inset is the reflection of incident sound waves among microcones. (b) Eardrum-inspired acoustic fabric with single piezoelectric fiber via hot stretching. (c) Piezoelectric nanofiber-based intelligent hearing system with spiral trampoline-like structure. (d) Diagram of wearable piezoelectric electret patches used for health monitoring.

Wearable technology and bioacoustics applications

As wearable technology continues to advance, the integration of flexible electronics

with piezoelectric materials has gradually led to the development of FPAS. These can be widely applied in small electronic devices and advanced personal health monitoring fields. FPAS mainly consisted of organic piezoelectric polymers and inorganic ceramics. Shintaku et al. [126] designed a multichannel acoustic sensor based on flexible PVDF film, which exhibited frequency-selective response characteristics. As illustrated in **Fig. 2.9a**, a PVDF layer with deposited electrodes was mounted on a substrate featuring trapezoidal apertures, emulating the behavior of a passive basilar membrane. The film width was gradually tapered along its length, resulting in position-dependent resonant frequencies. Electrodes were labeled sequentially from Ch. 1 to Ch. 24 corresponding to increasing film widths. The self-powered piezoelectric device was attached to a stainless-steel substrate filled with silicone oil to simulate an in vivo environment. **Fig. 2.9b** compares the vibrational motion (solid line) and output voltage (dashed line), showing aligned amplitude peaks and consistent frequency dependence. Measured resonant frequencies reached 3.64 kHz, 2.32 kHz, and 1.88 kHz at Ch. 6, Ch. 12, and Ch. 18, respectively. Despite its frequency selectivity, the sensor showed limited sensitivity to faint acoustic signals below 60 dB.

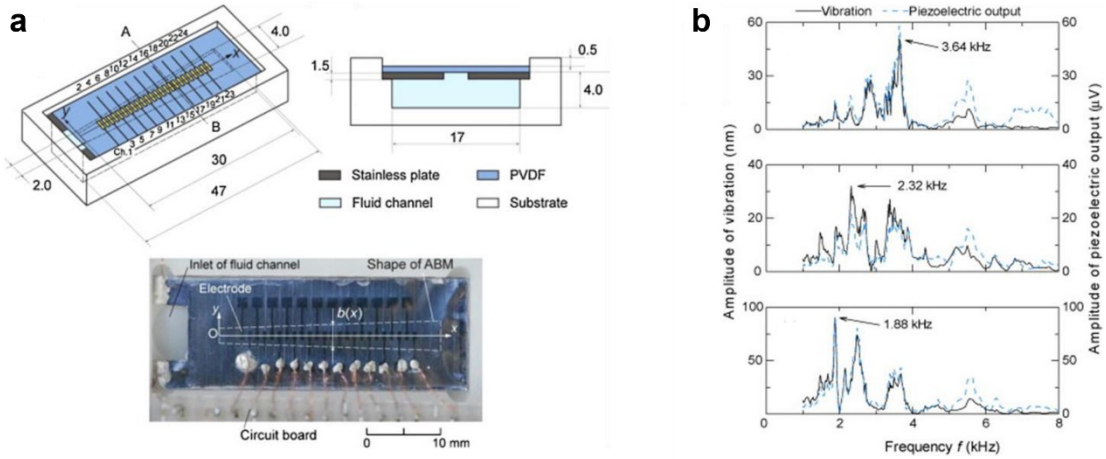

Fig. 2.9 (a) The structure of PVDF based PAS. (b) Resultant vibration amplitude and output voltage from Ch. 6, Ch. 12, and Ch. 18[126].

In 2018, Park et.al[127] fabricated a flexible, self-powered sandwich-structured PVDF based PAS with MIM structure and encapsulated it in PDMS cylinder via injection molding. **Fig. 2.10a** shows a schematic of the structure. To increase output voltage of device, an amplifier with a 1000-fold amplification factor was connected to the device to explored its performance in both air and liquid. **Fig. 2.10c** shows the sensitivity response in different sound pressure levels (SPL) when the device was placed in a sound pressure chamber. When the device was subjected to sound signals with frequencies of 1–60 kHz and SPL of 80 and 100 dB, the response spectrum displayed multiple peaks and valleys. This is because the PDMS tube itself resonates to varying degrees, influencing the output of the device.

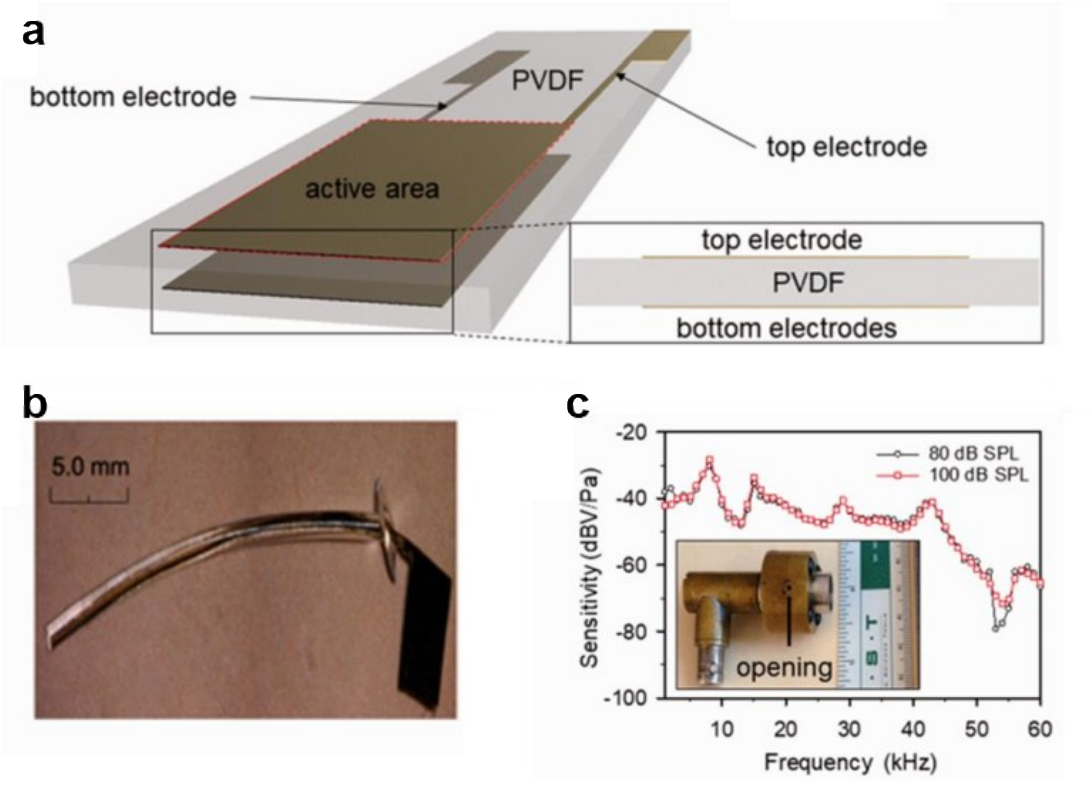

Fig. 2.10 (a) Schematic of acoustic device with electrodes patterned on top and bottom surface of PVDF film. (b) Photograph of the PVDF sensor encapsulated in PDMS cylinder. (c) The sensitivity of PVDF acoustic device inside an air pressure chamber. Sound pressure was delivered at two levels (80 and 100 dB). Inset shows air pressure chamber[127].

Lee et al.[128] developed an inorganic piezoelectric acoustic sensor (PAS) by transferring a PZT thin film onto a trapezoidal silicone membrane, which functioned as a frequency-separating structure mimicking the basilar membrane. As depicted in **Fig. 2.11a**, the sensor emulates the organ of Corti, with the PAS acting as an artificial hair cell capable of generating piezoelectric potential in response to subtle sound vibrations. Three sensor units were positioned at different locations on the synthetic trapezoidal membrane to replicate the spatial frequency-sensing behavior of biological hair cells. **Fig. 2.11b** shows an optical image of the PAS array mounted at the apex, middle, and base regions of the silicone substrate. Vibration responses were frequency-dependent: low-frequency sounds primarily excited the apex, while high-frequency stimuli induced vibrations at the base. As shown in **Fig. 2.11c**, the device achieved a conversion of 7.6 nm vibrational displacement into 59.7 μV output at the resonance frequency of 1000 Hz. Additionally, PAS units located at the apex and middle regions successfully identified low and mid-frequency signals at 500 Hz and 600 Hz, respectively, within the target vocal frequency spectrum.

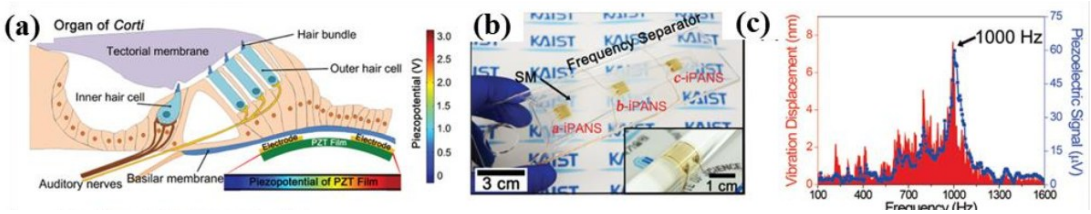

Fig. 2.11 (a) Conceptual illustration of organ of Corti in mammalian cochlea. (b) Optical image of the frequency separator with PAS. (c) Vibration displacement and piezoelectric signal [128].

The application of acoustic sensors in the field of biomedicine is also rapidly expanding. These sensors are used for detecting and diagnosing various physiological conditions of the body, enabling real-time monitoring and providing instant data to healthcare providers[129, 130]. Electronic stethoscopes are progressively replacing traditional auscultation methods, offering real-time and accurate detection of sounds from the heart, lungs, and bowel movements. For instance, by analyzing the intensity, frequency, and pathological murmurs of heart sounds, these sensors can aid in diagnosing cardiovascular diseases; they can also identify conditions such as asthma, Chronic Obstructive Pulmonary Disease (COPD), or sleep apnea by monitoring breathing patterns[131, 132]. Furthermore, for patients with hearing impairments, acoustic sensors are an integral part of cochlear implant systems, converting sound waves into electrical signals to directly stimulate the auditory nerve. These advanced applications demonstrate the significant potential and value of acoustic sensors in the realm of modern medical and health care.

Table 2.3 summarized the relevant applications in biomedical field and the required

parameters of flexible acoustic sensors. As we can see, in the realm of biomedical applications, the evolving demands on acoustic sensors have become significantly more rigorous, particularly concerning their sensitivity, response range, and durability. Enhanced sensitivity is crucial for accurately detecting subtle and low-amplitude sounds like faint heart murmurs or variations in breathing, vital for precise medical diagnoses. A broad response range is essential due to the diverse range of frequencies and intensities of sounds encountered in medical settings, from low-frequency heart sounds to higher-frequency gastrointestinal or respiratory noises. The trend towards wearable healthcare devices and implantables necessitates not only the miniaturization but also the durability, as they must withstand regular sterilization processes and provide reliable, long-term performance, especially in continuous monitoring devices. Additionally, advanced noise reduction techniques and signal processing algorithms are required to ensure the data's accuracy and reliability with high SNR. Besides, temperature and humidity can affect the operational stability and measurement accuracy of sound sensors. Collectively, these factors are pushing the boundaries of acoustic sensor technology, driving innovation in fabrication, miniaturization, and advanced signal processing to meet these heightened requirements in biomedical applications.

Table 2.3 The required parameters of FPAS for bioacoustics applications.

Frequency range	S1 (40–60 Hz) S2 (60–100Hz)	40–300 Hz	150–500 Hz	100–4000 Hz
Dynamic range in various applications	/	>45–40 dB	>34–40 dB	40–60 dB

	Heart sounds[133]	Breath sounds[134]	Bowel sounds[12]	Speech sounds[135]

Note: S1 is the heart sound signal formed by ventricular contraction, which makes the ventricular pressure exceed the atrial pressure, and the blood forces the atrioventricular valve to vibrate. S2 marks the beginning of the ventricular diastole. This is the vibration caused by the outflow of blood from the ventricular, causing closure of the aortic and pulmonary valves.

2.3 Fabrication via electrospinning techniques

Fabrication technology can impact various characteristics, such as sensing performance, cost, efficiency, and industrialization potential of the PAS. The typical fabrication methods include MEMS, coating, transfer printing, thermal drawing and electrospinning. Among these, electrospinning is not only a scalable method for fibrous membrane acoustic sensors but also an effective strategy to promote the β phase in PVDF-family piezoelectric polymers: the combination of a strong electric field and intense extensional flow aligns chains into the all-trans conformation and partially poles dipoles in situ. Compared with β-phase induction by filler doping, electrospinning avoids foreign nucleating agents that can increase dielectric loss or stiffen the film; relative to mechanical stretching, it achieves chain alignment at (near) room temperature without large draw ratios or added thermal steps; and versus post electrical poling, it reduces processing steps, energy input, and dielectric-breakdown risk because dipole orientation is established during deposition. In practice, electrospinning enables single-step fabrication without extra poling, is readily combined with coating or transfer

printing, and yields lightweight, porous, conformal membranes that are advantageous for acoustic impedance matching. Herein, we will make a detailed introduction of the principle and key factors for the processing of electrospinning for PAS.

2.3.1 Fundamentals of electrospinning

Electrospinning is a fiber production technique that uses electric force to draw charged threads from polymer solutions or melts, resulting in fibers with diameters ranging from micro to nanoscale.[136, 137] The process initiates when a high voltage is applied to a polymer solution, forming a Taylor cone at the nozzle tip. A jet is subsequently ejected and undergoes stretching and whipping instabilities, leading to extreme thinning and solvent evaporation, which solidifies the fiber. By adjusting parameters such as solution concentration, applied voltage, flow rate, and environmental conditions, fibers with controlled morphology, porosity, and alignment can be achieved.[138, 139] The basic configuration of a typical electrospinning setup is illustrated in **Fig. 2.12a**. Under appropriate viscosity and ambient conditions, a stable and continuous process can be maintained, as shown in **Fig. 2.12b**. This versatile method is widely used to fabricate functional materials for applications in tissue engineering, sensors, energy devices, and filtration membranes.

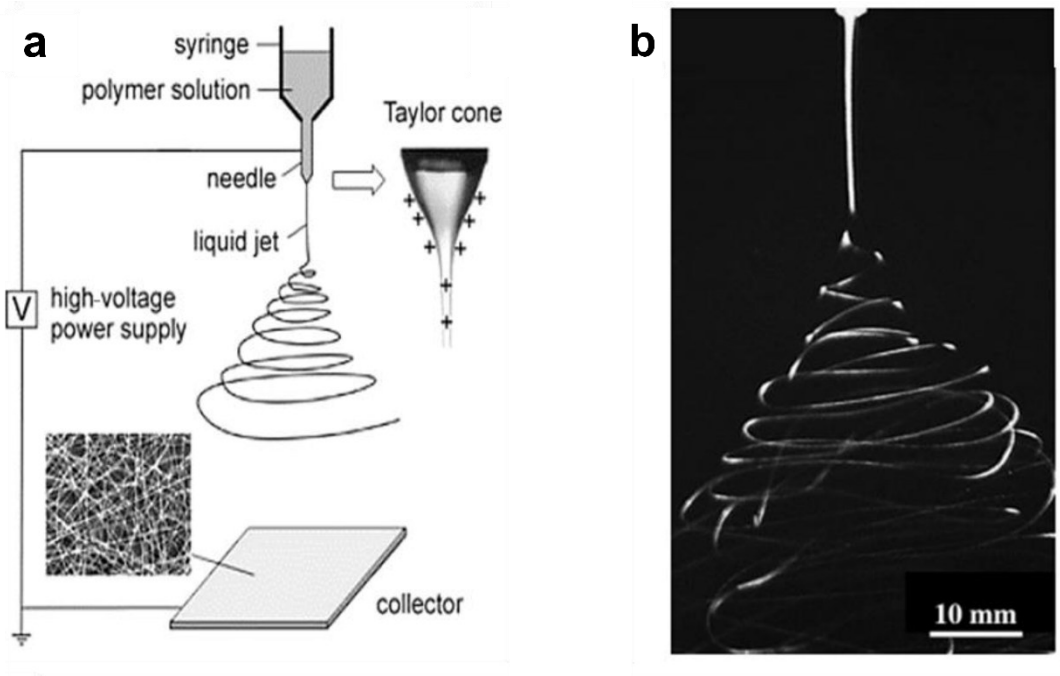

Fig. 2.12 The principle of electrospinning. (a) Basic setup of electrospinning. (b) A snapshot of an electrospinning jet with well-developed loops from the nozzle[140].

2.3.2 Current status of electrospinning for PAS

Electrospun nanofibers exhibit a number of advantageous properties, including extreme fineness, high specific surface area, tunable nanostructures, and ease of doping or functional modification. The high tunability of both material properties and electrospinning parameters enables the design of nanofibers with fundamental characteristics ideal for PAS. Due to their solution processability, a wide range of piezoelectric materials, such as PVDF,[141] PVDF/BTO composites,[17] P(VDF-TrFE),[142] polyurethane (PU),[61] PZT,[143] and PAN,[144] can be processed via electrospinning. Consequently, significant research efforts have been directed toward optimizing polymer compositions and nanostructures to further improve sensing

performance.

The random orientation of electrospun nanofibers often influences their mechanical, electrical, and optical properties. Aligning the dipoles within piezoelectric polymer nanofibers significantly enhances piezoelectric output, a process that can be facilitated by mechanical stretching during electrospinning. Consequently, alignment strategies such as near-field electrospinning, high-speed collection, and mechanical stretching have attracted considerable attention for improving device performance. For instance, Huang et al. developed a dynamic near-field electrospinning technique to fabricate aligned nanofiber meshes in situ for broadband, self-powered PAS.[145] These meshes mimic the high-aspect-ratio, ultrathin, and free-standing morphology of biological nonresonant acoustic sensors, yielding high device sensitivity at safe sound pressure levels and superior signal fidelity. Similarly, Wang et al. produced aligned P(VDF-TrFE) fibers using a high-speed rotating drum coupled with a strong electric field, resulting in well-oriented dipoles.[142] The resulting PAS exhibited sensitive responses to dynamic forces (0–25 N) and acoustic stimuli across a wide range (60–110 dB).

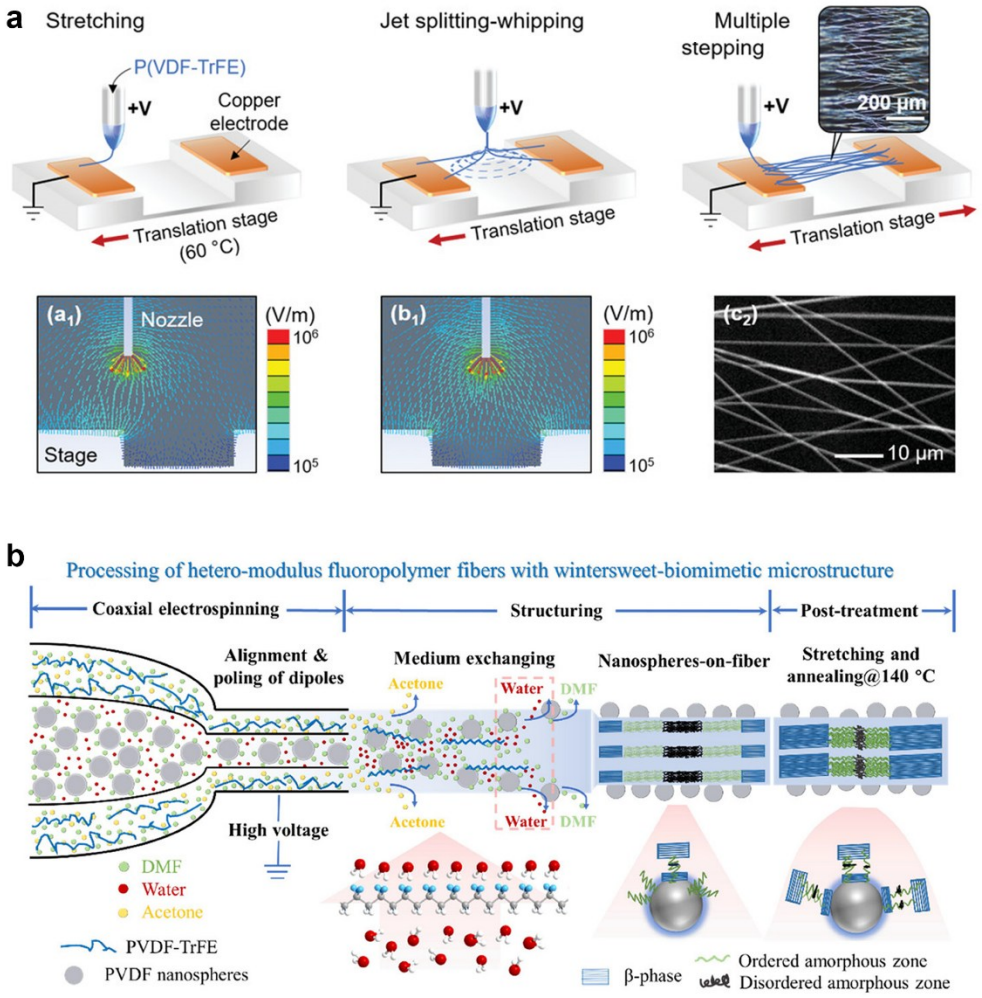

Fig. 2.13 Schematic illustrations of the preparation of aligned electrospun nanofibers (a) dynamic near-field electrospinning technique, (b) high-speed rotating drum.

Moreover, the polar phase content of nanofibers can be optimized by adjusting electrospinning parameters, which fall into three categories: polymer properties (molecular weight and polarity), solution parameters (solvent composition, type, and concentration), and processing conditions (flow rate, needle size, voltage, tip-to-collector distance, spinning time, and collector speed). Molecular weight influences spinnability, fiber morphology, and mechanical properties, while polar groups (e.g., –CF_2, –CN) enhance dielectric behavior through electric-field-induced dipole formation.

Solution concentration and solvent volatility affect fiber uniformity and crystallization. Low concentrations promote bead formation due to inadequate chain entanglement, whereas excessively high viscosity impedes polymer stretching and polarization. An intermediate concentration facilitates stable jet formation and promotes crystalline phase development through reduced evaporation rates. Processing parameters also significantly impact polarization. Flow rate and needle diameter influence shear stress, which enhances molecular alignment within an optimal range. Excessive flow rates or overly small needles can cause flow instability or clogging, reducing crystallinity. Collector speed and mechanical stretching promote fiber alignment and polar phase transformation. Tip-to-collector distance and applied voltage regulate jet stability and stretching force; excessive distance or voltage leads to instability and lower polarization. Although spinning time mainly affects film thickness and resistivity, it also indirectly influences piezoelectric output.

In summary, electrospinning parameters profoundly affect spinnability, dipole alignment, morphology, and performance. Compared to traditional methods, electrospinning offers in situ poling and stretching, produces flexible and breathable films ideal for PAS, and is scalable for industrial production.

2.3.3 Integration of electrodes on electrospun nanofibers

Typical PAS comprise a piezoelectric membranes sandwiched between two electrodes. Electrode design is one of the key factors to improve sensor sensitivity. Metal coating, conductive polymer membranes or flexible elastomers filled with conductive materials,

such as graphene nanoplatelets (GNPs), carbon nanotubes (CNTs), and MXene, are mainly used as electrodes. For example, Lang et al. demonstrated a highly sensitive flexible piezoelectric nanofiber-based acoustic sensor by electrospinning a PVDF solution.[146] In this sensor, the PVDF nanofiber web was sandwiched between two gold-coated PET films where a hole formed to enable nanofibers to efficiently interact with sound waves (**Fig. 2.14a**). The gold-coated surfaces were contacted with the nanofibre layer, and they functioned as electrodes to collect electrical signals. Similarly, Wang et al. used a lamination process to incorporate a copper foil layer on the PET film, which serves as an electrode for signal transduction.[147] The structural design of the PET film and the copper foil emulates ridge and microrib configurations (**Fig. 2.14b**).

Furthermore, integrated electrode design on electrospun nanofibers has been demonstrated as an effective architecture that avoids the use of conductive additives and polymer binders, resulting in more compact and efficient electrode systems. Direct electrode integration not only simplifies the device structure but also enhances interfacial contact and signal transduction. Conductive materials such as AgNWs, graphene, or PEDOT/PSS can be directly deposited onto the nanofiber mesh through magnetron sputtering, printing, or in situ growth, forming continuous and flexible conductive networks. Among these techniques, magnetron sputtering stands out as one of the most widely utilized methods for depositing electrodes onto electrospun nanofibers (**Fig. 2.14c**).[144, 148, 149] The resulting coating exhibits excellent conductivity and stability while preserving the porous microstructure and flexibility of the underlying fibers. However, prolonged exposure to plasma may cause etching or

damage to fine nanofibers. In addition, spray coating presents another effective route for electrode integration (**Fig. 2.14d**).[16, 150-152] This approach typically involves dispersing conductive nanomaterials in a solvent to form an ink, which is then directly applied onto the electrospun nanofiber mesh. Its primary advantage lies in its simplicity, low cost, and scalability. The process can be performed under ambient conditions, making it highly attractive for rapid prototyping and large-scale industrial production. Despite its potential, the solution-based method is limited by non-uniform coverage, solvent-induced damage, thermal degradation during post-treatment, and poor adhesion, limiting its practical application.

In summary, the design of the electrode is paramount to the performance of PAS. It directly dictates key metrics such as sensitivity, signal-to-noise ratio, mechanical flexibility, and long-term stability. An optimal electrode must not only efficiently collect generated charges with minimal loss but also do so without compromising the inherent advantages of the electrospun piezoelectric layer.

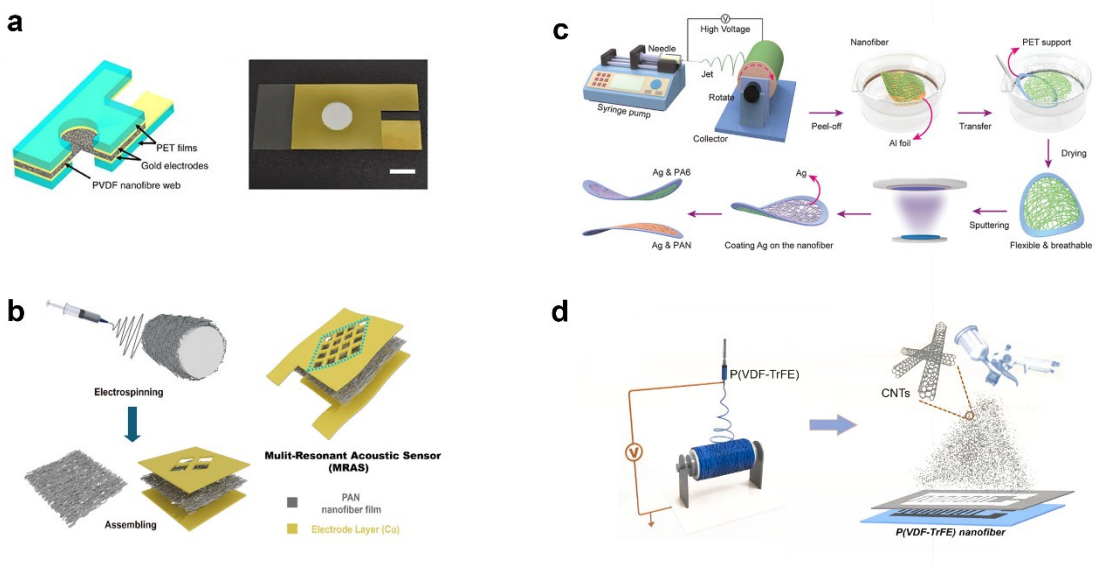

Fig. 2.14 Schematic diagram of electrode integration. (a) metal coating, (b) metal plate, (c) magnetron sputtering, and (d) spray coating.

2.4 Performance requirement and evaluation for acoustic sensors

2.4.1 Core metrics

Over the past few decades, the development of bioacoustics sensors has been predominantly driven by efforts to improve their comprehensive performance across a broad set of parameters. However, from an application-oriented standpoint, it is neither necessary nor practical for a sensor to exhibit optimal performance in all domains. Instead, tailoring the sensor's capabilities to meet the demands of specific application scenarios is more meaningful. For instance, cardiovascular monitoring necessitates high sensitivity and a high SNR within the 20–600 Hz range to capture faint heart sounds[60, 94]. In contrast, ecological studies of bat echolocation prioritize ultrawideband frequency response (80–120 kHz) and ultrafast transient response (<0.1 ms) over ultrahigh sensitivity.[153, 154] These diverse requirements in bioacoustics applications dictate which performance parameters should be prioritized during sensor design and fabrication. This section provides a concise overview of the core selection criteria in some specific application scenarios (healthcare, agriculture, HMI and sports), including benchmarks like sensitivity, response and recovery times, operational frequency range, SNR, dynamic range and resolution. In parallel, system-level metrics such as environmental robustness, directionality, acoustic impedance matching, signal processing integration, biocompatibility, and long-term stability are considered in

diverse deployment environments like healthcare, sports, human–machine interfaces (HMI), and agriculture (**Fig. 2.15**). Establishing these evaluation criteria facilitates more rational selection of sensor mechanisms, materials, and structural designs, thereby promoting systematic and application-specific development of future bioacoustics sensors.

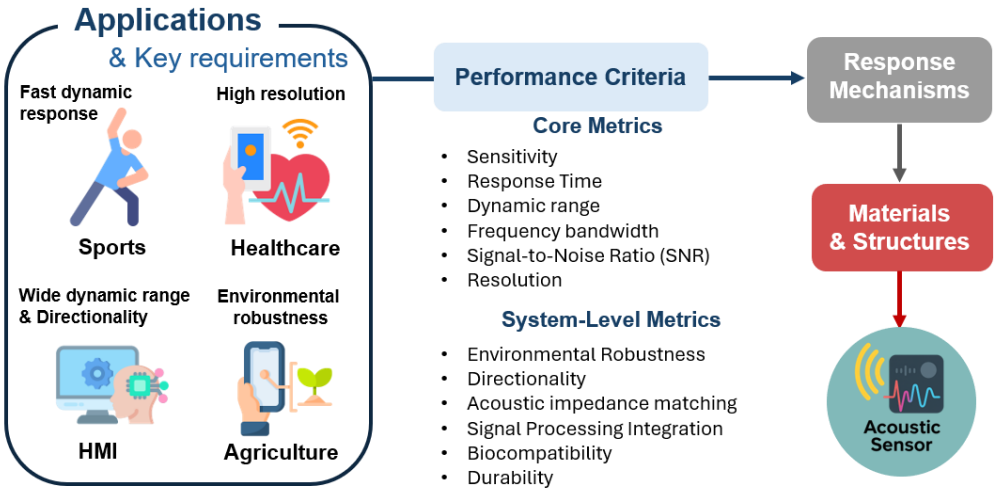

Fig. 2.15 Performance requirements and selection criteria for various bioacoustics sensors.

Sensitivity, typically expressed in mV Pa^{-1} or dBV Pa^{-1}, is a key performance metric for various acoustic sensors, reflecting the electrical output generated per unit of sound pressure. High sensitivity is essential for detecting weak acoustic signals, which is particularly important in bioacoustics applications such as monitoring insect vocalizations,[155] gastrointestinal sounds,[156] and voice recognition[87] in which signal amplitudes are often extremely low. Accordingly, enhancing sensitivity remains a central objective in developing bioacoustics sensing systems to enable the reliable

acquisition of biologically relevant acoustic information. Despite high sensitivity, the dynamic range and frequency bandwidth also play a critical role and must be tailored to the specific acoustic characteristics of each application. For instance, in physiological monitoring, cardiac sounds are predominantly confined to frequencies below 500 Hz at subtle acoustic signal (around 30–50 dB), whereas pulmonary signals may span a broader range from 100 Hz to over 3,000 Hz.[157] These varying frequency requirements necessitate sensor designs that not only maximize sensitivity but also ensure spectral alignment with the target signals. As such, achieving both high sensitivity and appropriate frequency response constitutes a dual design imperative in the development of acoustic sensors for complex bioacoustics environments. Notably, to achieve a flat frequency response, the resonance frequency of the designed acoustic sensor should be positioned outside the target frequency range. Nevertheless, in specific applications involving a narrowband signal, a tailored resonance band may be introduced to detect weak acoustic signals.[158]

Response times, defined as the durations required for a sensor to reach its peak output following a stimulus and to subsequently return to baseline, are critical parameters in the performance evaluation of acoustic sensors. These temporal metrics are particularly important in applications involving rapidly changing acoustic signals or high-frequency sound, where inadequate temporal resolution can lead to significant signal distortion or loss of fidelity. In bioacoustics sensing, many physiological sound sources exhibit inherently transient characteristics, posing challenges to accurate signal capture. Owing to the inherent electromechanical transduction mechanisms, piezoelectric and

triboelectric materials offer rapid dynamic response capabilities, making them promising candidates for bioacoustics sensors capable of capturing high-frequency and short-duration biological sound events with high fidelity. Notably, recent studies have demonstrated triboelectric thin-film acoustic sensors capable of achieving ultrafast response times of approximately 0.8 ms under 80 Hz acoustic excitation, highlighting their potential for capturing transient bioacoustics signals with high temporal precision.[159]

Resolution refers to the smallest detectable variation in an external acoustic stimulus, representing the sensor's capacity to discriminate subtle differences in waveform or frequency. In bioacoustics sensing, particularly in physiological monitoring, high resolution is critical for identifying minute signal fluctuations that may indicate underlying biological activity. For instance, minor variations detected by ultrasonic transducers can serve as early indicators of pathological changes in organ tissues.[160] In clinical contexts, high-resolution acoustic sensors are often employed to extract diagnostically relevant features from complex biosignals. However, enhanced resolution also increases the sensor's susceptibility to ambient noise, necessitating the incorporation of advanced signal processing techniques to ensure signal fidelity.

Building on this, another critical performance metric for evaluating acoustic sensors is the **signal-to-noise ratio (SNR)**, which quantifies the proportion of useful signal relative to background noise and indicates signal fidelity. High SNR is crucial for detecting low-amplitude acoustic signals, as it ensures that the output remains

distinguishable from noise, thereby preserving signal interpretability and enabling accurate feature extraction. Enhancing SNR can be achieved primarily by amplifying the sensor's response output or reducing noise components. While environmental noise is inherently unavoidable in practical applications, efforts typically focus on minimizing intrinsic circuit noise through structural shielding, circuit-level optimization, and signal modulation techniques to attain superior SNR performance. A common strategy involves selecting amplifiers with appropriate gain to boost weak acoustic signals, along with the integration of notch filters to effectively suppress Power frequency interference.

2.4.2 System level metrics

Beyond the core sensing metrics discussed above, several system-level parameters should be considered. Foremost among these is environmental robustness. Bioacoustics sensors are frequently deployed in diverse scenarios, each with distinct environmental challenges. For instance, acoustic sensors intended for wild animal detection or migratory bird tracking require effective protection against dust ingress and wind-induced acoustic interference. Acoustic sensors deployed underwater demonstrate strong resistance to water, corrosion and thermal fluctuations. Additionally, sensor directionality and spatial resolution constitute critical evaluation criteria. Applications such as medical ultrasound imaging, auscultation localization, or individual voice recognition in complex noise environments benefit significantly from specialized sensor arrays designed to enhance directional sensitivity and spatial discrimination,

thus enabling precise acoustic sensing.

Acoustic impedance matching is another critical design consideration for acoustic systems, aimed at maximizing the efficiency of acoustic energy transmission by minimizing reflection losses at material interfaces. In bioacoustics applications, particularly in medical ultrasound and wearable acoustic sensors, the inherent impedance mismatch between conventional sensor materials and biological tissues necessitates strategies such as integrating specialized acoustic windows or employing multilayered gradient-impedance structures. Alternatively, the acoustic impedance of the sensor materials can be tailored by incorporating fiber-reinforced composites or microsphere-embedded architectures that increase porosity to reduce bulk density. Such material modifications effectively reduce intrinsic acoustic impedance, thereby enhancing acoustic coupling efficiency and minimizing reflective losses.[161]

Bioacoustics sensors are increasingly advancing toward wearable and flexible form factors, particularly in applications such as health monitoring and medical implants, where biocompatibility becomes a central performance criterion. In certain scenarios, partial compromises in sensing performance may be necessary to ensure safety. For instance, skin-mounted sensors designed for infant bowel sound monitoring must utilize hypoallergenic materials and may require antibacterial surface coatings to minimize skin irritation and infection risks.[162] For implantable or minimally invasive ultrasonic transducers, inert encapsulation and immunological inertness are essential to avoid foreign body responses. Besides, mechanical compliance is also a critical

component of biocompatibility; flexible acoustic sensors should accommodate deformation to conform to curved anatomical surfaces and adapt to dynamic bodily movements. In continuous monitoring scenarios, long-term stability emerges as another key evaluation metric. This includes electrical and mechanical stability to prevent performance degradation over time due to material aging, wear, or signal drift. Strategies to enhance durability and operational lifespan include material optimization, fatigue-resistant structural design, and multilayer encapsulation for environmental protection.

The final system-level consideration is the integrated signal processing capability, which refers to the acoustic sensing system capable of coordinating hardware, software, and algorithmic modules to perform signal conditioning, acquisition, transmission, processing, and interpretation within a unified architecture. At the hardware level, application-specific acquisition circuits should be developed to support different sensing mechanisms while also containing real-time data integration and transmission across multiple channels. For example, when incorporating additional sensors such as inertial measurement units (IMUs) for motion artifact suppression introduces further demands on the hardware for seamless synchronization and fusion of heterogeneous signal streams.[163] On the software side, the system should support both time-domain and frequency-domain signal analysis, enabling robust feature extraction as well as machine learning (ML) -assisted classification and recognition of bioacoustics patterns. In wearable and portable platforms, to reduce transmission burden, the system can perform local edge processing prior to data transfer through the integration of compact

microcontroller units (MCUs). This approach reduces communication latency and minimizes energy usage by offloading essential signal processing tasks directly to the sensor node. To ensure practical deployment, such functionality must be balanced against constraints on sampling rate, algorithmic complexity, and local data storage, especially under resource-limited operating conditions.

Once the performance requirements under specific application scenarios are identified, the selection of appropriate acoustic sensing mechanisms and active materials can be made in a more targeted manner, and sensor structures can then be designed accordingly based on the intended parameter ranges. For instance, in applications requiring flexibility and high-frequency response, piezoelectric polymers such as PVDF are often prioritized due to their mechanical compliance and fast response. In contrast, bioinspired designs incorporating microstructure piezoresistive sensors can offer frequency selectivity through structural tuning for artificial cochlea applications.[164] In scenarios demanding spatial resolution, miniaturized sensor arrays are typically realized using MEMS-based architecture. In the following sections, we provide a comprehensive review and comparison of existing acoustic sensors concerning their underlying mechanisms, material systems, structural designs, and recent advances.

2.4.3 Evaluation strategies for performance

Mannequin-simulated sounds

Physiological signals are characterized by their transient, sporadic, and non-repeatable nature, which presents significant challenges for the objective evaluation of acoustic

sensor performance. In practice, physiological signals vary not only between individuals but also within the same subject under different physiological or emotional states. Therefore, during sensor design, optimization, and iterative development, it is essential to obtain reliable, repeatable, and physiologically relevant signal inputs for meaningful performance assessment. Moreover, system-level evaluations should closely approximate vivo wearing conditions, ensuring that simulated body sounds propagate through media with acoustic properties similar to human tissues. This minimizes signal distortion caused by scattering or attenuation at the interface between the sensor and the skin.

To meet these requirements, high-fidelity auscultation mannequin offers an ideal solution for mimicking the generation and transmission of physiological acoustic signals within the human body which is essential for benchmarking sensor performance under controlled and repeatable conditions. These manikins, commonly used in medical education and clinical competency training, act as programmable “standardized patients.” They are equipped with pre-recorded audio libraries of heart, breath, lung crackles, and bowel sounds, which can be selectively played at anatomically accurate auscultation points. They provide standardized and repeatable sound sources by enabling programmable playback, critical for comparative sensor testing. In addition, the outer materials of these mannequins such as medical-grade silicone, are often selected to closely match the acoustic impedance of human skin, thereby simplifying the design of the acoustic coupling interface for wearable sensors.

The earliest high-fidelity mannequin dates back to 1968, developed for cardiovascular training with capabilities such as carotid pulse simulation and controllable heart and respiratory sounds.[165] Modern systems, enabled by advances in digital media and simulation technology, now support programmable multi-system physiological signal outputs, thereby enabling comprehensive evaluation of a sensor's performance. For instance, the Lung Sound Auscultation Trainer “LUNG” ver.2 (Kyoto Kagaku Co. Ltd., Kyoto, Japan) integrates five independently programmable lung sound modules distributed across different thoracic zones. (**Fig. 2.16a**) The system contains a variety of lung sound scenarios and supports synchronized heart sounds as background, creating a clinically realistic, composite acoustic environment. Further developments in high-fidelity auscultation manikins have led to the emergence of advanced, multimodal platforms such as SimMan 3G Plus (Laerdal Medical), which now offer a mature integration of multi-organ systems, including cardiac, respiratory, and gastrointestinal modules. These platforms enable customizable and programmable playback of physiological sounds, allowing researchers to emulate a broad spectrum of clinical scenarios with high temporal and spectral fidelity. Importantly, their modular configuration supports the synchronized output of multiple signal types across anatomically distributed locations, enabling realistic signal superposition and interference patterns. This level of programmability facilitates comprehensive benchmarking of acoustic sensor performance, including sensitivity, signal discrimination, crosstalk resistance, and multi-source resolution under repeatable and physiologically relevant conditions.

Human subject validation

High-fidelity mannequins provide controllable, repeatable, and standardized physiological sound sources for acoustic sensor evaluation. By providing ground-truth audio inputs with known spectral and temporal characteristics, they facilitate rigorous, quantitative validation of acoustic sensors during early-stage development and calibration. However, human subject testing remains a critical step toward clinical translation, as it enables validation of sensor performance under real-world conditions. By benchmarking against clinical gold standards, such testing reveals practical challenges such as skin–sensor coupling stability, motion artifacts, inter-individual variability, and long-term wearability. Beyond confirming functional effectiveness, human testing also provides valuable insights from both a technical and user experience perspective, guiding iterative optimization of sensor design for real-life applications.

During human testing of acoustic sensors, it is essential to evaluate their ability to monitor physiological sounds across a range of anatomical sites and subject conditions. By placing the sensor on specific body locations, bioacoustics signals such as heart sounds, breath sounds, swallowing, pulse, and bowel activity can be captured. To assess inter-individual adaptability, subject cohorts should span a broad demographic spectrum including variations in age, sex, body habitus, and health status. For instance, Rogers and colleagues demonstrated a wireless, broadband acoustic-mechanical sensing network that enabled pulmonary function assessment in individuals with chronic lung disease (n=55), as well as continuous monitoring of respiratory and

gastrointestinal activity in neonates admitted to intensive care units (n=15) **(Fig. 2.16b)**. In the chronic lung study, sensing modules were strategically placed on predefined anatomical landmarks to capture lung acoustics during respiration in both healthy volunteers (n=20) and patients (n=35). Notably, representative recordings from neonatal ICU patients were benchmarked against FDA-approved clinical monitors, confirming the accuracy of physiological parameter extraction under clinical conditions.

Beyond static recordings, human trials should also capture physiological signals during both resting and dynamic states to reflect real-world variability and assess sensor robustness under motion because variations in body movement, posture, and activity can influence signal fidelity. An illustrative example is shown in **Fig. 2.16c**, where heart sounds were recorded across multiple activity states (quiet sitting, talking, walking, and jogging). The device maintained clean acoustic signals with negligible motion artifacts, enabled by its soft form factor and skin-conformal design. Such soft materials help accommodate skin-device contact variations during motion, minimizing acoustic impedance mismatches between the epidermis and the microphone diaphragm and suppressing high-frequency noise due to locomotion or vocalization.

In summary, human subject validation should evaluate not only technical parameters such as SNR, amplitude response, and dynamic robustness, but also resistance to motion artifacts and ambient noise. Validation against clinical-grade equipment ensures output accuracy, while subject diversity across age, sex, body type, and health status supports generalizability. Incorporating both healthy and pathological cohorts further

enhances the sensor's translational value for personalized and diagnostic healthcare applications. When combined with programmable auscultation mannequins that offer controllable and repeatable acoustic benchmarks, in vivo human testing provides a comprehensive framework for assessing sensor performance across both standardized and real-world physiological scenarios.

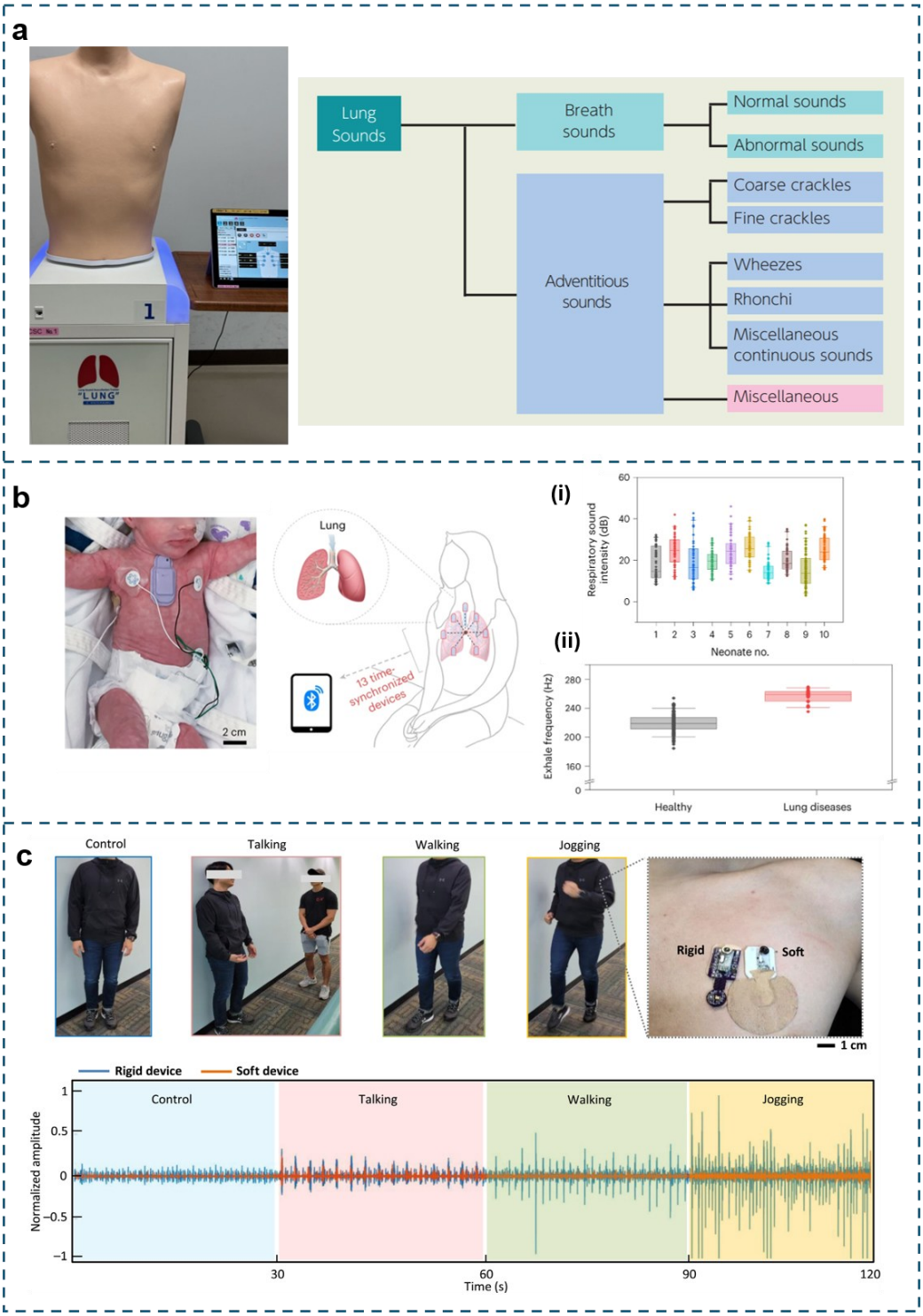

Fig. 2.16 (a) Lung Sound Auscultation Trainer "LUNG" ver.2, a mannequin simulator for lung sound auscultation. (b) Wireless acoustic monitoring systems for neonatal respiration and chronic pulmonary disease patients; (i) Monitoring respiratory sound intensity in ten neonates in the neonatal intensive care unit (NICU) (ii) Comparative

respiratory rate monitoring between healthy subjects and chronic pulmonary disease patients. (c) Comparison of signal amplitudes between soft acoustic sensors and rigid devices under static and dynamic conditions, demonstrating noise immunity and motion artifact suppression capabilities.

CHAPTER 3 FABRICATION AND CHARACTERIZATION OF DURABLE AND STABLE HIGHLY ALIGNED PIEZOELECTRIC NANOFIBER MEMBRANES FOR ACOUSTIC SENSING

3.1. Introduction

With the rapid development of wearable electronics, various flexible sensors have emerged for physiological and healthcare monitoring.[166-170] Among them, acoustic sensors designed to capture bioacoustic signals from different physiological signals have received increasing attention.[171-174] A central challenge in this field lies in engineering high-performance, flexible sensing elements that serve as the core components of wearable acoustic systems.[175, 176]

Among the various transduction mechanisms, piezoelectric sensing stands out for its fast response, tunable characteristics, and self-powered operation, making it highly attractive for wearable acoustic applications.[177-179] Most commercial piezoelectric stethoscopes rely on inorganic piezoelectric ceramics (BTO and PZT), which despite their excellent performance, are inherently rigid and brittle, limiting their compatibility with flexible systems.[60, 180] Some products have adopted dense PVDF films, but pristine PVDF typically requires extra stretching and electrical poling to induce sufficient β-phase content, complicating fabrication and limiting sensitivity.[181, 182] Therefore, there is an urgent need to develop new piezoelectric films that combine low modulus, excellent conformability, and high electromechanical conversion efficiency, to enable the construction of next-generation flexible and sensitive acoustic transducers.

Compared with pure PVDF, its copolymers often exhibit higher piezoelectric activity and show greater potential in piezoelectric, ferroelectric, and fabrication aspects for applications in acoustic devices.[183, 184] However, the piezoelectric parameters of these polymers are still significantly lower than those of ceramic-based materials. Therefore, many recent studies have adopted composites of flexible piezoelectric polymers and ceramic fillers, which can maintain mechanical flexibility while achieving relatively high piezoelectric performance.[185, 186] Meanwhile, the piezoelectric voltage constant (g_{33}) should also be taken into consideration during design.[187, 188] Therefore, maintaining a low dielectric constant is crucial for obtaining a higher electrical output and improving sensitivity. When a flexible membrane is subjected to acoustic pressure, the generated mechanical deformation mainly appears as in-plane stretching rather than out-of-plane compression. As a result, the d_{31} mode is more relevant for piezoelectric acoustic or vibration sensing than the d_{33} mode. Furthermore, introducing anisotropy in the piezoelectric film can enhance directional sensitivity in specific orientations, which provides better selectivity when detecting regionally distributed physiological signals.

Based on these considerations, this chapter designs oriented piezoelectric composite membranes via electrospinning, using a terpolymer P(VDF-TrFE-CFE) (PVDF-TER) as the matrix and incorporating a controlled amount of BTO nanoparticles. The electrospun fibers are further stretched during the collection process to obtain obvious orientation and enhanced d_{31} working performance. Under the high electric field during electrospinning, the molecular chains undergo rearrangement, enabling the formation

of polar phases without additional poling treatment. This chapter also investigates that the enhancement of piezoelectric performance by BTO doping does not originate from the intrinsic piezoelectricity of the ceramic itself, but rather from the synergistic effect of heterogeneous nucleation and interfacial polarization. Focusing on the relationship between structure, polar phase, and performance, we systematically study the effects of electrospinning parameters on the orientation and crystallinity of PVDF-TER/BTO composite membranes. Quantitative characterizations are conducted using multiple techniques, and the mechanical and physical properties are also evaluated, laying the foundation for subsequent device design. Finally, comprehensive tests of d_{31}, d_{33}, and dielectric constant are performed, and the contribution of fiber alignment to directional sensitivity is further clarified through in-plane strain response analysis. This work provides a feasible material and fabrication route for the development of next-generation skin-conformal acoustic transducer units and offers support for the design of wearable physiological sound sensing devices.

3.2. Experimental section

3.2.1 Materials

P(VDF-TrFE-CFE) powders (ratio 64:27:9, M_w =3 00 000–4 00 000 g/mol, Piezotech ® FC); PVDF powders (*Mw* = 275000 g/mol, Macklin); $BaTiO_3$ particles (99.9% trace metals basis, diameter < 100 nm, Macklin); N, N-dimethylformamide (DMF), acetone were purchased from Sigma-Aldrich. The silicone elastomer base and related curing agent for Polydimethylsiloxane (PDMS, SYLGARD® 184) were bought from Dow Chemical Company (USA).

3.2.2 Preparation of Precursor Solution

P(VDF-TrFE-CFE) powders were dissolved in a solvent mixture of DMF and acetone (volume ratio 6:4) to prepare solutions with polymer concentrations of 12%, 15%, and 18% (w/v) to detect the optimized concentration. The mixtures were stirred at 50 °C for 5 h to obtain homogeneous PVDF-TER solutions. Subsequently, various amounts of $BaTiO_3$ nanoparticles (0 to 24 wt% in 4 wt% increments) were added to the superior PVDF-TER solution (18%) to prepare composite suspensions. Each suspension was stirred for 7 h, followed by ultrasonic treatment for 1 h with water replacement every 15 min to avoid thermal buildup. Solutions of pure PVDF and PVDF-TER without $BaTiO_3$ were prepared under the same conditions for comparison. All controlling parameters for processing fibrous membranes with various solution contents and doping ratios are listed in **Table 3.1**.

Table 3.1 The control parameters for fabricating fibrous nanofiber membranes.

P / S	V (kV)	C (%)	H (%)	T (℃)	D (%)
1	12	12	50	25	0
2	15	12	50	25	0
3	18	12	50	25	0
4	18	15	50	25	0
5	18	18	50	25	0
6	18	18	30	50	0
7	18	18	30	50	4
8	18	18	30	50	8
9	18	18	30	50	12
10	18	18	30	50	16
11	18	18	30	50	20
12	18	18	30	50	24

P: parameters; **S:** Samples; **V:** Voltage; **C:** the concentration of polymers; **H:** humidity during electrospun; **D:** doping ratio of the BTO.

3.2.3 Fabrication of the fibrous membrane via electrospinning

10 mL of the above precursor solution will be transferred into a syringe with a stainless-steel needle with a diameter of 0.22 mm. During the process of electrospinning, a fixed potential of 18 kV, a stable velocity of 0.5 mL h^{-1} are set up to get the fibrous membranes. To prepare the random and highly oriented nanofibers for comparison, the collection roller is set for different rotating speeds of 100 and 2600 rpm, with a 15 cm distance between the needle and the collector. Then the composite fibrous film will be dried at 65 °C in an oven to completely evaporate the solvent and further annealed at various temperatures below its melting points to promote crystallinity. The electrodes

were first fabricated utilizing physical vapor deposition (PVD) technique (The Mat400, MAT Dresden) by depositing copper on both sides of the fibrous membrane to form the MIM structure. To increase the compactness of fibrous membranes and electrodes, the samples were hot-pressed at 10 MPa under 30°C. After electrode integration, the films were encapsulated using polydimethylsiloxane (PDMS) at a prepolymer-to-curing agent weight ratio of 10:1 for subsequent electrical measurements. The working flow for fabricating high-oriented nanofiber membrane is shown in **Fig. 3.1**.

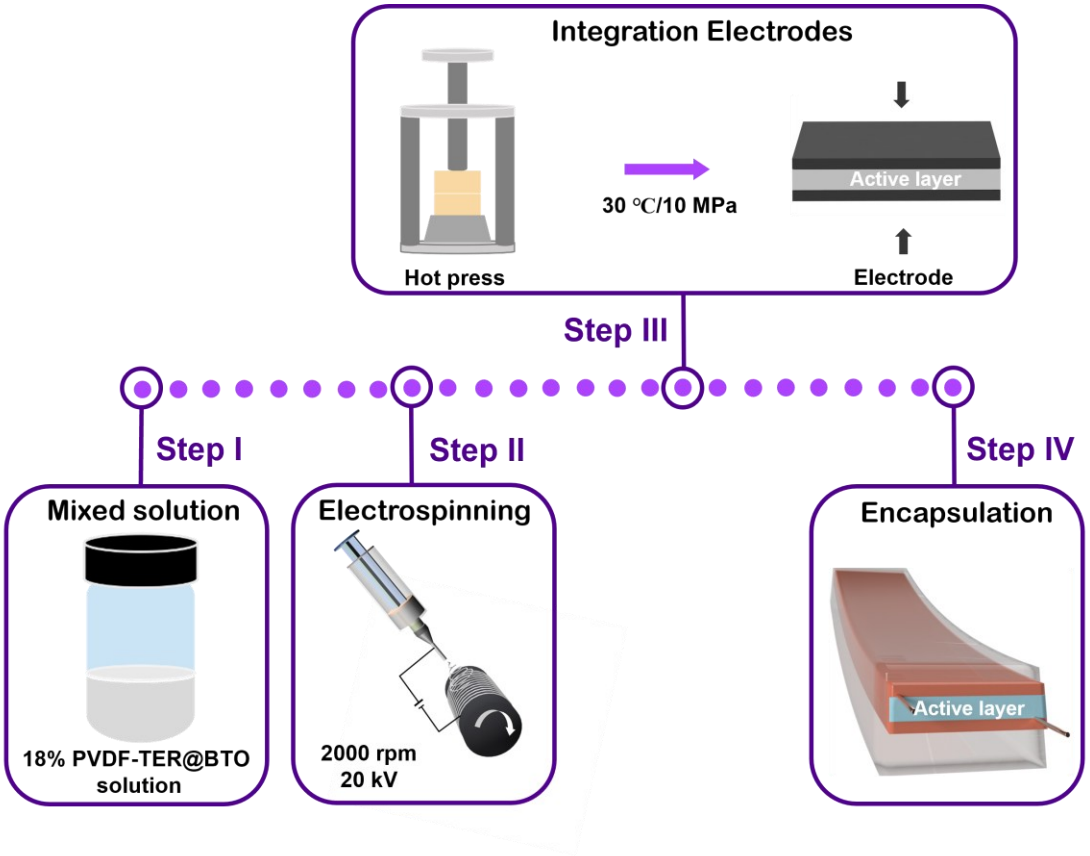

Fig. 3.1 Schematic diagram of fabrication of high-oriented nanofiber film via electrospinning.

3.2.4 Characterization and Measurements

Morphology and characterizations

The morphology of the fibrous membrane was characterized using a Scanning Electron Microscope (SEM, Tescan VEGA3, from Brno, Czech Republic) to confirm the alignment degree and diameters of nanofibers. Energy dispersive X-ray spectroscopy (EDS) was employed to explore the uniform distribution of BTO nanoparticles.

The molecular structure in fibrous membrane was measured by Fourier-transform infrared spectroscopy (FTIR, Perkin-Elmer Spectrum GX, USA) in the range of 650–2000 cm^{-1} with a resolution of 4 cm^{-1} over 32 scans. The calculated content of β phase can be calculated as:

$$F(\beta) = \frac{A_\beta}{1.26A_\alpha + A_\beta}$$

where the A_α and A_β are the absorbance of vibration peaks at 764 cm^{-1} (α-phase) and 840 cm^{-1} (β-phase) of the PVDF-Trfe-CFE.

X-ray diffractometer (XRD, Rigaku SmartLab 9kW - Advance) was used to examine the crystal plane corresponding to the diffraction peak of the aligned and random nanofibers and further confirm the second stretching during the fabrication process promotes the all-trans configuration. By utilizing the broadening effect of diffraction peaks from XRD data, the apparent crystallite size (L) can be calculated with the Scherrer formula:

$$L = 0.9\lambda/(B\cos\,\theta)$$

where λ is the X-ray wavelength, B is the full width at half maximum (FWHM) of the

diffraction peak, and θ is the Bragg angle.

Differential Scanning Calorimetry (DSC, Mettler Toledo DSC3) was scanned at a temperature range of –50 ℃ –300 ℃ with the heating rate of 5℃/min under nitrogen atmosphere. Through DSC scanning, the melting points (T_m) and melting enthalpies (ΔH_m) before and after doping with BTO were determined then the crystallinity of the polymers was further calculated for comparison.

To quantitatively evaluate the degree of orientation and structural anisotropy in the aligned films, Grazing-Incidence Wide-Angle X-ray Scattering (GIWAXS) were performed with X-ray incident beams aligned both parallel and perpendicular to the fiber orientation direction. The scattering vector range (q) was set from 0.1 to 2.2 $Å^{-1}$. After confirming the anisotropy of the nanofibers through the 2D-GIWAXS diffraction arcs in two directions, the degree of orientation was quantitatively determined by calculating the Herman orientation factor (*f*). The azimuthal integration of the main peak range (around 1.4 $Å^{-1}$) was performed within the range of ±90°, and through the following formula:

$$f = \frac{3(\cos^2 \phi) - 1}{2}$$

Mechanical properties test: The mechanical properties were measured at a tensile rate of 10mm/min with the Instron 5944, USA. The bulk density and porosity of the films was calculated by the following equations:

$$Density\ (g/cm^3) = \frac{mat\ mass\ (g)}{mat\ thickness\ (cm) \times\ mat\ area\ (cm^2)}$$

$$Porosity\ (\%) = (1 - \frac{\rho_{sample}}{\rho_{material}}) \times 100\%$$

Piezoelectric properties test

For conventional quasistatic method was realized with Quasi-static Piezoelectric d_{33} Meter (ZJ-3). For the single fiber d_{33} value was calculated with the Piezoelectric force microscopy(PFM, Asylum Research, USA) in dual AC resonance tracking (DART) mode, with Pt-coated conductive probes.

To obtain the d_{31} piezoelectric coefficient, the indirect method was performed with the following setup by tensile instruments. The sample was clamped between the two clamps, and the tensile instrument applied the definite tensile stress. The transient transfer charge was recorded by the Keithley 6517B connected with the NI card (NI - 9234) for data collection.

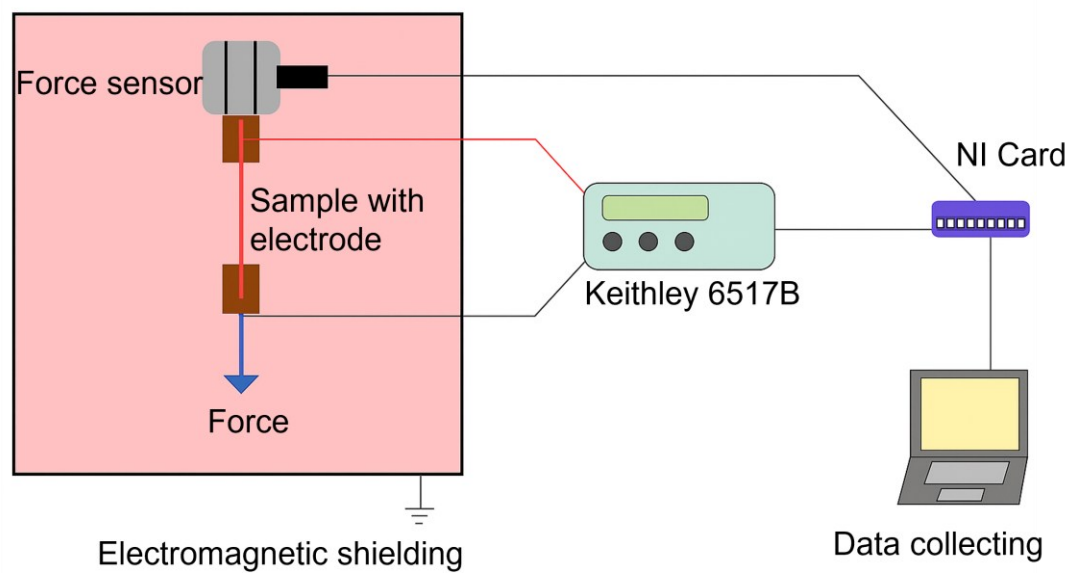

Fig. 3.2 Schematic illustration of the tensile testing setup for determining the piezoelectric coefficient d_{31}.

3.3. Results and discussion

The sensing performance of electrospun PVDF-TER@BTO nanofiber membranes is primarily attributed to their intrinsic piezoelectric properties. In line with the piezoelectric working modes discussed in Chapter 2, both the d_{33} and d_{31} working modes are considered in the design of acoustic sensing units, which impose stringent requirements on the fabrication process of electrospun membranes. Specifically, the formation of highly aligned nanofibers via high-voltage electrostatic fields and rapid jet stretching is essential for enhancing the d_{31} piezoelectric coefficient. Theoretically, the morphology, crystallinity, and piezoelectric performance of electrospun membranes can be optimized through controlled processing parameters. In this section, a systematic investigation of key electrospinning parameters, including solution concentration, applied voltage, piezoceramic doping content, and collector speed, was conducted. Through quantitative analysis of parameter variations, highly aligned electrospun PVDF-TER@BTO membranes were successfully fabricated. Subsequent characterization focused on evaluating their intrinsic properties, including surface morphology, degree of fiber alignment, crystallinity, porosity, and mechanical performance. Finally, the piezoelectric coefficient of the membranes was quantified using both direct and indirect measurement methods to ensure the reliability of the acoustic sensing units.

3.3.1 Construct highly aligned nanofiber membranes

The concentration of the polymer solution plays a critical role in determining the

morphology, continuity, and film-forming quality of electrospun nanofibers. Additionally, to achieve highly aligned fibrous membranes, secondary stretching is introduced via a high-speed rotating collector, which also promotes the formation of the all-trans (*TTTT*) configuration in PVDF-TER chains.

A systematic investigation was first conducted to assess the effects of polymer concentration and collector rotation speed on the morphology of electrospun nanofibers, as shown in **Fig. 3.2**. Overall, both parameters exert significant influence on the characteristics of the resulting fibrous membrane, particularly in controlling fiber diameter and uniformity. As shown in **Fig. 3.3a–c**, increasing the polymer concentration from 12% to 15% and 18% results in a morphological transition from droplets and beaded structures to uniform and continuous nanofibers under the electric field, owing to enhanced chain entanglement.

Subsequently, the effect of different collector rotation speeds was investigated under a fixed polymer concentration of 18%. SEM images of classic electrospun membranes collected at various rotation speeds are shown in **Fig. 3.3d–f**, and the corresponding fiber diameter and distributions are presented in **Fig. 3.3g–i**. As the collector speed increased, the nanofibers underwent greater secondary stretching during deposition, leading to a progressive reduction in diameter and enhanced alignment degree. At 2500 rpm, the fibers exhibited well-aligned orientation with an average diameter of approximately 780 nm. Notably, fiber stacking and adhesion were observed at lower collection speeds. In contrast, under identical humidity conditions (30% RH), such

adhesion was absent in membranes collected at high speed. This improvement is attributed to the smaller fiber diameter and increased surface area, which collectively promote more efficient solvent evaporation.

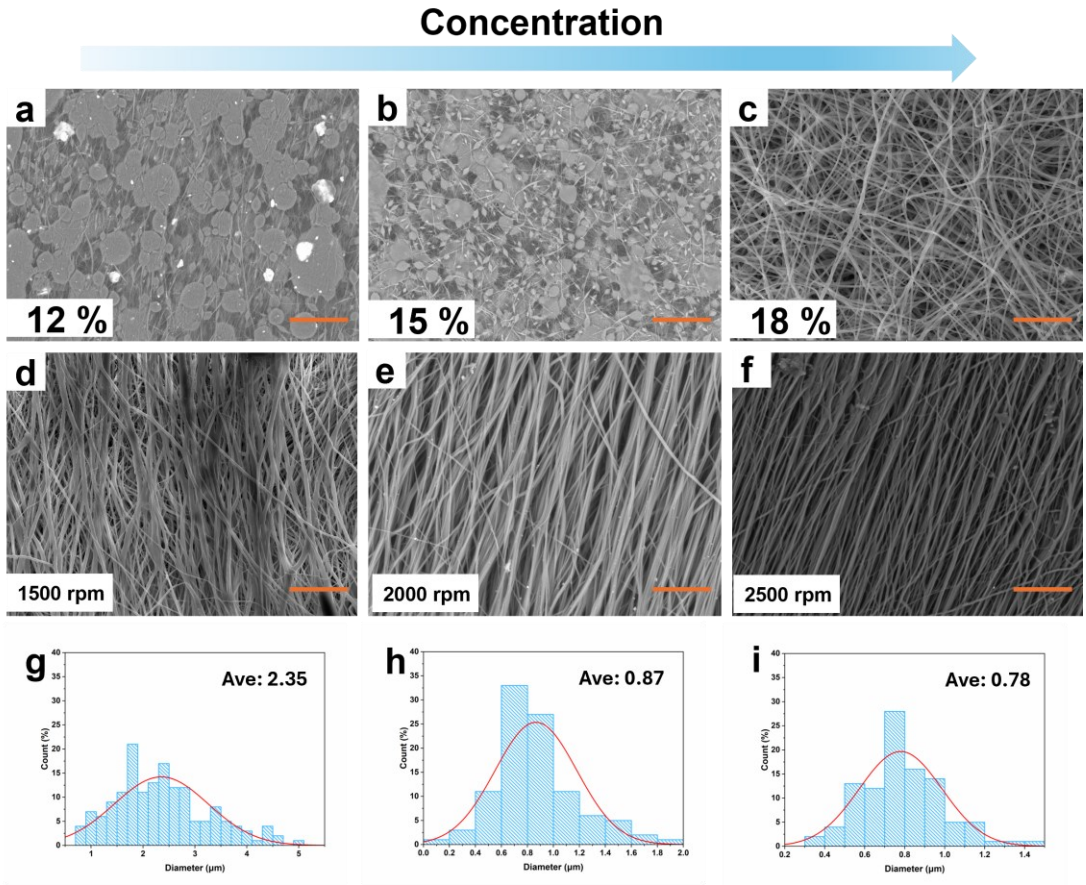

Fig. 3.3 (a), (b), and (c) are typical morphology pictures via SEM of the nanofiber membranes with variable content of polymer solutions from 12% to 18%; (d), (e), and (f) are the oriented nanofibers with different collection speeds and humidity; (g), (h), and (i) are the diameter and distribution of the above corresponding nanofibers. (Scalebar: 50 μm)

With the optimal parameters for producing oriented nanofibers established, the next step was to examine whether the alignment of electrospun films, either aligned or

randomly oriented, affects the crystallinity and polar phase formation of the polymer. As shown in **Fig. 3.4a**, XRD spectra were conducted on both randomly oriented and aligned nanofibers fabricated under identical electrospinning conditions. Compared with the randomly oriented fibers (red curve), the aligned fibers (green curve) exhibit a pronounced increase in peak intensity and a narrowing of the peak width at the 110,200 reflections. This indicates that the secondary stretching alignment process can significantly enhance the polymer crystallinity and β-phase diffraction. Using the Scherrer equation, the apparent crystallite sizes were estimated to be 38 nm and 27 nm for the aligned and randomly oriented fibers, respectively, suggesting that alignment promotes the structural integrity of the crystalline domains. In addition, as the polymer chains are straightened during the alignment process, compression perpendicular to the crystal planes (Poisson effect) causes a slight shift of the main peak toward higher diffraction angles.

After confirming the promoting effect of orientation on the polar phase in the polymer，the next focus was on investigating the doping concentration of the inorganic piezoelectric ceramic BTO. As previously discussed, a quantitative amount of doped piezoelectric ceramic can enhance the overall piezoelectric performance of electrospun films, whereas excessive doping may adversely affect both their mechanical and piezoelectric properties. Therefore, selecting appropriate doping concentration is critical. In this study, PVDF-terpolymer was used as the matrix, and BTO nanoparticles were incorporated at concentrations ranging from 0 to 24 wt% in increments of 4 wt% to fabricate highly oriented electrospun films. These films underwent a series of

subsequent characterizations to determine the optimal doping concentration. For brevity, the samples are hereafter denoted as PVDF-TER@BTO_x, where x represents the doping concentration. **Fig. 3.4b, c** present the FTIR spectra of aligned and non-aligned terpolymer films with varying BTO doping ratios, along with the corresponding calculated fraction F_β (β phase content) to quantitatively assess the proportion of all-trans configuration ($T_{m>3}$) which corresponds to the characteristic peak at 848 cm^{-1} while the peak at 768 cm^{-1} is associated with the TGTG′ configuration. It is evident that fiber alignment induces the formation of the all-trans crystalline phase. As the BTO doping level increases, the β-phase content first rises and then decreases; within the range of 4–16 wt% BTO. This is because the heterogeneous nucleation and the high dielectric constant of BTO promote β-phase formation via interfacial polarization. When come to higher doping levels, the decline in F_β is attributed to BTO aggregation and restricted polymer chain mobility, which reduce the overall crystallinity. Consequently, the optimal BTO doping level was determined to be 16 wt%, and all subsequent studies were conducted using this concentration. Although incorporating BTO enhances the piezoelectric response of the composite nanofibers, the intrinsic high piezoelectric coefficient of bulk BTO is not directly translated into output due to polymer encapsulation, multidomain structures, and limited poling conditions. Instead, under the influence of the electrospinning field and alignment process, the BTO/PVDF-TER interface forms nanoscale interfacial layers or pores, which undergo Maxwell-Wagner-Sillars (MWS) interfacial polarization coupled with strain under subtle pressure. This generates additional dipoles at the interface, which align along the fiber

axis and become the primary source of the enhanced piezoelectric effect in the composite (**Fig. 3.4e**).

To further verify the positive effect of BTO doping, DSC measurements were performed on nanofibers before and after 16 wt% BTO incorporation, as shown in **Fig. 3.4d**. For the undoped sample, the melting temperature (T_m) was 131.1 °C with a melting enthalpy (ΔH_m) of 27.06 J/g. After doping, the T_m was 130.7 °C, indicating that the lamellar thickness distribution remained essentially unchanged. The ΔH_m increased to 29.83 J/g (polymer reference basis). The DSC-derived crystallinity values (X_c) were calculated to be 46.6% and 49.6% for the undoped and doped samples, respectively, further confirming that heterogeneous nucleation by BTO promotes the perfection of crystallization.

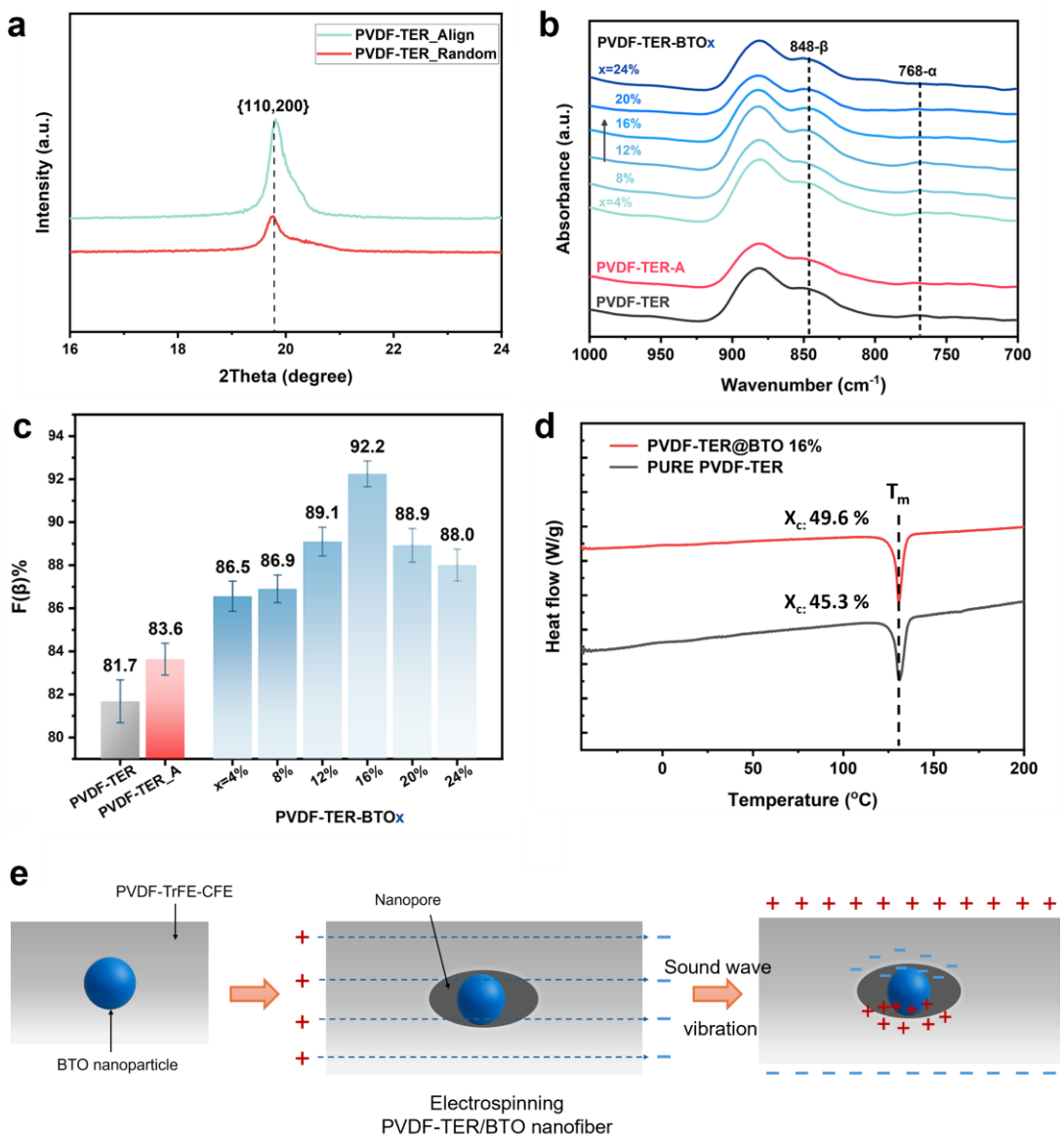

Fig. 3.4 (a) The XRD spectrum of the nanofibers of PVDF-TER random, aligned membranes. **(**b) The FTIR spectrum of the PVDF-TER nanofibers with gradient-content BTO doping (from 0–24% doping ratio, 4% as gradient). (c) The calculated crystallization of β-phase content corresponding to the FTIR spectrum. (d) The DSC (heating rate of 10 K/min) curve of the pure PVDF-TER and PVDF-TER doping with 16% BTO electrospun membranes and corresponding calculated crystallinity. (e) Schematic illustration of the BTO incorporation enhances the performance of composite piezoelectric polymers.

To further investigate the molecular and crystalline orientation of the BTO-doped PVDF-TER aligned nanofiber films, grazing-incidence wide-angle X-ray scattering (GIWAX) characterization was conducted. This technique enables a quantitative assessment of the degree of orientation and visualizes the anisotropy of electrospun membranes through diffraction patterns. As illustrated in **Fig. 3.5a**, a coordinate system was established for both the aligned nanofiber film and a single fiber, with the X-ray beam incident either parallel or perpendicular to the fiber from the in-plane direction to probe orientation. As shown in **Fig. 3.5b**, the diffraction pattern exhibits sharp and intense arcs near the equator, indicating that molecular chains within the fibers are aligned well along the stretching direction during the fabricating process. In contrast, **Fig. 3.5c** shows no distinct arcs, highlighting the clear anisotropy of the film and confirming that the fibers are oriented along the axial direction. Furthermore, analysis of the 1D WAXS curves in **Fig. 3.5d** revealed that the diffraction intensity parallel to the fiber direction is approximately 4.5 times higher than that perpendicular to the fiber direction, further evidencing a pronounced uniaxial structure. To quantitatively evaluate the fiber orientation, azimuthal integration I(χ) was performed over the annular diffraction corresponding to the main peak at q≈1.4 $Å^{-1}$ (parallel to the fiber axis) within the range of ±90°, and the Herman's orientation factor (*f*) was calculated to be 0.704. In theory, *f* approaches 0 for a randomly oriented structure and approaches 1 for a perfectly uniaxially aligned structure. This quantitative result confirms the highly oriented nature of the electrospun film, laying a solid foundation for its subsequent piezoelectric performance.

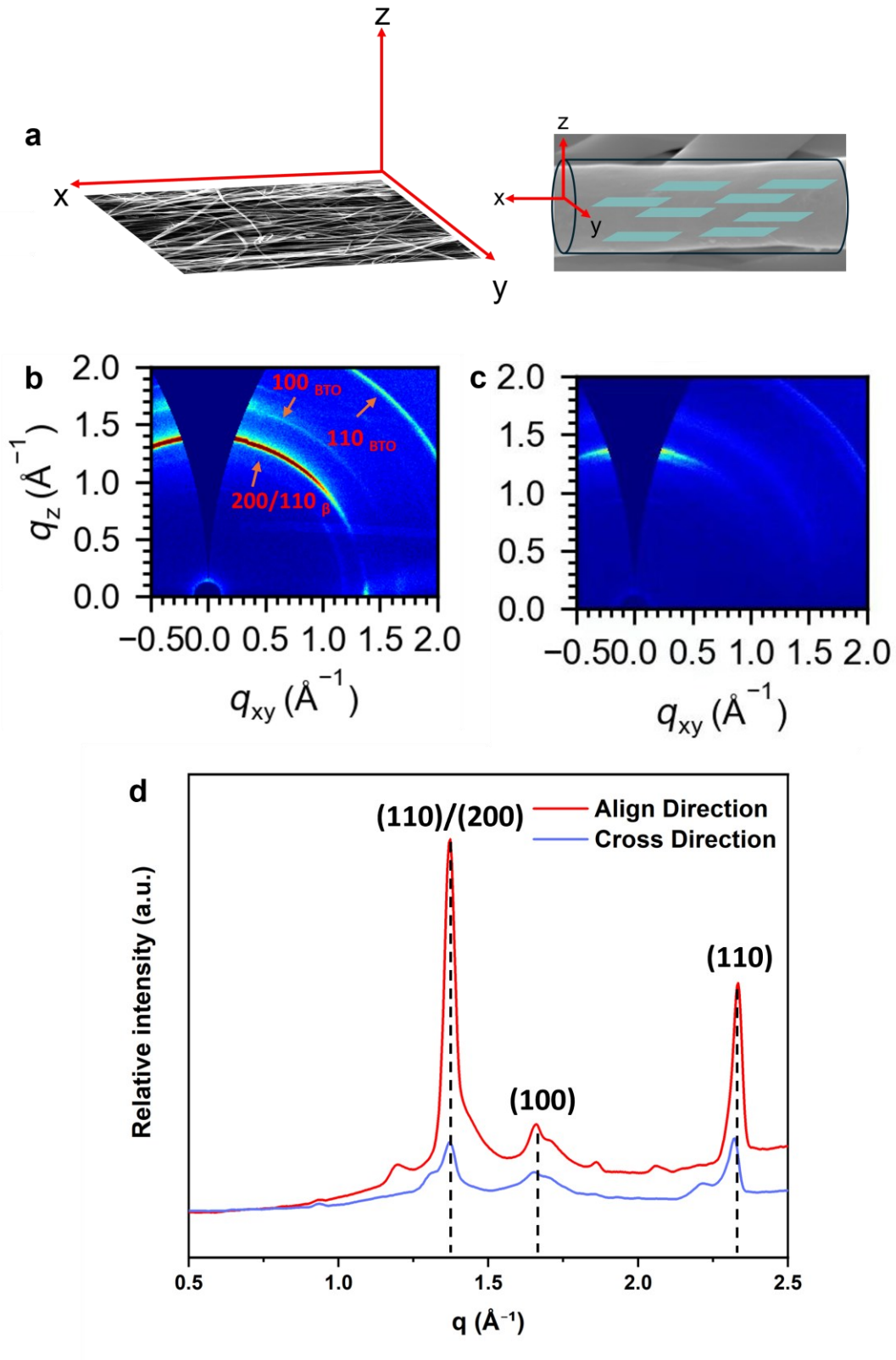

Fig. 3.5 (a) Schematic diagram of the coordinate axes for the PVDF-TER/BTO_{16} nanofiber film and a single fiber. (b) and (c) 2D GIWAX patterns with the incident X-

ray beam parallel to and perpendicular to the fiber axis, respectively. (d) 1D GIWAX curve showing the 110/200 diffraction plane (β phase) of PVDF-TER and the tetragonal phase of the BTO nanoparticles.

3.3.2 Morphologies and mechanical properties

With the alignment of the nanofiber membrane determined, the morphology is further explored. As shown in **Fig. 3.6a**, the surface morphology was studied by atomic force microscopy (AFM). Within the scanned region, the fibers form effective "ridges and valleys" along the alignment direction, further confirming the anisotropy of the film. The surface roughness (R_a) was measured to be 141 nm, arising from the stacking of aligned fibers. In the phase mapping image, the bright regions exhibit a strip-like morphology aligned with the fiber orientation, indicating that the crystalline domains are distributed along the fiber axis (**Fig. 3.6b**). The SEM images (**Fig. 3.6c and d**) reveal the well-aligned fibers and the embedding of BTO nanoparticles within the nanofibers, forming small ferroelectric domains along the fiber orientation. This observation further confirms the previously discussed heterogeneous nucleation and pore-induced interfacial polarization. Correspondingly, EDS mapping analysis shows that the $BaTiO_3$ fillers are well-dispersed without large-scale aggregation (**Fig. 3.6e and f**).

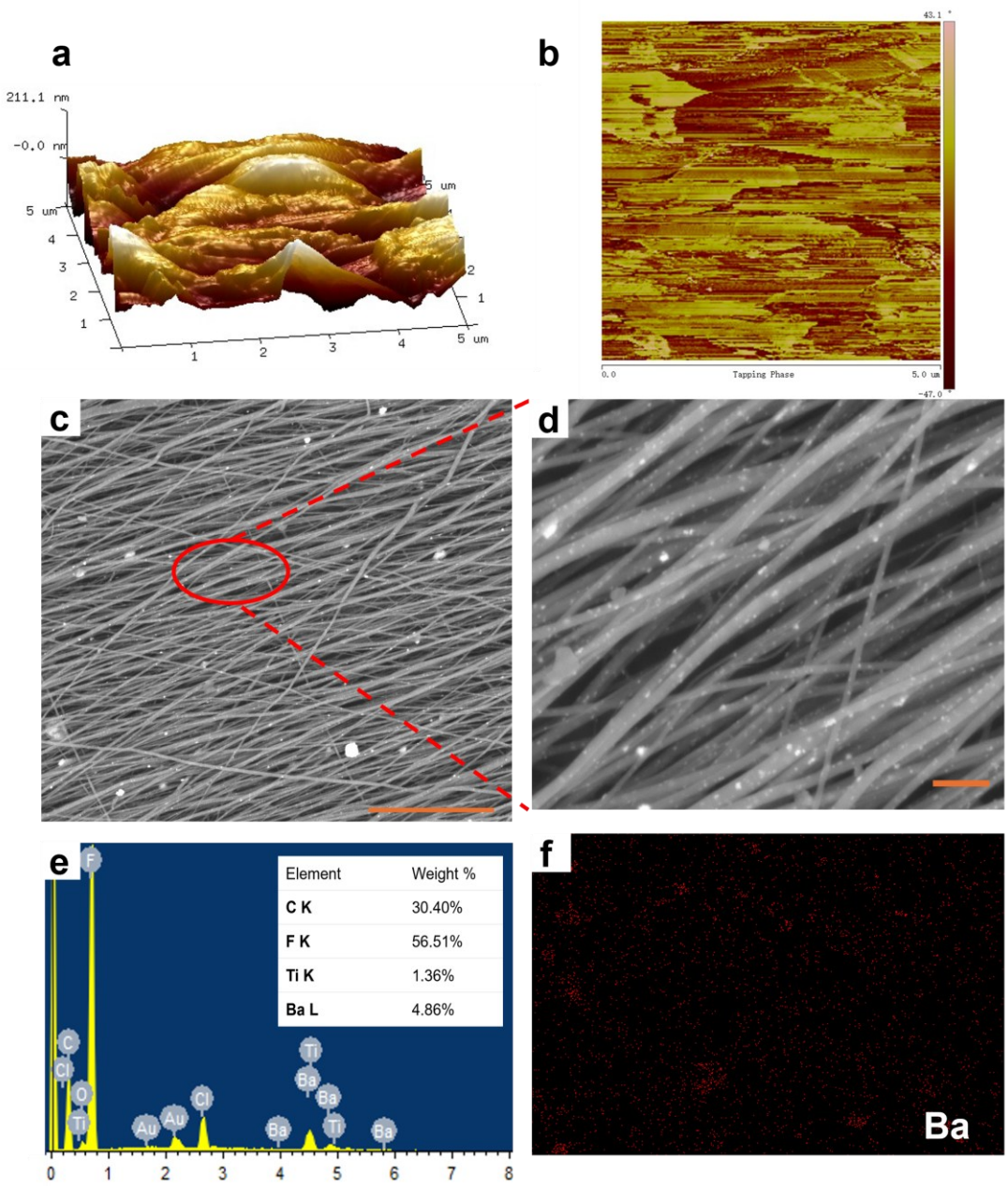

Fig. 3.6 3D height (a) and tapping phase (b) of the PVDF-TER/BTO nanofibers characterized by atomic force microscopy (tapping， 5 μm × 5 μm). (c) The SEM image of the PVDF-TER/16%BTO membrane demonstrates the well-alignment of the nanofibers (Scalebar: 50 μm). (d) The enlarged image of nanofibers (Scalebar: 10 μm). The BTO (<99nm) nanoparticles are fully dispersed within the fibers. (e) and (f) are the EDS element analysis and related mapping of Barium.

As previously mentioned, the bulk density and porosity of electrospun films are critical factors influencing the sensitivity of sensing film units. As shown in **Table 3.2**, we tested the bulk density and porosity of films with either aligned or random fiber orientations for different material compositions. At the same thickness, the bulk density of electrospun films ranges from 0.38 to 0.55 g/cm^3. The relatively low density improves the acoustic response for electrospun films, as their acoustic impedance ($Z=\rho v$) is closer to that of air, enabling effective impedance matching for incident sound waves and thereby greatly enhancing the electromechanical coupling efficiency (For comparison, the acoustic impedance of a dense PVDF film is approximately 2.5–3.5 MRayl). In addition, the lower density results in sensing unit with low mass at the same thickness, allowing it to respond more effectively to subtle acoustic pressures (~10^{-7} atm) by generating larger strains, making it well-suited for acoustic sensing applications. Compared with randomly oriented nanofibers, the aligned nanofiber films exhibit slightly lower porosity. This is attributed to the high-speed collector in the directional electric field, which stretches and aligns the fibers during deposition, leading to in situ packing. The slightly reduced porosity improves the tensile strength and fatigue life of the fibers, while also minimizing inter-fiber sliding friction and thereby reducing signal drift.

Table 3.2 The bulk density of the materials and electrospun membranes and corresponding calculated porosity of different samples.

Materials	Materials Density (g/cm^3)	Film Density (g/cm^3)	Porosity
PVDF-TER_Random	1.8	0.38±0.085	78.53%
PVDF-TER_Align	/	0.432±0.107	74.7%
PVDF-TER/BTO_Align	/	0.456±0.091	71.54%
BTO	6.08	/	/

The fiber alignment and BTO doping were found to influence the mechanical properties of the electrospun films. Tensile tests were performed to measure the tensile strength of films with different fiber orientations, and the corresponding Young's modulus values were calculated (**Fig. 3.7a** and **b**). Compared with the randomly oriented films, the aligned films exhibit higher strain and tensile strength. The incorporation of rigid BTO particles into the flexible polymer matrix increased the elastic modulus of the fibers but compromised their ultimate strain, which is related to the nanoscale interfacial layers discussed above. For the pure PVDF-TER electrospun film, the elastic modulus along the fiber alignment direction was 310 ± 56.9 MPa and increased to 364.6 ± 48.2 MPa after the doping of 16 wt% BTO nanoparticles. In contrast, the modulus perpendicular to the alignment direction was 44.5 ± 21.3 MPa. The orders-of-magnitude difference in elastic modulus between the two directions further confirms the anisotropic nature of the film. Under the same thickness conditions, commercial PVDF films exhibit a Young's modulus of approximately 2.2 GPa, which is six times higher than that of electrospun films, contributing greater deformation under minimal pressure of the electrospun films. Furthermore, in subsequent encapsulation applications, electrospun mats show better mechanical compatibility with elastomers, effectively reducing stress

concentration making it suitble for prolonged use.

In this chapter, the dielectric properties of these highly porous piezoelectric fiber membranes were systematically evaluated. As shown in **Fig. 3.7c**, the dielectric constant of the fiber membrane remains relatively low across the frequency range of 10^2 to 10^6 Hz, exhibiting a gradual decline with increasing frequency. This behavior is attributed to the porous microstructure formed during electrospinning, where the presence of air (dielectric constant ≈ 1) effectively reduces the overall dielectric constant (ε) of the composite system. Consequently, the piezoelectric voltage constant (g_{33}) is significantly enhanced without compromising the piezoelectric coefficient (d_{33}). Compared to dense films, the porous piezoelectric fiber membrane exhibits superior sensitivity and signal-to-noise ratio in detecting low-pressure, high-frequency biosignals such as heart sounds and bowel sounds. These results validate the strategy of tuning dielectric constant via structural engineering to improve piezoelectric output performance for wearable acoustic sensing applications.

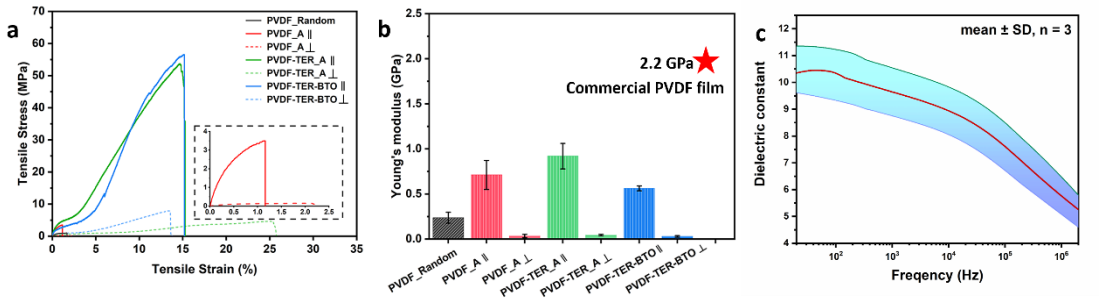

Fig. 3.7 (a) The strain-stress curve of the various electrospun nanofibers from different tensile directions (parallel to and perpendicular to the fiber), and (b) the corresponding calculated Young's modulus. (Compared with the dense commercial PVDF film under

same thickness: 2.2 GPa.) (c) The dielectric constant of the porous PVDF-TER-BTO electrospun membranes.

3.3.3 Piezoelectric properties and mechano-electric output

For subsequent testing of the piezoelectric performance of the electrospun films, electrodes and lead wires were integrated onto the films, followed by encapsulation to prevent interference from humidity and other environmental factors during measurements. As shown in **Fig. 3.8**, a sandwich-structured electrode was formed by depositing a 100 nm copper (Cu) layer on both the top and bottom surfaces of the film via magnetron sputtering (PVD). The electrodes were connected to metallic lead wires and encapsulated using a thermoplastic material molded to shape (fiber area: 500 × 5 mm along the fiber orientation direction, thickness: 70 μm). The encapsulated fiber exhibits excellent flexibility and conformability, enabling reliable performance in subsequent tests.

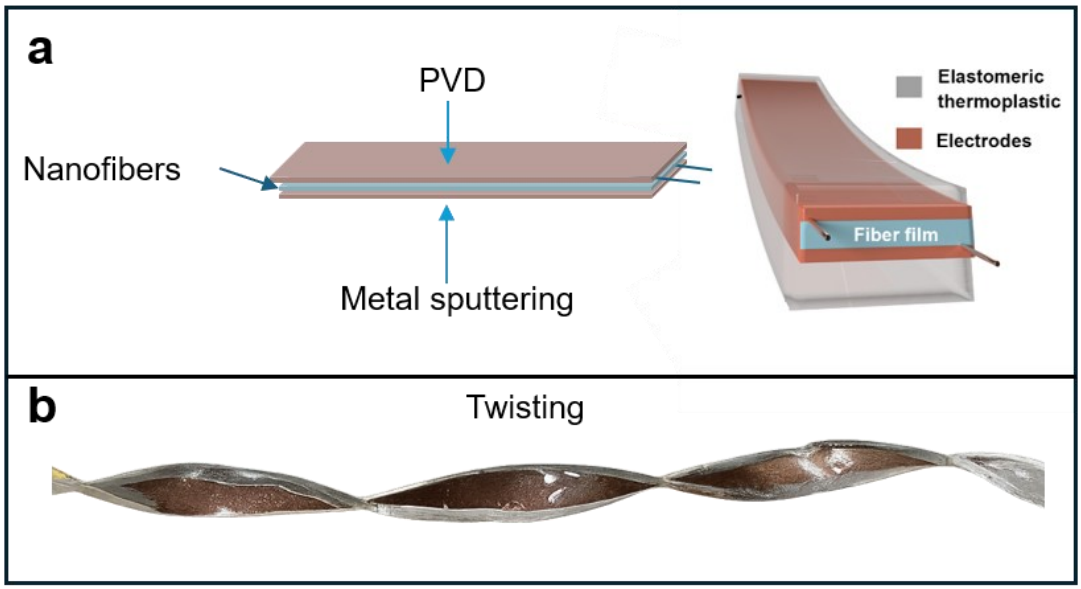

Fig. 3.8 Schematic illustration (a) and photographs (b) of fiber electrode fabrication and encapsulation for the PVDF-TER/BTO electrospun film. (The twisted fiber in the optical picture shows its high flexibility.)

Using the method described in **Section 3.2.4**, the transient charge transfer under different tensile strains was measured, enabling calculation of the d_{31} parameter for the corresponding tensile load area (**Fig. 3.9a–c**). By fitting the slope of the data, the d_{31} values were determined for both low-stress and high-stress regimes. The results show that, for nanofibers, the d_{31} is approximately 26.74 pC N^{-1} in the 0–2.5 MPa stress range, while in the 2.5–5 MPa range it increases significantly to about 45.5 pC N^{-1}. This nonlinear behavior is primarily attributed to the inconsistent responses of certain ferroelectric domains under low and high stress. When the applied stress exceeds a critical threshold, polar crystalline regions undergo rearrangement, which in turn activates previously inactive domains, thereby enhancing the piezoelectric response. To further validate the accuracy of the indirect method for calculating the d_{31} parameter, we compared the results for a commercial PVDF film tested under the same dimensions, surface area, and encapsulation conditions. The measured d_{31} value was 27.6 pC N^{-1}, which is within 5% of the manufacturer's specified value of 29 pC N^{-1}. By comparing our results with those reported in studies that employed similar calculation methods (**Fig. 3.9d**), it can be concluded that our electrospun films exhibit superior d_{31} values compared with commercial films. In the high-stress regime, the d_{31} of our nanofiber also exceeds that of thermal drawn P(VDF-TrFE)/$BaTiO_3$ composite fibers with additional electric poling.

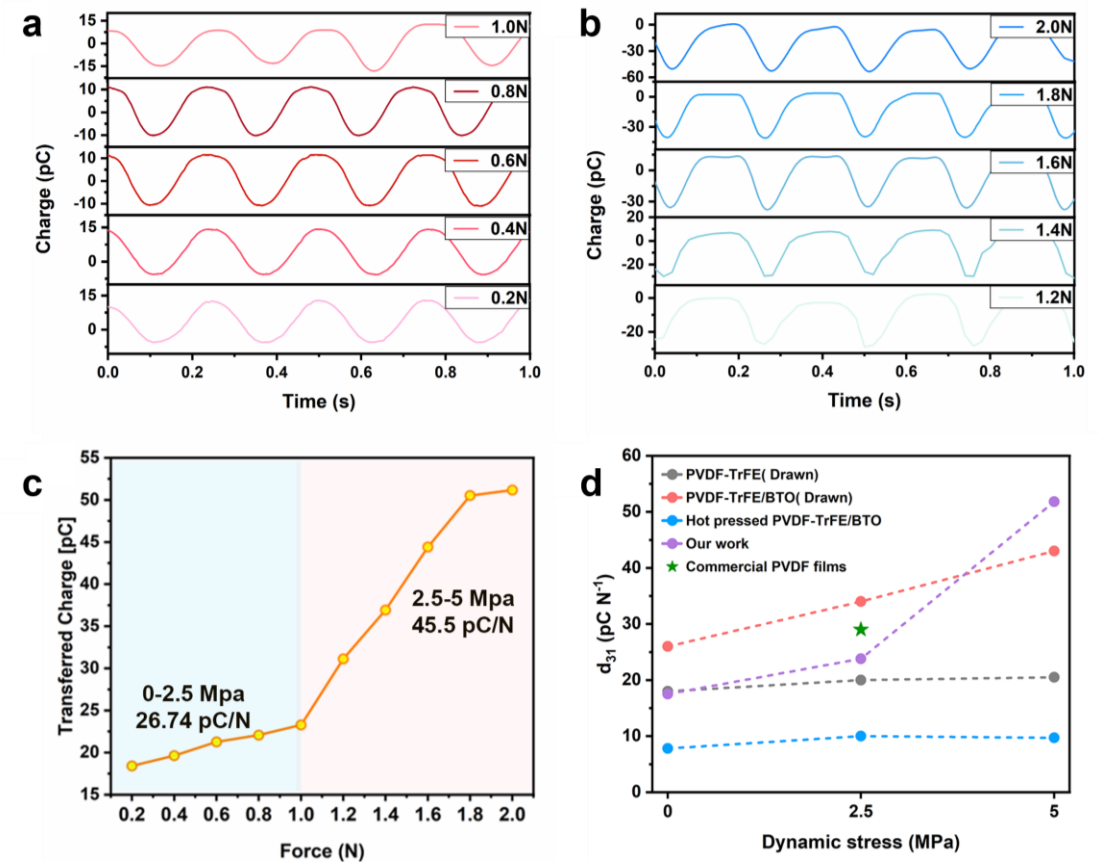

Fig. 3.9 The charge transfer versus the different tensile stress. (a) Low tensile stress region of 0–1.0 N. (b) High tensile stress region of 1.2–2.0 N. (c) Result of transferred charges versus applied tensile stress with the calculated dynamic sensitivity variations under low (blue) and high (pink) tensile stress region. (d) The comparison of d_{31} value of PVDF-TER/BTO nanofibers with other works and commercial PVDF films.

In addition to the d_{31} parameter, the d_{33} parameter also reflects the piezoelectric constant for the electrospun membrane. Here, piezoelectric force microscopy (PFM) and a quasi-static instrument were employed to measure single fibers and the entire bulk film, respectively, for cross-validation. The results from the quasi-static method show a d_{33} value of –30.9 pC $^{-1}$, as shown in **Fig. 3.10a**. In addition, the PFM measurements of single fiber demonstrate the ferroelectric characteristics of the material. **Fig. 3.10b**

shows the amplitude butterfly loop of a single composite fiber under a bias voltage of ±30 V. The maximum amplitude is observed at ±24 V, corresponding to the coercive fields. Under applied bias voltage, the phase image (**Fig. 3.10c**) reveals a 180° reversal of the ferroelectric domains. The d_{33} value of a single fiber, calculated from the PFM measurements, is 67.5 pC N^{-1}. Such discrepancies are common in piezoelectric materials and can be attributed to factors such as mechanical coupling between fibers and variations in stress transfer efficiency in quasi-static tests, arising from the weak adhesion between fibers and the substrate. Therefore, subsequent measurements in this work primarily rely on the macroscopic test result. To better evaluate the piezoelectric performance of our electrospun films, we compared the piezoelectric coefficients reported in recent similar studies with those obtained in this work. The results are summarized in **Table 3.3**.

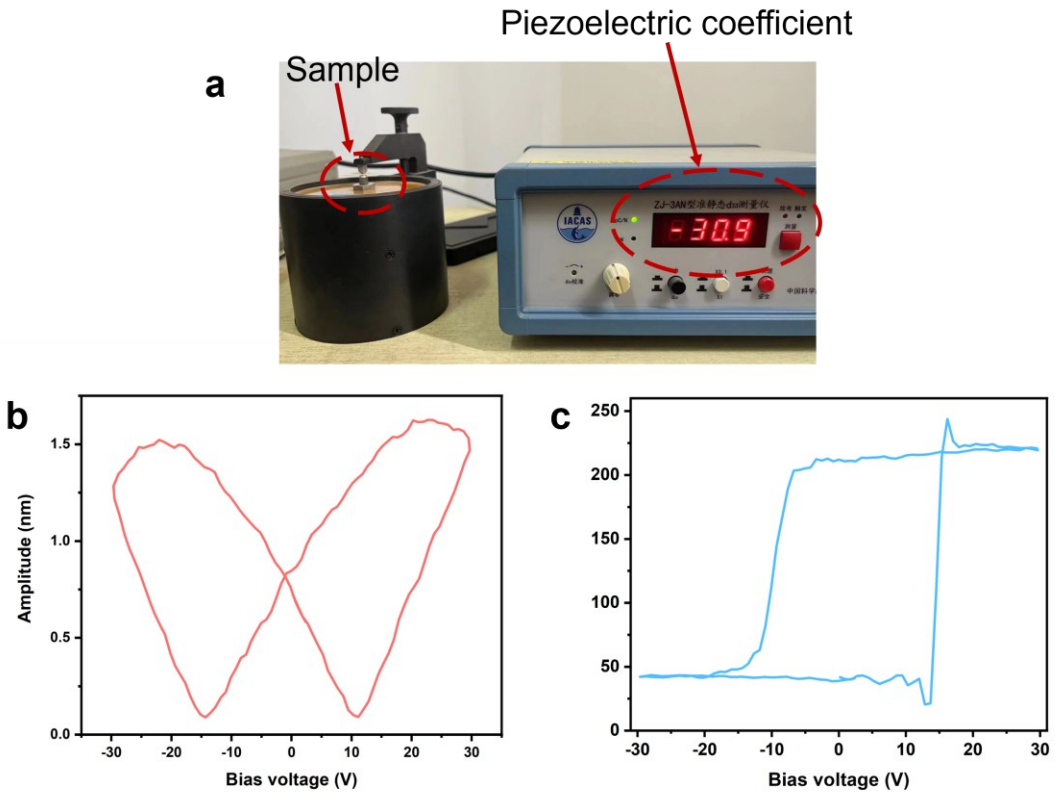

Fig. 3.10 (a) The optical image for measuring the piezoelectric coefficient. (b) PFM butterfly amplitude loop and (c) PFM phase of the nanofibers under a direct current (DC) bias ± 30V.

Table 3.3 The comparison of the piezoelectric coefficients in different works.

Piezoelectric Materials	Structure	Processing techniques	Piezoelectric coefficient, d_{33}/d_{31}	Measurement methods	Ref.
PVDF-TrFE/BTO	Film	3D printing/ electric poling	–20 ±0.6 pC/N (d_{33}, composites)	Conventional quasistatic method	[189]
PVDF-TrFE/BTO	Belt-like Fibres	Thermal drawing	46 pC/N (d_{31}, composites)	Indirect tensile test method	[4]
PVDF-TrFE/BTO	Film	Spin coating and poling	–23 pC/N (d_{33}, composites)	Conventional quasistatic method	[185]
PVDF-TrFE/BTO	Fibrous film	Electrospinning/ electrospray	32.72 pC/N (d_{33}, composites)	Conventional quasistatic method	[190]
PVDF-TrFE/BTO	Film	Solvent casting and poling	20 pC/N (d_{33}, composites)	Conventional quasistatic method	[191]
PVDF-TrFE/BTO	Film	Spin coating	146±7.31 pC/N (d_{33},composites)	PFM	[192]
PVDF-TrFE/BTO	Nanofiber membrane	Electrospinning	21.2 pC/N (d_{33},composites)	PFM	[193]
PVDF-TrFE	Film	Imprinting and electric poling	18–24 pm/V (d_{33})	PFM	[194]
PVDF-TrFE	Film	Spin coating	1.195 pm/V (d_{33})	PFM	[195]
PVDF-TrFE-CFE	Film	Solvent casting and poling	49.6 pC/N (d_{33})	Conventional quasistatic method	[196]
PVDF-TrFE-CFE /BTO	Film	Solvent casting and poling	43 ± 2 pm/V (d_{33})	PFM	[197]

PVDF-TrFE-CFE/BTO	Nanofibre	Electrospinning	67.5 pC/N d_{33} 30.9 pC/N d_{33} 45.5 pC/N d_{31}	PFM, Conventional quasistatic method, Indirect tensile test method	This work

Finally, the anisotropic films were tested to evaluate their linear sensitivity and to investigate the effect of different stress orientations on the electromechanical output characteristics of the fibers. The electrospun piezoelectric film demonstrates force-sensitive and directionally-dependent electromechanical behavior. Under compressive loading, the voltage output increases with force up to ~6 N, beyond which saturation effects limit further enhancement (**Fig. 3.11a–b**). Under saturated polar loading, i.e., below 6 N, linear fitting of the output (R^2=0.96) yields a linear sensitivity of 262 mV N^{-1}.The voltage response also varies significantly with fiber alignment angle, with maximum output observed when the force is applied along the fiber axis (90°). Furthermore, bending tests reveal a curvature-dependent output, with larger bending radii (lower curvature) leading to higher voltage signals, especially when fibers are aligned orthogonal to the bending direction. These findings highlight the anisotropic nature of the electrospun structure and its tunable sensitivity for wearable and directional sensing applications. The high voltage output under in-plane strain along the fiber direction lays the foundation for the directional sensitivity of subsequent acoustic sensor devices.

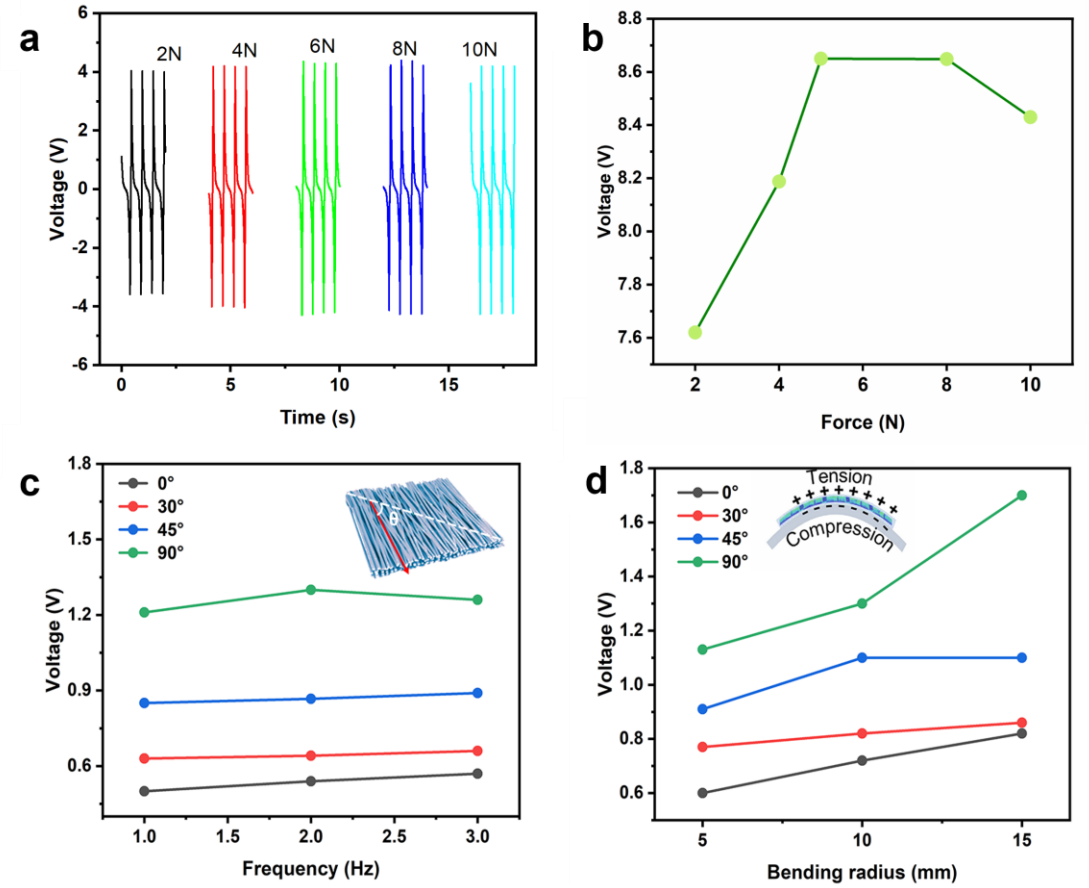

Fig. 3.11 (a) Periodic voltage output under different loads. (b) The variation of peak voltage with the applied force. (c) Voltage outputs at various frequencies (1–3 Hz) at a constant bending radius (10 mm) with varying fiber orientation angles (0°, 30°, 45°, and 90°) relative to stress direction. (d) Voltage outputs under different bending radii (5–15 mm) at various fiber orientations.

3.4. Conclusions

In this work, we developed a flexible, low-density, and highly crystalline anisotropic piezoelectric electrospun film. Using PVDF-TER as a flexible matrix and embedding BTO nanoparticles, we fabricated highly aligned nanofibers. The synergistic effects of BTO-induced heterogeneous nucleation and interfacial polarization enhanced the

polarity of the piezoelectric film, resulting in an all-trans phase (*TTTT'*) content of approximately 92%. The piezoelectric constant d_{33} reached –30.9 pC N^{-1}, while secondary stretching during electrospinning enabled the d_{31} of the nanofiber film to reach 45.5 pC N^{-1}. The high porosity of the film moderated its apparent dielectric constant, allowing it to maintain a high d_{33} value while achieving an elevated g_{33}, thereby ensuring efficient electromechanical coupling. Under low loading, the piezoelectric film exhibited a high sensitivity within the linear regime, and the high voltage output generated under in-plane strain along the fiber direction established the basis for directional sensitivity in subsequent acoustic sensor devices. Among PVDF-based piezoelectric films, our design maintains a comparatively high piezoelectric coefficient and demonstrates strong potential as a piezoelectric sensing unit for future electroacoustic coupling applications.

CHAPTER 4 DESIGN AND ASSEMBLY FOR LOW-FREQUENCY RESONANCE-DRIVEN SHAPE-ADAPTIVE ACOUSTIC SENSOR

4.1. Introduction

With the growing demand for wearable technologies in biomedical and health monitoring applications,[198, 199] flexible and highly sensitive acoustic sensors have gained increasing attention for detecting physiological signals.[200-203] Compared to conventional rigid electronic stethoscopes, flexible acoustic devices offer better conformability to body surfaces and improved wearing comfort, making them more suitable for long-term and dynamic monitoring scenarios.[204-206] Recent research efforts have predominantly focused on patch-based flexible acoustic sensors.[207-210] However, achieving high signal stability under body movement and suppressing interference from ambient noise remain key challenges. These issues significantly limit the signal fidelity and anti-interference capability, especially in comparison to rigid counterparts.

Another major technical bottleneck lies in the reliable integration of conductive electrodes onto flexible sensing layers. For dense-film-based sensors, metal electrodes are commonly deposited using physical vapor deposition (PVD) techniques.[211] While when applied to electrospun membranes, these rigid films tend to suffer from cracking or delamination due to mechanical mismatch with the soft substrate and inter-fiber slippage during repeated deformation. This leads to disruption of the conductive pathway and degrades long-term device reliability. Alternative strategies such as

screen-printing stretchable conductive inks (e.g., silver paste or carbon nanotube) or fabricating metal nanofiber electrodes via electrospinning have also been explored.[212-218] However, these methods often struggle to achieve nanoscale and may alter the mechanical modulus of the sensing membrane, thus compromising its acoustic sensitivity and eliminating the intrinsic advantages of electrospun structures.

In this study, we adopt an electro-spraying method to deposit silver nanowires (AgNWs) onto electrospun piezoelectric films, forming a flexible and robust conductive network. The resulting electrode maintains excellent conductivity and interfacial adhesion and exhibits outstanding mechanical resilience under repeated bending cycles. In contrast, copper films deposited via sputtering display rapid electrical degradation under similar stress conditions, primarily due to fracture formation arising from rigidity and localized stress concentration. Additionally, the slippage between fibrous structures further contributes to electrode failure.

Building upon this flexible electrode design, we developed a multilayer flexible acoustic sensor with both structural support and surface adaptability. The sensor conforms well to curved body areas and maintains signal output under movement. A conical back cavity, designed using COMSOL simulations, was incorporated to enhance sound pressure concentration and mechanical vibration, leading to amplified electrical responses. This chapter presents the selection of materials, fabrication processes, and performance evaluation of a flexible acoustic sensor integrated with AgNW electrodes. The results highlight its potential for high-fidelity physiological

signal detection in next-generation wearable health monitoring systems.

4.2. Experimental section

4.2.1 Materials

The silver nanowires (AgNWs) solution (10mg/ml, 30–60 nm diameter, 10–20 μm length) was purchased from OE. CHEMICAL, CHINA. Triton™ X-100 (CAS No. 9002-93-1, $C_{34}H_{62}O_{11}$, M_W = 647, purity >98%, density 1.057–1.065 g·mL^{-1} at 20 °C) was purchased from Phygene. The 3D printing was performed using Deposition Modeling technology (FDM), with thermoplastic polyurethane (TPU, Shore hardness 90) filament. The infill density was set to 100% to ensure structural compactness. Kafuter (K-3725H) UV-curable adhesive is used to bond and encapsulate equipment components. The Shore D hardness of this resin is approximately 69 (GB/T 531–1999), and its elongation at break is about 120%, ensuring both flexibility and structural integrity. This adhesive is a low-viscosity acrylic resin (viscosity < 2600±500) that can be rapidly cured under UV light to form mechanically strong seal.

4.2.2 Fabrication of the electrodes on electrospun film

Two approaches were employed to fabricate electrodes on the electrospun films. As shown in **Fig. 4.1**, the left diagram illustrates the first method, in which silver nanowire (AgNW) electrodes were deposited onto the surface of the electrospun films via electrostatic spraying. An AgNW dispersion (10 mg·mL^{-1}, ethanol: water = 7:3) was prepared by mixing with Triton™ X-100 at concentrations of 0.05, 0.1, 0.15, and 0.2

wt%. The mixtures were magnetically stirred for 20 min to ensure homogeneous distribution of the surfactant. Subsequently, the well-dispersed AgNW suspensions were atomized under an applied voltage of 20 kV and uniformly sprayed onto the surface of the electrospun films. The deposition was controlled to achieve a sheet resistance of approximately 3 Ω sq^{-1}, ensuring high conductivity while preserving the flexibility and porosity of the nanofiber membrane. The thickness is controlled to about <200nm. Subsequently, the AgNW electrodes deposited on the electrospun membrane were annealed on a hot plate at 100 °C for 1 h. This process promotes thermal welding between adjacent silver nanowires, thereby effectively reducing the contact resistance and enhancing the stability of the conductive network. After annealing, the overall electrical performance of the AgNW network was significantly improved, ensuring reliable conductivity during subsequent device assembly and under mechanical deformation.

For physical vapor deposition (PVD), magnetron sputtering (Surrey Nanosystems Gamma 1000C®, Newhaven, UK) was employed to deposit a copper electrode onto both sides of the electrospun films, yielding a sandwich-like configuration (**Fig. 4.1 right**). A copper target (purity ≥ 99.99%) was sputtered under an argon atmosphere of 0.5 Pa at a power of 100 W. The sputtering time was adjusted to achieve a final film thickness of approximately 100 nm on each surface.

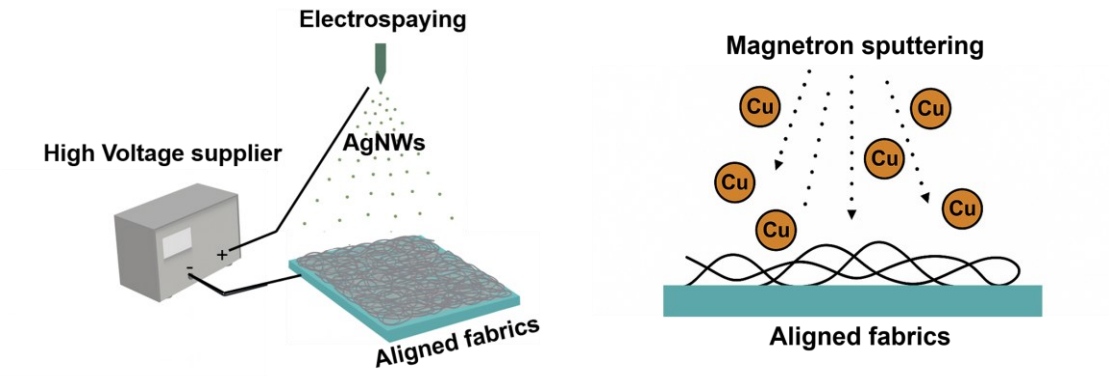

Fig. 4.1 Electrodes fabrication schematic diagram: (Left) silver nanowires (AgNWs) are deposited on electrospun film via electrospraying; (right) copper atoms are sputtered by magnetron sputtering on electrospun film.

4.2.3 Shape-adaptive acoustic sensors assembly procedure

The assembly of the piezoelectric acoustic device was carried out via two parallel routes: internal integration of the piezoelectric sensing element and external encapsulation of the housing.

Internal assembly

- Electrospun piezoelectric films (Thickness 70 μm) with electrodes were precisely cut into the required geometry using an ultrasonic cutter.
- A vibration diaphragm was cut to match the device dimensions (diameter 26mm).
- The piezoelectric film was thermally laminated onto the diaphragm using ethylene-vinyl acetate (EVA) hot-melt adhesive web (thickness: 40 μm, diameter: 14mm) under controlled hot-pressing conditions (80 °C).
- To improve acoustic responsiveness, a small tensile pre-strain was applied to the

diaphragm by mounting it onto an embroidery hoop fixture.

External assembly

- A circular housing was fabricated by 3D printing TPU (Shore hardness 90A, 100% infill). The top and bottom shells were aligned and pre-assembled.
- To suppress electromagnetic interference, the inner surface of the housing was uniformly coated with a thin silver (Ag) shielding layer.
- The diaphragm–film unit was fixed onto the bottom shell using UV-curable adhesive (Kafuter (K-3725H) UV glue), ensuring airtight encapsulation and mechanical stability.
- Excess diaphragm material protruding outside the housing was trimmed.
- The top shell was bonded and sealed by UV curing, completing the device encapsulation.
- Finally, to achieve acoustic impedance matching and effectively amplify the subtle vibration signals from the skin surface, a silicone layer (thickness of approximately 100 μm) was incorporated on the skin-contacting side of the lower housing.

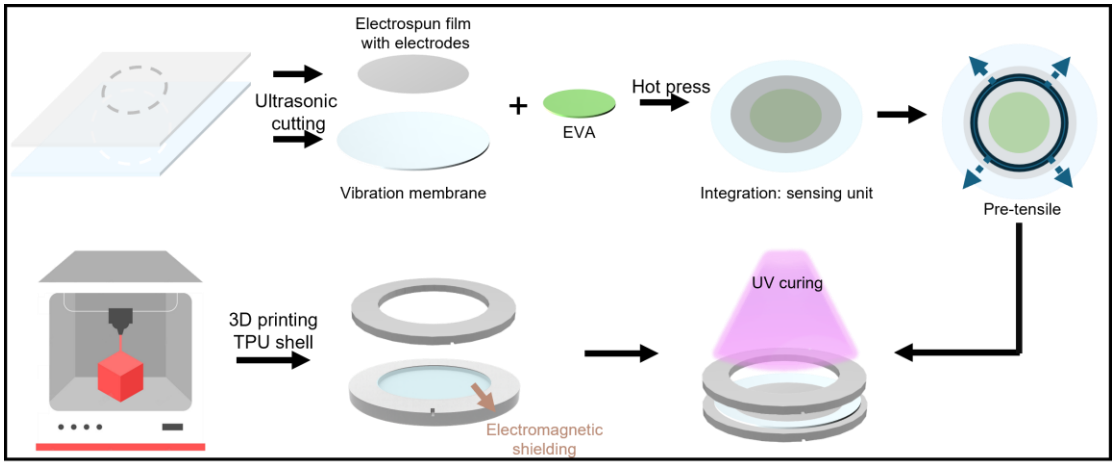

Fig. 4.2 Fabrication process flow diagram of the device assembly.

4.2.4 Characterization and Measurements

Electrode measurements

The surface morphologies of AgNW electrodes prepared with varying concentrations of Triton X-100 were examined using an optical microscope (Laica 130), with particular attention to the occurrence of the coffee-ring effect. Scanning electron microscopy (SEM, VEGA3) was employed to evaluate fracture features of the electrodes after bending deformation. For electro-mechanical testing, current-voltage characteristics under different bending curvatures were recorded using a Keithley 2400 source meter, which provided a stable bias voltage. Simultaneously, controlled bending was applied and maintained using an Instron 5944 system. The cyclic bending durability was further assessed by continuous monitoring with a Keithley 2010 multimeter, in combination with a custom-built stepper-motor platform.

Acoustic response testing

To evaluate the acoustic response of the sensors and guide performance optimization, an acoustic testing chamber was constructed, as illustrated in **Fig. 4.3**. The sensor was secured using a magnetic base clamp to enhance structural stability and suppress the transmission of external mechanical vibrations, while a loudspeaker (Logitech, LS21) was positioned directly beneath the sensor. A sound level meter (DELIXI, DLY-2202), also mounted on a magnetic fixture and aligned with the sensor at the same horizontal level, was employed to ensure accurate calibration of the sound pressure level (SPL).

The emission and acquisition of acoustic signals were realized through an electrometer (KEITHLEY 6517B) and a data acquisition (DAQ) system. The computer controlled the loudspeaker to generate acoustic signals, which were transduced into electrical signals by the sensor. These signals were captured by a high-impedance electrometer, collected via an NI card (NI-USB-6536), and finally transferred to the computer for storage.

The interior of the chamber was lined with acoustic foam to effectively absorb sound energy, thereby reducing wave reflections inside the enclosure and approximating a free-field environment. In addition, the foam helped suppress ambient noise interference during testing, ensuring consistency and repeatability in sensor calibration. To further minimize external disturbances, the exterior of the chamber was covered with a grounded copper mesh, which acted as a quasi-Faraday cage to shield against electromagnetic interference.

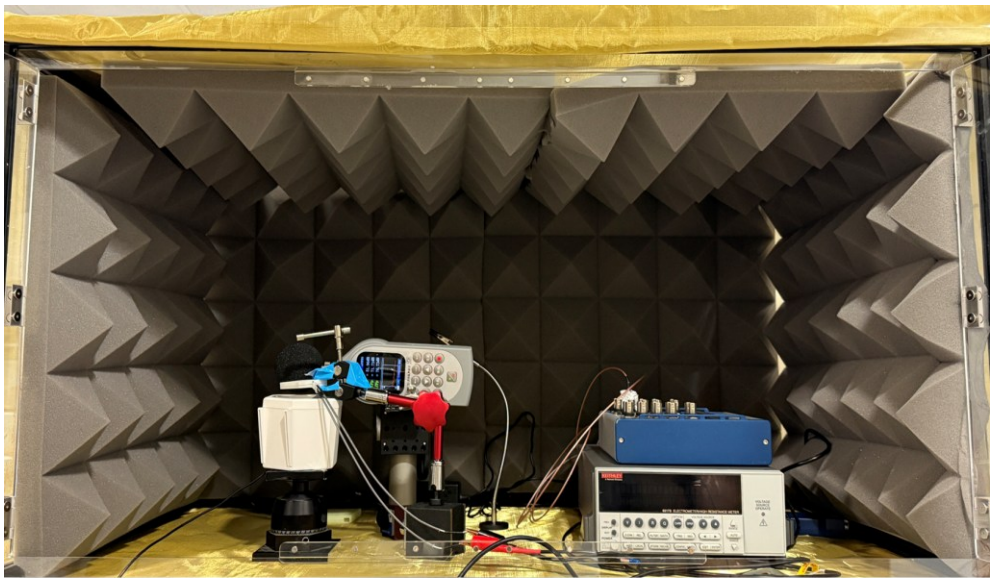

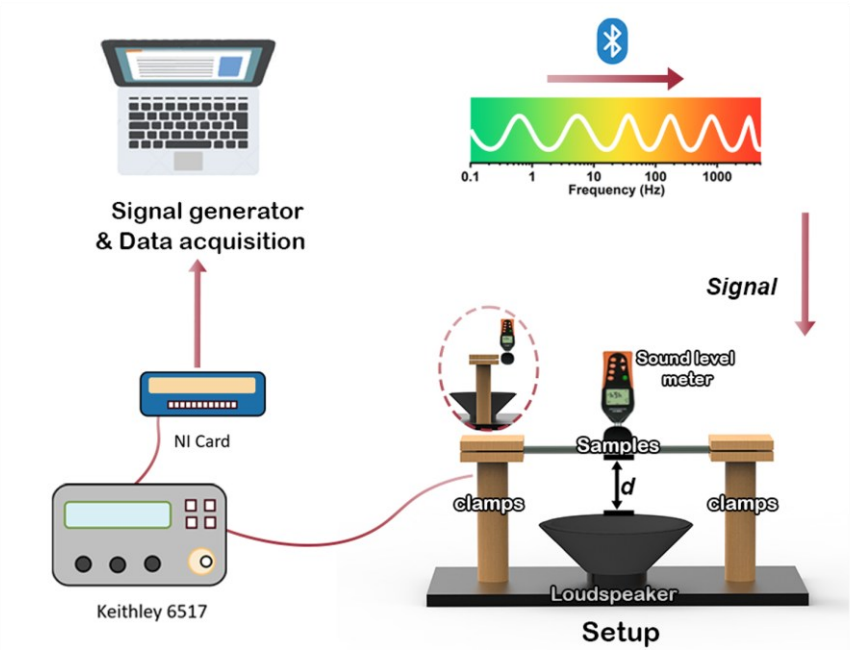

Fig. 4.3 The full-scale acoustic chamber image for acoustic response testing (upper). Sound insulation from noise background: sound-absorbing cotton (thickness: 8 cm), interference shielding with copper mesh grounding. Schematic illustration of the real-time acquisition system for acoustic testing (bottom).

Acoustic frequency response analysis

The frequency response and the sensitivity calibration are essential steps in evaluating

acoustic sensor performance. To this end, sweep frequency was employed to apply a continuous sinusoidal sweep excitation within the target frequency range of 20–1200 Hz, thereby identifying the sensor's resonance regions and effective operating bandwidth. Subsequently, the acquired time-domain signals were processed using Fast Fourier Transform (FFT) to obtain the corresponding frequency-domain curves. By analyzing the amplitude-frequency characteristics, the sensor's response variation across frequencies can be determined, including primary resonance peaks, bandwidth range, and high-frequency attenuation.

In addition to frequency response, the sensitivity of the sensor is another critical performance metric. Sensitivity is defined as the ratio of the output voltage to the input sound pressure, expressed as[146]:

$$S = \frac{V}{P} = \frac{V}{P_0 \cdot 10^{L_p/20}}$$

where *Lp* is the sound pressure level (dB), $P_0 = 2 \times 10^{-5}$ Pa: Commonly used sound pressure in air (hearing threshold of the human ear).

COMSOL Multiphysics model

Geometry: A circular diaphragm-cavity-housing assembly was modeled. The diaphragm comprises a PI (Kapton) substrate of thickness 25 μm and diameter·26 mm, carrying a electrospun piezoelectric film of thickness 70 μm and diameter 22 mm. The two layers are bonded within a central EVA hot-melt film (40 μm thick, diameter 14 mm); outside this area the interfaces are left unbonded to preserve peripheral compliance. The diaphragm is effectively clamped on a circular rim at radius 12 mm

(Fixed Constraint), and no pretension is applied.

The back cavity is a TPU annulus with a tapered inner bore: the inner diameter is 26 mm at the top (diaphragm side) and 34 mm at the bottom, with a depth of 4 mm. Top housing integrated with single vent of 3 mm (diameter) connects the cavity to the exterior.

Boundary and excitation conditions: The exterior acoustics is modeled in a hexahedral domain. One planar face carries an Incident Pressure Field representing a spherical wave emitted by a virtual monopole positioned just outside that face and aligned with its normal. The source amplitude is calibrated so that the incident sound pressure at the diaphragm center is exactly 1 Pa at every frequency. The remaining five faces are terminated by perfectly matched layers (PMLs); PML thickness is set to roughly 0.4–0.6 of the minimum wavelengths, and the device is placed at least ~0.3 of that wavelength away from the inner PML boundary to avoid spurious reflections.

Piezoelectric stress-strain relationship and anisotropic material modeling

To accurately describe the electromechanical coupling behavior of our electrospun anisotropic piezoelectric film, it is essential to define the appropriate material coefficient matrices in the COMSOL simulation environment. Specifically, the compliance matrix [K_{ij}][219, 220], which describes the material's strain response to mechanical stress, is implemented as shown below. Its inverse, the stiffness matrix [C_{ij}], represents the stiffness of the material and is derived accordingly.

In addition, we have summarized the key mechanical and piezoelectric properties of the materials used in this study, as presented in **Table 4.1**. These parameters serve as essential inputs for finite element simulations and ensure accurate prediction of the sensor's mechanical-electrical behavior under dynamic excitation.

$$[K_{ij}] = \begin{bmatrix} \frac{1}{Y_z} & -\frac{\mu_{xz}}{Y_x} & -\frac{\mu_{xz}}{Y_x} & 0 & 0 & 0 \\ -\frac{\mu_{xy}}{Y_x} & \frac{1}{Y_x} & -\frac{\mu_{xy}}{Y_x} & 0 & 0 & 0 \\ -\frac{\mu_{xz}}{Y_x} & -\frac{\mu_{xy}}{Y_x} & \frac{1}{Y_x} & 0 & 0 & 0 \\ 0 & 0 & 0 & \frac{2(1+\mu_{xy})}{Y_x} & 0 & 0 \\ 0 & 0 & 0 & 0 & \frac{1}{G_{zx}} & 0 \\ 0 & 0 & 0 & 0 & 0 & \frac{1}{G_{zx}} \end{bmatrix},$$

$$= \begin{bmatrix} 3.333 & -1.818 & -1.818 & 0 & 0 & 0 \\ -8.864 & 22.727 & -8.864 & 0 & 0 & 0 \\ -1.818 & -8.864 & 22.727 & 0 & 0 & 0 \\ 0 & 0 & 0 & 63.182 & 0 & 0 \\ 0 & 0 & 0 & 0 & 49.09 & 0 \\ 0 & 0 & 0 & 0 & 0 & 49.09 \end{bmatrix} \times 10^{-9}$$

Table 4.1 The input mechanical parameters of the anisotropic piezoelectric layer.

Young's modulus (longitudinal)	Y_z	364.6 ± 48.2 MPa
Young's modulus (transverse)	$Y_x = Y_y$	44.5 ± 21.3 MPa
Poisson's ratio (xz plane)	μ_{xz}	0.08
Poisson's ratio (xy plane)	μ_{xy}	0.39
Shear modulus (zx plane)	G_{zx}	20.37 MPa
Piezoelectric constant	d_{33}	–30.9 pC/N
Piezoelectric constant	d_{31}	25.6 pC/N

Density	ρ_c	0.42g/cm^3
Dielectric constant	ε_r	12(1kHz)

4.3. Results and discussion

4.3.1 Flexible electrodes characterizations and optimization

For flexible electrospun films used as electromechanical sensing units, it is essential to construct surface electrodes with good flexibility and electrical conductivity. In this study, a method using silver nanowires (AgNWs) was investigated to prepare flexible electrodes. The electrodes were deposited on the fiber surface by electrospray coating, and the deposition quality was adjusted by controlling the spraying and dispersion parameters, as shown in **Fig. 4.1**. At the same time, copper electrodes were prepared on the fiber films using physical vapor deposition (PVD), which is commonly used in previous studies, to serve as a rigid comparison. The electrical stability and structural integrity of both types of electrodes were evaluated under bending conditions to verify the reliability of the flexible fiber-based electrodes.

To evaluate the effect of Triton X-100 concentration on the spreading behavior of AgNWs ink on the hydrophobic electrospun film, we measured the contact angles (CA) of AgNWs ink mixtures with varying surfactant concentrations (0–0.1 wt %) on the surface of the electrospun piezoelectric membrane, as shown in **Fig. 4.4a**–**b**. The contact angle decreased markedly from 131° to 34° with increasing surfactant content, indicating enhanced wettability and improved uniformity of AgNWs distribution. As illustrated in **Fig. 4.4c**, when the Triton X-100 concentration was 0.05%, the droplet

flattened rapidly within 2 seconds, reflecting the fast dynamic wetting behavior facilitated by the presence of the surfactant.

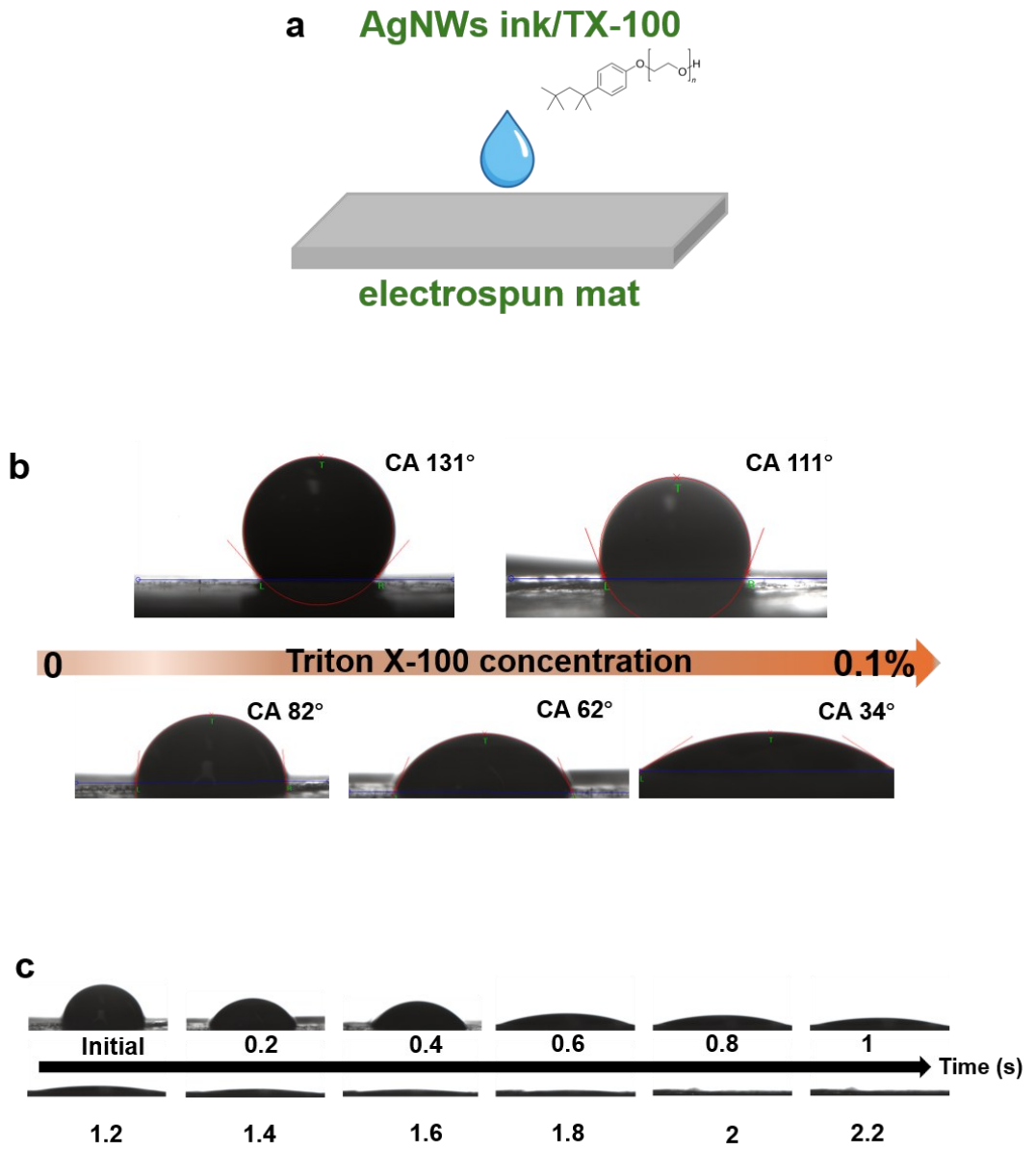

Fig. 4.4 Effect of Triton X-100 concentration on the spreading behavior of AgNW ink on electrospun membranes. (a) Schematic illustration of the AgNWs ink formulation containing different concentrations of Triton X-100 applied onto an electrospun mat. (b) Contact angle (CA) images of AgNWs droplets with increasing Triton X-100 concentrations (0–0.1 wt%). (c) Time-resolved droplet profiles of 0.05 wt% TX-100-

modified AgNW ink during spreading.

The influence of surfactants on the electrode performance primarily stems from their ability to modulate the distribution of AgNWs on the electrospun membrane surface. Due to the inherent aggregation tendency of AgNWs and the hydrophobic nature of PVDF-based films, the drying process of AgNW solution typically exhibits a pronounced coffee-ring effect. This phenomenon arises from the faster evaporation rate at the droplet's edge, which induces an outward capillary flow that carries suspended nanowires toward the perimeter, ultimately forming ring-like deposits. Such non-uniform deposition is commonly observed during the fabrication of AgNW electrodes.

To systematically investigate the surfactant's role in suppressing the coffee-ring effect, AgNW suspensions with varying Triton X-100 concentrations (0, 0.05, and 0.1 wt%) were deposited on electrospun membranes from the same batch, and the resulting surface morphologies were characterized via optical microscopy (**Fig. 4.5d**–**f**). As shown, in the absence of surfactant (**Fig. 4.5d**), AgNWs exhibit severe non-uniform deposition with clear ring-like accumulation at the edges and sparse coverage in the central region. Upon the introduction of 0.05 wt% Triton X-100 (**Fig. 4.5e**), the coffee-ring effect is notably alleviated, and AgNWs begin to redistribute toward the center, although some localized clustering remains. At 0.1 wt% Triton X-100 (**Fig. 4.5f**), the deposition becomes markedly uniform, demonstrating that the coffee-ring effect is effectively suppressed, leading to significantly improved electrode homogeneity and quality.

Fig. 4.5a–c present the corresponding sheet resistance measurements of AgNW electrodes fabricated with varying Triton X-100 concentrations. In the absence of surfactant, poor droplet spreading leads to a non-uniform distribution of AgNWs and the formation of discontinuous conductive networks, resulting in relatively high sheet resistance. With increasing Triton X-100 content, the improved dispersion and film-forming quality of AgNWs lead to a gradual decrease in sheet resistance. At 0.1 wt%, the sheet resistance reaches approximately $1.9 \pm 0.63\ \Omega\ sq^{-1}$, representing the optimal surfactant doping level.

Fig. 4.5g schematically illustrates the underlying mechanism by which the surfactant suppresses the coffee-ring effect. On the left, the AgNWs-only ink exhibits pronounced edge pinning and Marangoni backflow, causing AgNWs to accumulate at the droplet edge and leading to poor film uniformity. In contrast, the right side demonstrates that the introduction of Triton X-100 reduces the contact angle and lowers surface tension at the droplet periphery. This induces inward Marangoni convection within the droplet, promotes centripetal flow, and facilitates uniform AgNW deposition by mitigating flow asymmetry.

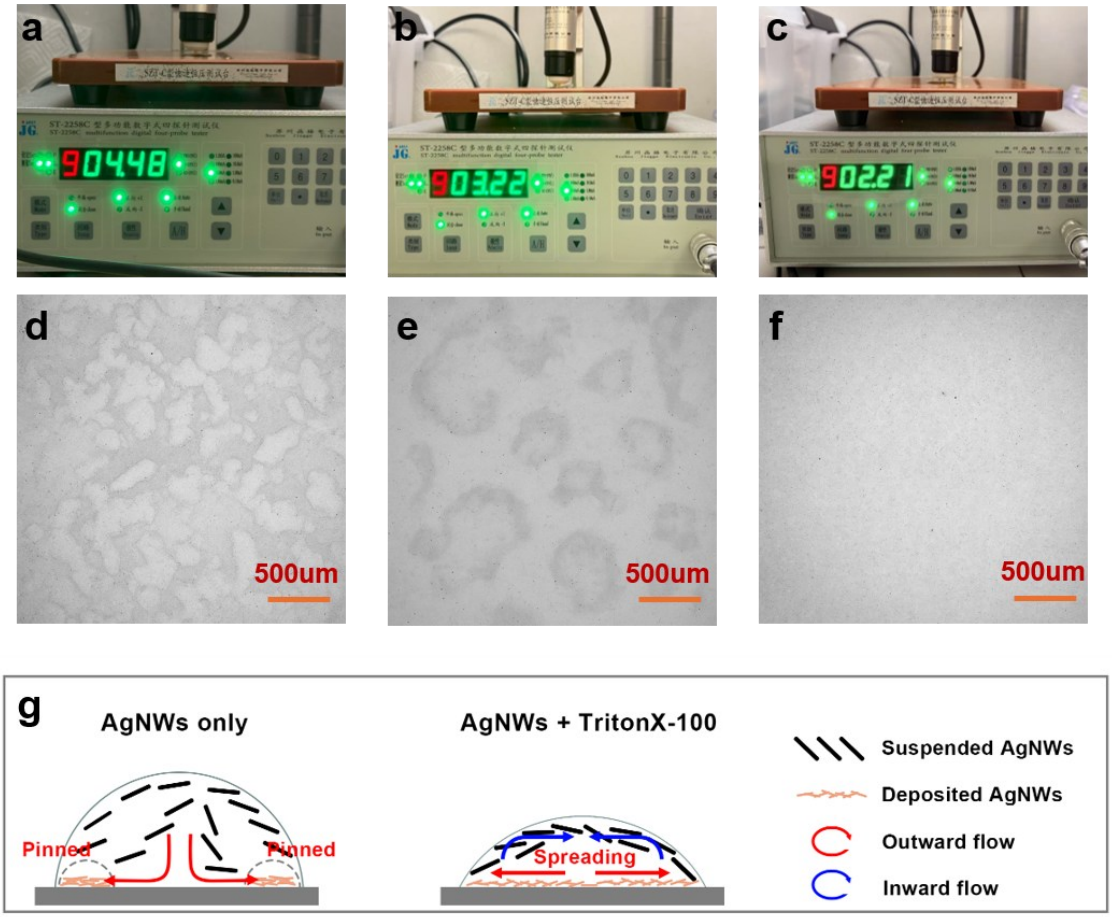

Fig. 4.5 Evaluation of surface conductivity and morphology of AgNWs electrodes with different Triton X-100 concentrations. (a–c) Real-time sheet resistance measurements of electrospun PVDF-based films with (a) AgNWs only, (b) AgNWs with 0.1% Triton X-100, and (c) AgNWs with 0.2% Triton X-100, respectively, measured under consistent conditions. (d–f) Corresponding optical microscopy images of the AgNWs layer on fiber surfaces from (a–c), demonstrating the improved uniformity and coverage with increasing Triton content. (g) Schematic illustration of the spreading behavior of AgNWs droplets during deposition.

4.3.2 Conductivity and stability under bending for sensing element

To evaluate the reproducibility and stability of the electrodes under bending conditions, **Fig. 4.6a and 4.6c** present the current-voltage (I-V) characteristics of AgNW and PVD-Cu electrodes under various bending curvature radii (2–0.5 cm). The bending radius (r) was calculated using the formula: $c=2r*\sin(l/2r)$, where c is the chord length and l is the arc length. The AgNW electrode exhibits nearly linear ohmic behavior even at high curvature, indicating excellent mechanical robustness and continuity of the conductive network. The corresponding SEM image (**Fig. 4.6b**) after bending at 0.5 cm reveals well-preserved nanowire interconnections with minimal breakage or delamination.

In contrast, the PVD-Cu electrode makes a marked deviation from linearity and a decrease in current with increasing curvature, even displaying hysteresis behavior, indicating crack formation and degradation in conductivity. The SEM image (**Fig. 4.6d**) clearly shows dense crack networks and structural failure, confirming poor mechanical resilience under deformation. This mechanical failure primarily arises from the mismatch in mechanical properties between the rigid Cu electrode layer and the flexible electrospun substrate. Moreover, sliding between individual nanofibers during deformation further disrupts the continuity of the metal film, leading to breakage of the conductive pathway.

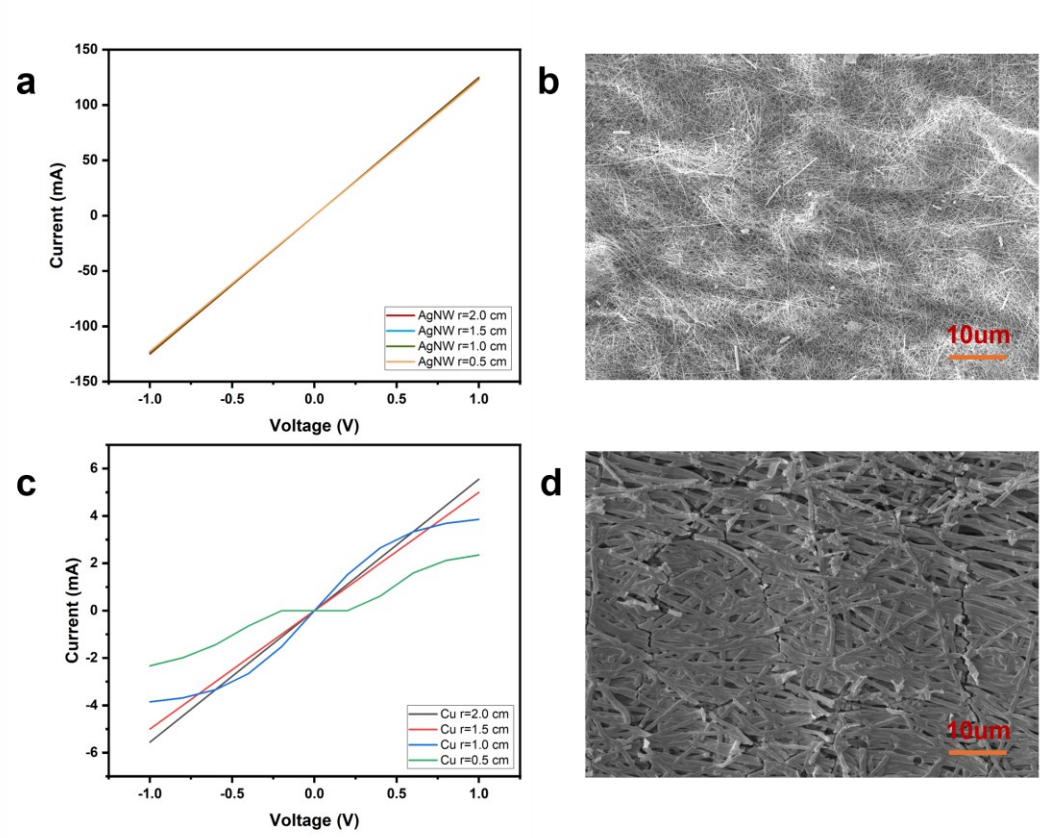

Fig. 4.6 (a) I–V curves of AgNW-based electrodes under different bending radii (r = 2.0, 1.5, 1.0, and 0.5 cm). **(b)** SEM image of AgNW electrode after bending (r=0.5 cm). **(c)** I–V curves of Cu electrodes under various bending radii (same with AgNW-based electrodes). **(d)** SEM of Cu electrode after r = 0.5 cm bending.

To further investigate the electrical stability of the AgNW electrode under repeated dynamic bending, **Fig. 4.7a** illustrates a cyclic bending test conducted with a fixed bending radius of 1.0 cm. The film was subjected to 10,000 bending cycles using a stepper motor, and the relative resistance change ($\Delta R/R_0$) was recorded in real time. As shown in **Fig. 4.7b**, $\Delta R/R_0$ began to increase gradually after approximately 1000 cycles and ultimately increased by only 16%, demonstrating reliable bending durability.

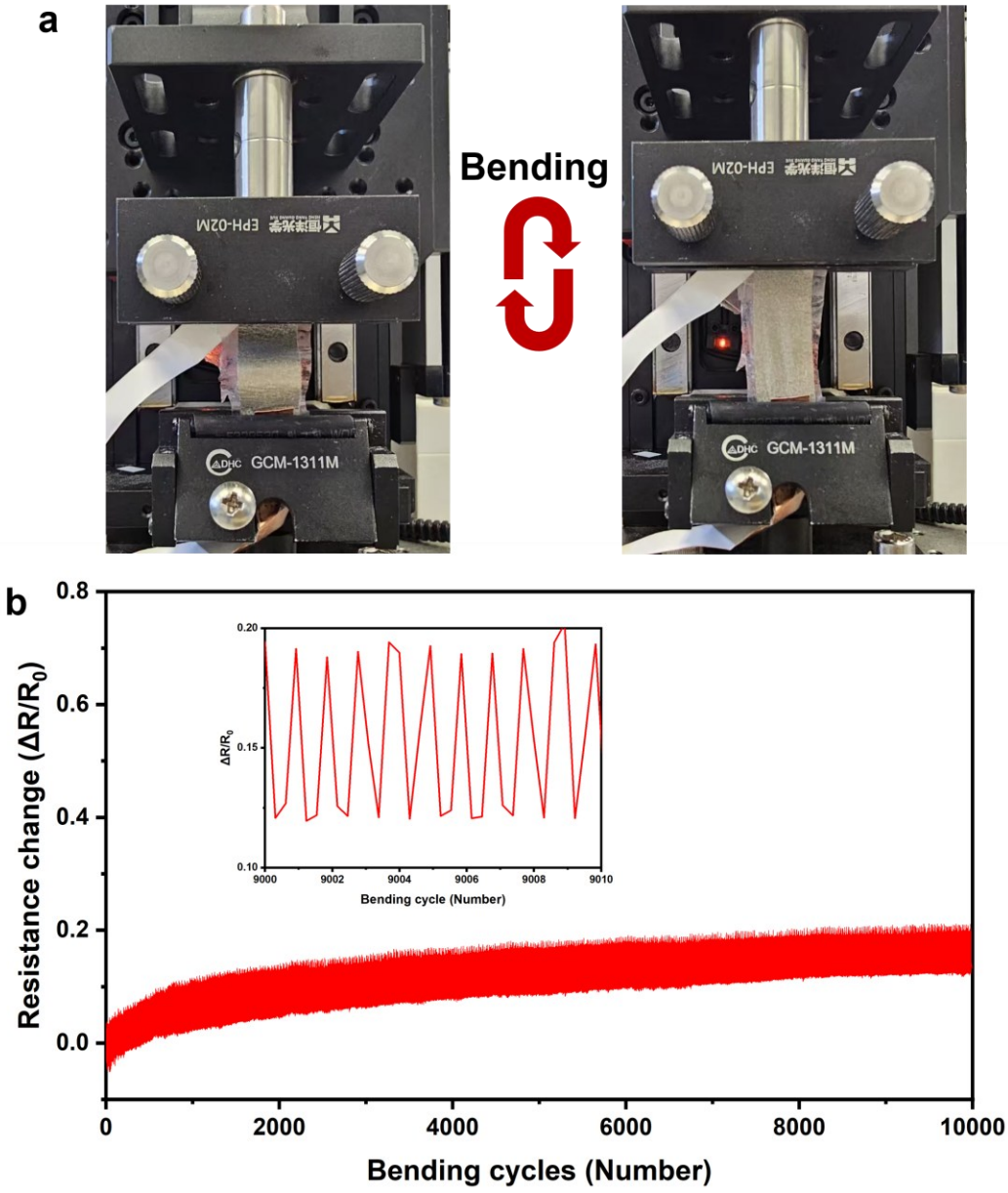

Fig. 4.7 (a) Photographs of the cyclic bending test setup with a fixed curvature radius of 1.0 cm using a motorized bending apparatus. (b) Relative resistance change ($\Delta R/R_0$) of the AgNWs electrode over 10,000 bending cycles under a constant bending curvature. Inset: enlarged view of $\Delta R/R_0$ fluctuation during cycles 9000–9010, indicating stable and repeatable resistance response.

4.3.3 Structure design of piezoelectric acoustic sensor

Physiological acoustic sensors are typically implemented in two modes: direct-contact and air-coupled designs. Because the target bioacoustic signals are very weak, air-coupled sensors often employ a cavity-backed structure to provide passive acoustic gain: low-amplitude sounds transmitted through the skin enter the sensor and are amplified by the back cavity before driving the diaphragm. Compared with direct-contact sensing, this coupling strategy can attenuate motion noise and movement-induced artifacts, since it relaxes the need for rigid mechanical contact while preserving sensitivity in the band of interest.

As mentioned earlier, the primary frequency components of physiological signals, such as heart and lung sounds, are mainly distributed below 1000 Hz, with subtle signals being more challenging to detect. Therefore, during the initial design phase of the acoustic sensor, the operating frequency range was defined as 20–1000 Hz. To achieve a relatively flat frequency response, the resonance peak of the vibration diaphragm was deliberately designed to lie outside this range. Based on this requirement, an edge-clamped polyimide (Kapton) thin film was selected as the diaphragm material.

Additionally, to enable the device to conform to different skin curvatures and ensure good skin contact, the outer housing of the sensor was fabricated from thermoplastic polyurethane (TPU) via 3D printing, forming both the upper and lower cavities as well as the supporting frame. The overall structure of the piezoelectric acoustic sensor is illustrated in **Fig. 4.8a.** From bottom to top, the layers include: a TPU housing with vent holes, PU foam for damping adjustment, a Kapton diaphragm laminated with a

piezoelectric thin film featuring top and bottom electrodes via EVA mat, a TPU supporting frame with a lower cavity, and a silicone sensing membrane for direct skin contact. The EVA web served a dual function: ensure the piezoelectric sensing unit fixed onto the diaphragm firmly and facilitate reliable contact between the diaphragm and the bottom electrode of the piezoelectric film to establish a stable electrical pathway. The final assembled sensor has an overall diameter of 42 mm and a total thickness of ~7.5 mm (**Fig. 4.8c**). The specific physical and mechanical parameters of the materials utilized in each layer of the sensor are summarized in **Table 4.2.**

Table 4.2 Specific physical and mechanical parameters of the materials utilized in each layer of the sensor.

Material	**Density (**g·cm^{-3}**)**	**Young's modulus (**GPa**)**	**Poisson's ratio ν**	**Thickness (**μm**) & Diameter (**mm**)**	**Notes**
PI (Kapton)	1.42	3.0	0.34	25 Ø 26	Effective clamp radius (5 mm)
Piezoelectric electrospun mat	0.42	0.34	0.34	70 Ø 20	Dielectric constant 12–15
EVA mat	0.95	0.01–0.05	0.33–0.49	40 Ø 14	Center bond
TPU (housing)	1.15	0.05	0.49	Upper: 2.8mm Lower: 4mm Ø 43	Ring support
Silicon	1.1	/	0.49	200	Acoustic impedance matching (1.2 MRayl)

Diaphragm design

For the diaphragm design, the Kirchhoff clamped circular plate theory was applied to

calculate the first-order resonance frequency of the sensor diaphragm. The diaphragm consists of a laminated structure composed of a 25 μm-thick PI film and a 70 μm-thick electrospun film (as shown in the key sensing unit in **Fig. 4.8b**). Under an effective clamping radius of a=12 mm, the first-order resonance frequency can be calculated using the following equation[221]:

$$f_{01} = \frac{\lambda_{01}^2}{2\pi R^2}\sqrt{\frac{Eh^3}{12(1-\nu^2)\rho h}}$$

λ_{01}^2 represents the dimensionless constant of the first-order vibration mode, approximately 10.21 for clamped boundary conditions. E the Young's modulus, ν the Poisson's ratio. By substituting the corresponding parameters summarized in **Table 4.2** into the equation, the first-order resonance frequency (f_{01}) is determined to be approximately 120 Hz, effectively magnifying the target signal under 100 Hz.

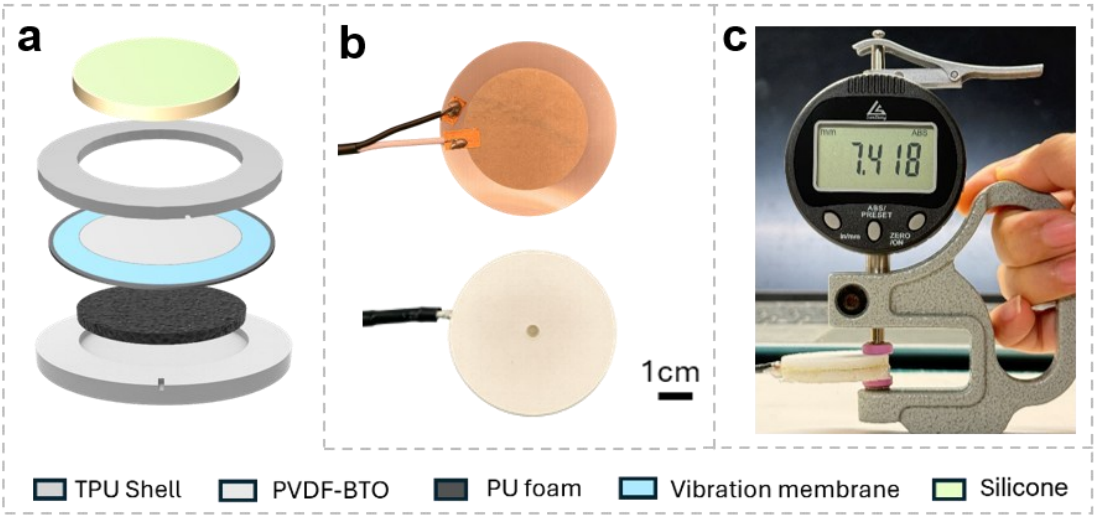

Fig. 4.8 (a) Schematic diagram showing the layered structure: TPU shell, PVDF-BTO piezoelectric layer, PU foam, vibration membrane, and silicone skin-contact layer. (b) Photographs of the assembled device: top view showing the key sensing unit integration

and bottom view showing the full-scale device. (c) Measured total thickness of the integrated sensor (~7.4 mm) using a digital micrometer. (The color legend below indicates the material assignment of each structural layer).

4.3.4 Characterization of sensor frequency response

The amplification effect of the back cavity is based on the relationship between the acoustic compliance, pressure, and volume. When a sound wave enters the cavity, the pressure increment follows the equation below:

$$p_{\mathrm{cav}} \approx \frac{\rho c^2 A_{\mathrm{in}}}{V} x$$

The cavity pressure is proportional to the membrane displacement, resulting in passive amplification. As illustrated in **Fig. 4.9a and b**, the back cavity diameter of 38 mm (bottom), and 26 mm (top), with a cavity depth of 4 mm. Considering the volumetric compliance of the diaphragm and substituting the parameters into the above equation, the pressure generated by a 1 μm displacement is approximately 0.6 Pa.

To investigate whether cavity coupling amplifies the incident acoustic waves, a COMSOL simulation was conducted based on the above structure. As shown in **Fig. 4.9 c**, the simulated sound pressure was probed at both the bottom and the diaphragm of the cavity. The results reveal a sound pressure amplification gain of approximately 1.8 times in the low-frequency region (<100 Hz) and about 1.2 times beyond this frequency range. Experimental results further confirmed the amplification effect of the cavity (**Fig.4.9 d**). The sensor electric output was tested before and after sealing the silicone membrane at different frequency, and the amplitudes were converted into

sensitivity values. The results show that, prior to cavity sealing, the sensor sensitivity at 50 Hz was around 200 mV/Pa, while the sensitivity remained relatively flat across other frequency range (average ≈ 32 mV/Pa). After sealing the cavity, a significant low-frequency enhancement was observed, with an average sensitivity of 47 mV/Pa above 100 Hz, indicating a gain of approximately 1.5 times. These results are consistent with the simulation, further confirming the cavity-coupling amplification effect.

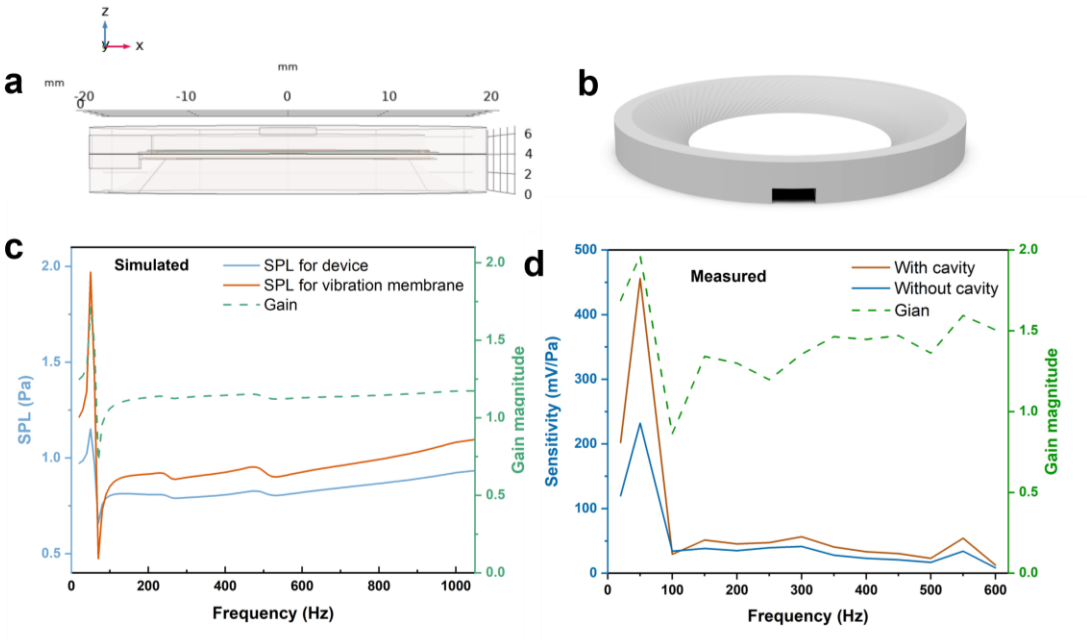

Fig.4.9 Modeling and experimental validation of cavity-backed coupling of the acoustic sensor. (a) Cross-section and COMSOL setup of the sensor showing the diaphragm and TPU frame forming the back cavity. (b) 3D concept of the top cover and back cavity. (c) Simulated frequency response: sound pressure at the device (SPL for device), at the diaphragm surface (SPL for vibration membrane), and the resulting gain (ratio), demonstrating passive amplification by the cavity. (d) Measured response: voltage sensitivity with and without the cavity and the derived gain.

To evaluate the frequency response of the acoustic sensor, a stepwise sinusoidal sweep from 20 to 1000 Hz was applied in 20 Hz intervals. At each frequency point, the sensor was exposed to a fixed-duration excitation, and the output voltage was processed through FFT to determine the response amplitude. As shown in **Fig. 4.10**, the device exhibited strong sensitivity in the low-frequency regime (<200 Hz), with peak amplitude occurring near 120–150 Hz. However, a rapid decline in signal strength was observed beyond 650 Hz, with the output dropping below 5 mV and approaching the noise threshold. This implies a reduced detection capability in the high-frequency range. It should be noted that the excitation sound pressure level was not constant across all frequencies, as the output of the speaker inherently varies with frequency. While this introduces some uncertainty in absolute sensitivity comparison across the spectrum, the trend still reflects the dominant low-frequency responsiveness of the sensor.

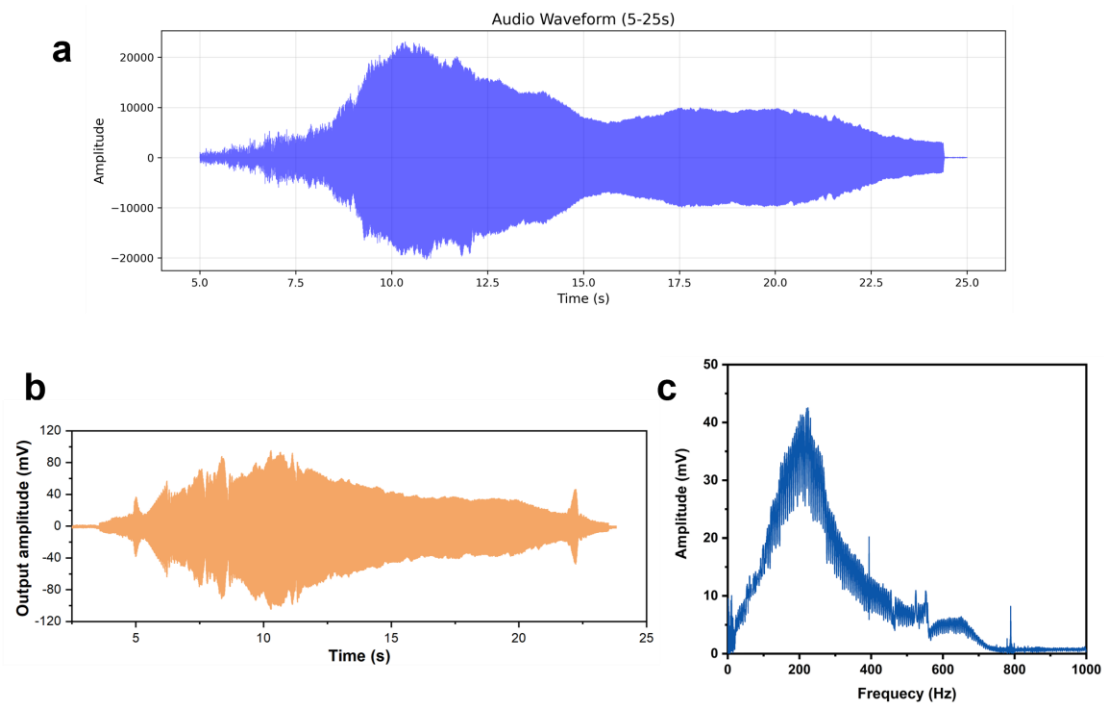

Fig. 4.10 Time-domain comparison between the input sweep audio (20–1000 Hz) and

the sensor output. (a): reference input audio waveform (5–25 s, A.U.). (b) sensor corresponding voltage output and FFT analysis (c).

4.4 Conclusion

In this chapter, we developed a flexible acoustic sensor with excellent conformability, mechanical stability, and reliable signal response. The core sensing component consists of an electrospun piezoelectric membrane integrated with a silver nanowire (AgNW)-based flexible electrode. The AgNW network, fabricated via electrospraying in combination with surfactant-assisted dispersion, exhibited strong adhesion to the fibrous substrate and retained stable conductivity even after 10,000 bending cycles, significantly outperforming rigid metal electrodes deposited by magnetron sputtering.

Building upon the piezoelectric sensing unit, we further designed a multilayer acoustic sensor incorporating a back cavity. The flexible outer housing endowed the device with structural adaptability, allowing it to conform to curved skin surfaces. Through acoustic impedance matching and cavity resonance, the sensor demonstrated enhanced sensitivity to low-frequency acoustic pressure. Beyond 100 Hz, the sensor maintained a relatively flat sensitivity of approximately 47 mV/Pa. Electrical and acoustic characterizations confirmed the effective dynamic response within the 20–600 Hz range. This work provides a robust design strategy for wearable stethoscope applications and lays the groundwork for high-fidelity physiological signal monitoring in future biomedical devices.

CHAPTER 5 ACOUSTIC SENSOR OPTIMIZATION, PERFORMANCE EVALUATION, AND PHYSIOLOGICAL APPLICATIONS

5.1. Introduction

With the development of acoustic electronic stethoscopes, the continuous acquisition of physiological acoustic signals has become increasingly important for long-term wearable health monitoring. This places higher demands on the comfort of acoustic sensors and the stability of continuous signal acquisition. However, most existing acoustic stethoscopes employ rigid metallic housing, which compromise comfort during prolonged wear and are prone to excessive environmental noise pickup.[222, 223] Given that cardiac events are often sudden and unpredictable, continuous and long-term heart sound monitoring plays a vital role in early detection and prevention.[223-225] Heart sounds are typically characterized by low energy, rhythmic patterns, and a primary frequency range of 20–200 Hz, making their accurate acquisition and feature extraction critical for assessing cardiac function.[226-229]

Similarly, pulmonary disease diagnostics rely heavily on the auscultation and analysis of lung sounds. Normal lung sounds and abnormal sounds differ significantly in their acoustic features.[230-232] For example, emphysema is often accompanied by crackles, while wheezing typically presents as high-frequency, short-duration signals concentrated in the 100–1000 Hz range.[233, 234] Therefore, for sensors designed for cardiopulmonary monitoring, the operational frequency range should span 100–1000 Hz, with enhanced sensitivity at lower frequencies to improve the detection of weak

heart sounds and low-frequency lung components.[235, 236] Long-term monitoring also introduces additional requirements for wireless data acquisition systems, including extended battery life, multi-channel support, and low intrinsic noise, to ensure stable performance in diverse real-world environments.[237]

To address these challenges, this chapter builds upon the previous analysis and combines plate-shell vibration theory with finite element simulations to propose a structural optimization strategy. By incorporating a high-modulus PC stepped shoulder ring as the lower boundary support, a TPU layer for flexible sealing and conformal skin contact, and a copper upper ring to clamp the PI diaphragm from both sides, the sensor achieves a near clamped-edge boundary condition. This design significantly increases the effective boundary stiffness (K_{eff}), redistributes vibrational energy from the dominant low-frequency peak to the mid- and high-frequency bands, suppresses response fluctuations within the operating range, and broadens the effective bandwidth without compromising comfort.

A unified acoustic calibration and evaluation framework was established to standardize performance measurements. Full-chain calibration was performed using a 94 dB (1 kHz) reference tone, with Z-weighted corrections applied in the low-frequency range to calculate point-by-point sensitivity (V/Pa). The framework also evaluates dynamic range, linearity, SNR, and in-plane directional response. In addition, short-time Fourier transform (STFT) analysis was employed for time-frequency separation of mixed signals, enabling assessment of feature separability and noise robustness under in-vivo

conditions.

The in-vivo experiments covered multiple anatomical sites, including heart sounds at the anterior chest, arterial pulse signals at the carotid and radial arteries, and lung sounds from the upper right posterior lung field. The heart sound measurements focused on the S1 and S2 components, their intervals, and splitting characteristics; arterial recordings analyzed the P1 and P2 peaks, upstroke time (UT), and normalized area index (%MAP); while lung sound testing examined broadband energy distributions from 100 to 800 Hz and phase-locked time–frequency features across the respiratory cycle. These results demonstrate that structural optimizations yield stable signal acquisition and reliable extraction of key physiological features, providing a solid basis for subsequent development of array-based configurations and beamforming strategies.

5.2. Experimental section

5.2.1 Improve effective stiffness

To improve the effective stiffness of the diaphragm structure, a rigid copper support ring was introduced. The copper ring was fabricated via laser cutting, with an inner diameter of 20 mm, an outer diameter of 30 mm, and a thickness of 100 μm. To bond the copper ring with the PI (polyimide) diaphragm, a high-strength UV-curable adhesive, Kafuter K-3725H, was applied. This resin exhibits a Shore D hardness of approximately 69 (measured according to GB/T 531-1999) and an elongation at break of about 120%, ensuring the rigidity for effective stiffness. Support housing adopts a hard-soft concentric ring to realize a near-clamped boundary with a compliant periphery.

The inner ring is high-modulus Polycarbonate (PC) incorporating a step shoulder; the outer ring is TPU (Shore-A 90) for conformity and sealing. The ring is fabricated in one pass by dual-material FDM. During assembly, a copper ring (top clamp) and the PC shoulder (bottom clamp) provide stable clamping and define the effective radius R_{eff}, thereby increasing the effective stiffness K_{eff} and shifting the resonance upward. Through-holes (Ø1.0 mm, 1.8 mm pitch) or dovetail grooves at the PC-TPU interface enable mechanical interlocking of TPU.

5.2.2 Measurements for the physiological signal

Wireless multi-channel acquisition device

To facilitate physiological signal monitoring, a developed 8-channel wireless acquisition system was employed in this study by our member for acoustic data collection. Each channel is preliminarily amplified by a high-input-impedance instrumentation amplifier (INA). The circuit design is illustrated in **Fig. 5.1a.** An STM32 microcontroller serves as the core processor for analog-to-digital conversion, while an ESP32 Wi-Fi module is used for wireless data transmission to the PC terminal. The sampling rate is set at 5 kHz. On the software side, a 50 Hz notch filter is implemented in LabVIEW to suppress power-line interference. As shown in **Fig. 5.1b**, the acquisition module is powered by a 2500 mAh lithium-ion battery, providing continuous operation for up to 20 hours. To minimize electromagnetic interference, the entire system is enclosed in a 3D-printed aluminum alloy case for EMI shielding, and all interconnecting cables are shielded as well.

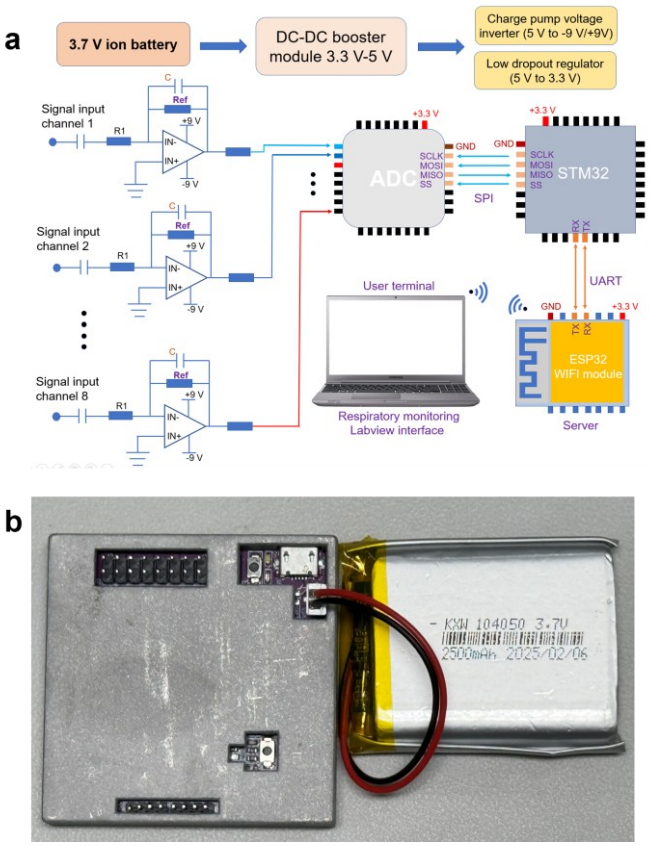

Fig. 5.1 System schematic and hardware implementation of the wireless acoustic monitoring module. (a) Block diagram of the wireless multi-channel acoustic acquisition and transmission system. (b) Photograph of the assembled hardware module integrated with a rechargeable lithium battery, PCB board.

Acquisition of heart and lung sounds

For cardiac sound acquisition, healthy volunteer was recruited and instructed to sit quietly in a natural seated posture within a low-noise environment (ambient noise level approximately 50 dB). The subjects maintained a steady and relaxed breathing rhythm during signal recording. Each auscultation site was recorded for 60 seconds.

Physiologically, the closure of the mitral and tricuspid valves generates the first heart

sound (S1), while the closure of the aortic and pulmonary valves produces the second heart sound (S2). To capture both components clearly, the sensor was positioned between the mitral and Erb's auscultation points, corresponding to region 4 in **Fig. 5.2a**.

For lungs sound acquisition, to minimize interference from heart sounds, recordings were performed on the posterior thorax. The sensor was placed on the right upper to middle lobe area near the first and second thoracic vertebrae, corresponding to region 1 in **Fig. 5.2b**, where bronchial breath sounds can be effectively detected. To reduce motion artifacts and frictional noise, the sensor was affixed to the skin using medical-grade double-sided adhesive tape (3M-2477P). For carotid and peripheral pulse signal acquisition, the sensor was secured using an elastic strap around the neck and upper arm to ensure stable contact with the skin during measurement.

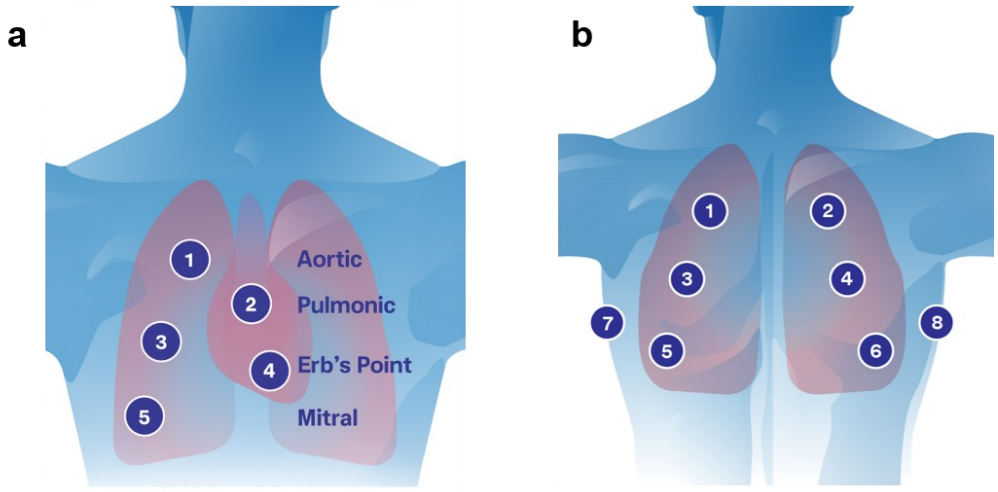

Fig. 5.2 Standard auscultation sites for pulmonary and cardiac acoustic signals. (a) Anterior view illustrating five classical auscultation points for heart sounds. (b) Posterior view showing eight standard auscultation sites for lung sounds.

Data preprocessing

The acquired raw signals were first normalized and denoised. A fourth-order bandpass filter was applied to remove low-frequency baseline drift and high-frequency background noise, with cutoff frequencies set to 20–200 Hz for heart sounds and 100–1000 Hz for lung sounds. For heart sound signals, S1 and S2 components were segmented using envelope detection combined with an autocorrelation-based windowing algorithm. For lung sound signals, frequency content was monitored and analyzed using STFT.

5.3 Results and discussion

5.3.1 Device modeling and modification

For any vibration mode, the diaphragm resonance can be approximated by

$$f_r = \frac{1}{2\pi}\sqrt{\frac{K_{\text{eff}}}{M_{\text{eff}}}}$$

where K_{eff} is the effective stiffness of that mode and M_{eff} is the modal mass. Increasing K_{eff} or reducing M_{eff} raises resonance frequency.

For the bending-dominated circular plate, the fundamental frequency is

$$f_{01}^{(\text{plate})} \approx \frac{\lambda_{01}^2}{2\pi R^2}\sqrt{\frac{D}{\rho h}}$$

in which bending stiffness $D = \frac{Eh^3}{12(1-\nu^2)}$, R is the effective radius, E the Young's modulus, ν the Poisson's ratio, ρh the areal mass density, and $\lambda_{01}^2 \approx 10.21$ for a clamped boundary. In last chapter, a TPU support ring together with a TPU upper housing was

used as the clamping boundary. Because the modulus of TPU is low (Shore-A 90, ~10−50 MPa), the boundary behaves as elastic support rather than a strict clamp. This lowers K_{eff} and introduces extra boundary damping, leading to a rapid amplitude roll-off above 600 Hz and preventing the device from reaching the intended resonance band.

Based on this, the boundary support was upgraded to a hard-soft concentric ring. The inner ring at the stepped shoulder was changed to PC (E≈2.3 Gpa) and used as the lower clamping layer, while the outer ring remained TPU for conformity and comfort. A Cu circular ring was introduced as the upper clamping layer. The PI diaphragm carrying the piezoelectric film is sandwiched between the upper and lower clamps, establishing a strictly clamped edge and stabilizing the effective radius R_{eff}. In theory, the introduction of PC and the copper ring significantly increases the effective stiffness, shifts the first resonant frequency into the targeted range, and enhances the mid-to-high-frequency output amplitude, indicating improved mechanical resonance and transduction performance.

To test the rationale of the design change, we augmented the previous model with a clamped edge and examined the resulting frequency response. As shown in **Fig. 5.3a**–**d**, with a compliant support the fundamental mode exhibits an axisymmetric drumhead shape, whereas higher-order resonances are weak and involve substantial edge motion. After enforcing a clamped boundary, the overall displacement slightly decreases but mid-to-high-order resonances become pronounced; nodal lines crowd toward the rim, indicating increased rotational stiffness at the boundary and more localized, symmetric

deformation. **Fig. 5.3e** compares the simulated electrical outputs with and without the copper ring (under 1Pa sound pressure): the low-frequency peak is reduced and shifts slightly upward, while a prominent mid-band peak near 0.5 kHz emerges and several smaller peaks appear above 0.7 kHz. These results confirm that clamping raises the effective stiffness, redistributing energy from a single low-frequency peak to the mid-high band and improving in-band electromechanical transduction.

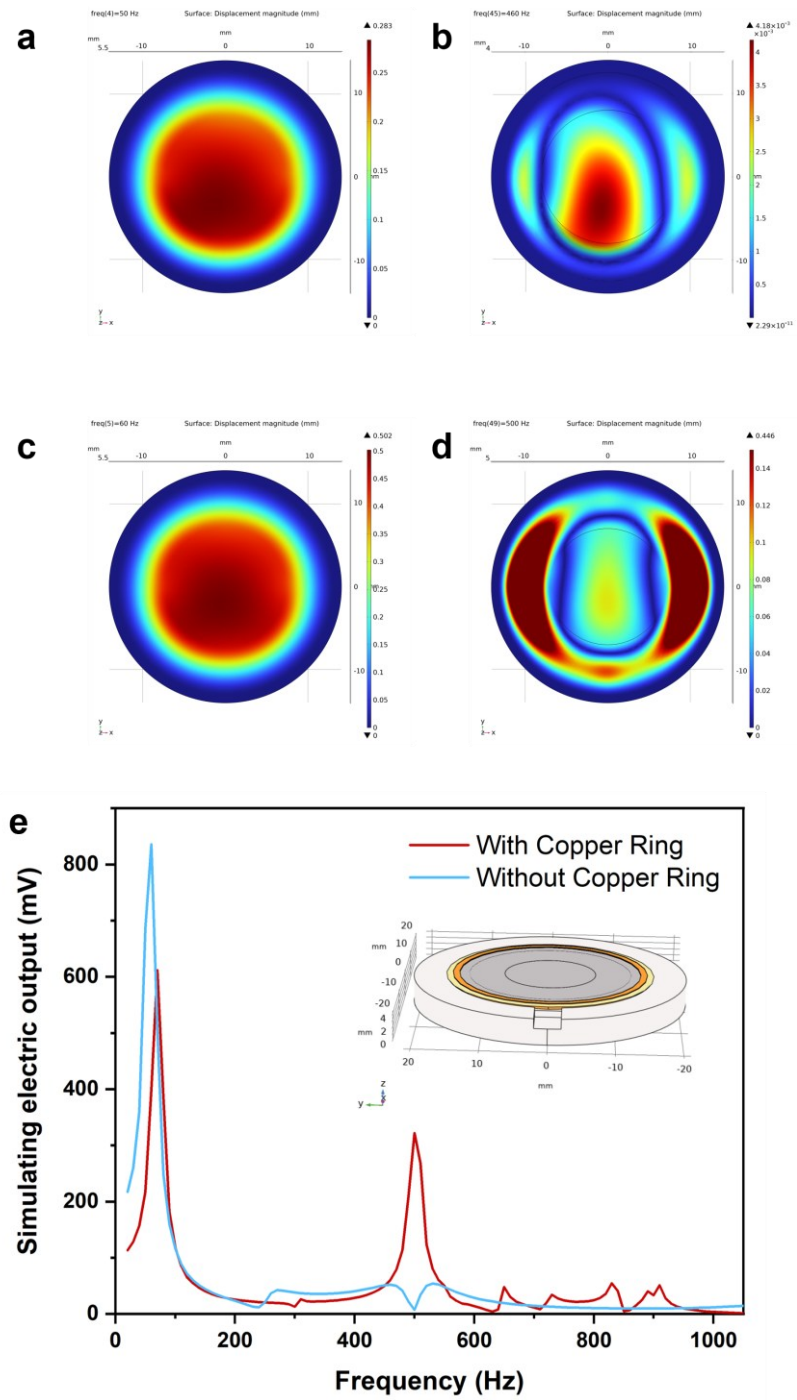

Fig. 5.3 Simulation of modal displacement and electrical response with and without copper ring. (a, b) show the first and higher-order modes without the copper ring; (c, d) show the corresponding modes with the copper ring. (e) Simulated electrical output of the device under frequency sweep from 20–1000 Hz. The red curve represents the sensor with the copper ring, and the blue curve without it.

5.3.2 Performance evaluation of the improved acoustic sensor

Frequency-domain voltage output and sensitivity

After verifying the positive effect of the clamped boundary on bandwidth extension, we evaluated the performance of the improved device. As shown in **Fig. 5.4a**–**b**, the amplitude response was measured from 20–1000 Hz with a 10 Hz step, and the corresponding voltage sensitivity was computed under a unified SPL calibration (a 94 dB, 1 kHz sound calibrator was used for link-gain calibration). Because the loudspeaker loses to reach the standard 1 Pa SPL below 150 Hz, the low-frequency SPL was read with a Z-weighted sound level meter for subsequent sensitivity calculation. As shown in **Fig. 5.4b**, the measured fundamental resonance appears around 60 Hz and the second resonance near 510 Hz, consistent with the simulations and showing a similar trend. The measured amplitudes are smaller than the simulated ones, because the simulations were conducted in vacuum whereas the experiments are influenced by fabrication testing factors and by air-radiation added mass and damping. Consequently, the device exhibits low-frequency, resonance-dominated gain: the average sensitivity below 150 Hz is 75.6 mV/Pa, while the response is relatively flat in the mid-to-high band (150–1000 Hz) with an average sensitivity of about 36 mV/Pa. The bandwidth is successfully extended to 1000 Hz with ripple $< \pm 3$ dB, matching the intended application range. The disparity in response magnitude caused by the two resonance peaks can be mitigated by circuit compensation by using active notch or shelving equalization to suppress the excessive peak and yield a more faithful representation of physiological signal

amplitude.

Signal-to-noise ratio (SNR)

After confirming the bandwidth benefit of the clamped boundary, we evaluated the device SNR with our data-acquisition chain. **Fig. 5.4c**–**d** shows tests in which the sensor was driven by a fixed sound source at two selected tones. Across the full measurement band, the SNRs at 200 Hz and 900 Hz are approximately 65 dB and 16 dB, respectively. **Fig. 5.4d** presents the FFT of the two recordings, revealing no noticeable harmonics and a relatively flat noise floor, which supports the validity of the results.

Directionality

For physiological signal monitoring, especially heart and lung sounds, the azimuthal directivity provides a better basis for subsequent array auscultation zoning and beamforming planning. As shown in **Fig. 5.4e**, a polar plot of the sensor's relative electrical output versus azimuth angle was obtained. The sound source was placed 1 cm above the diaphragm along the normal surface and rotated in 45° increments at a constant SPL (Z-weighted, output reported as RMS voltage). The device shows an asymmetric, undulating azimuthal dependence, with a peak-null difference of about 12–15 dB. This behavior is related to the anisotropy of the sensing element fabricated in Chapter 3; the response is larger along the fiber-orientation direction.

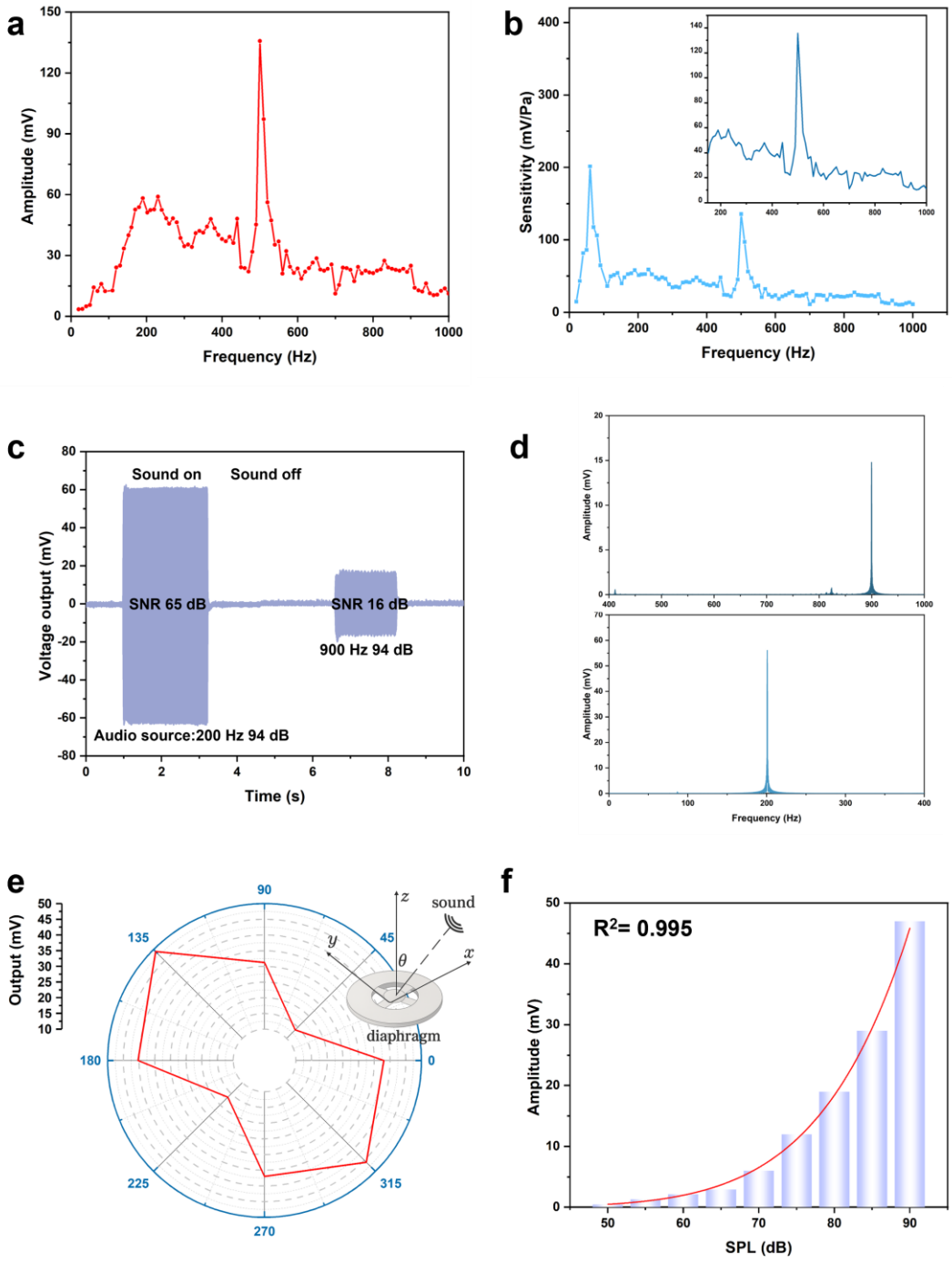

Fig. 5.4 Characterization of acoustic sensing performance. **(a)** Frequency-domain voltage output of the device under a broadband acoustic input (200–1000 Hz). (b) Frequency-dependent calculated sensitivity (mV/Pa), inset: enlarged sensitivity of frequency range 200–1000 Hz. (c) Time-domain and corresponding FFT process (d)

voltage output in response to 94 dB sound signals at 200 Hz and 900 Hz. (e) Polar plot of directional sensitivity under sound incidence from different angles. (f) Output amplitude versus SPL ranging from 50 to 90 dB.

Dynamic response

Beyond sensitivity, we evaluated the dynamic response range at different sound pressure levels. The minimum detectable SPL is set by the in-band noise in the sound-off window, and the maximum usable SPL is limited by linearity and distortion. As shown in **Fig. 5.4f**, the output amplitude fits well as a function of SPL, with R^2=0.995, indicating an approximately linear pressure response from 50 to 94 dB without noticeable compression.

For heart and lung sounds, most energy lie around 40–60 dB. Therefore, we played a known heart-sound clip at 50 dBZ inside an acoustic enclosure. The device recorded the corresponding time-domain acoustic response, and we computed STFTs for both the original audio and the recorded signal to compare their time-frequency features. To better emulate real organs where airborne sound and structural vibration coexist, we set up an acoustic-vibration platform. As shown in **Fig. 5.5a**, it consists of a PTFE chamber with an internal loudspeaker and a silicone membrane on top to mimic skin motion. The sensor is placed on the membrane to sense the mixed vibration and sound. **Fig. 5.5b** compares the original input of normal heart sound (lower) with the recorded signal (upper) and their STFT spectrograms. The device reproduces each heartbeat clearly, and the main frequency band overlaps with the input. To further quantify signal fidelity,

we evaluated the similarity between the original clip and the sensor-recorded waveform in the heart-sound band (20–200 Hz). After resampling, band-pass filtering, and time alignment by maximizing normalized cross-correlation, the time-domain similarity was calculated with the maximum normalized cross-correlation (NCC) = 0.646 and the Pearson's correlation coefficient (r) = 0.646, indicating a moderate-to-good waveform resemblance given the different acquisition chains (audio playback and propagation vs. mechano-electrical transduction) and the non-negligible electronic noise in the recording system. More importantly, the frequency-domain agreement was high, with an average magnitude-squared coherence of 0.909 over 20–200 Hz, demonstrating that the key low-frequency spectral content is well preserved. Consistently, the time-frequency structures also matched well, with a log-STFT spectrogram cosine similarity of 0.985 (mean-centered), confirming that the device captures the heartbeat rhythm and its dominant frequency band with high fidelity.

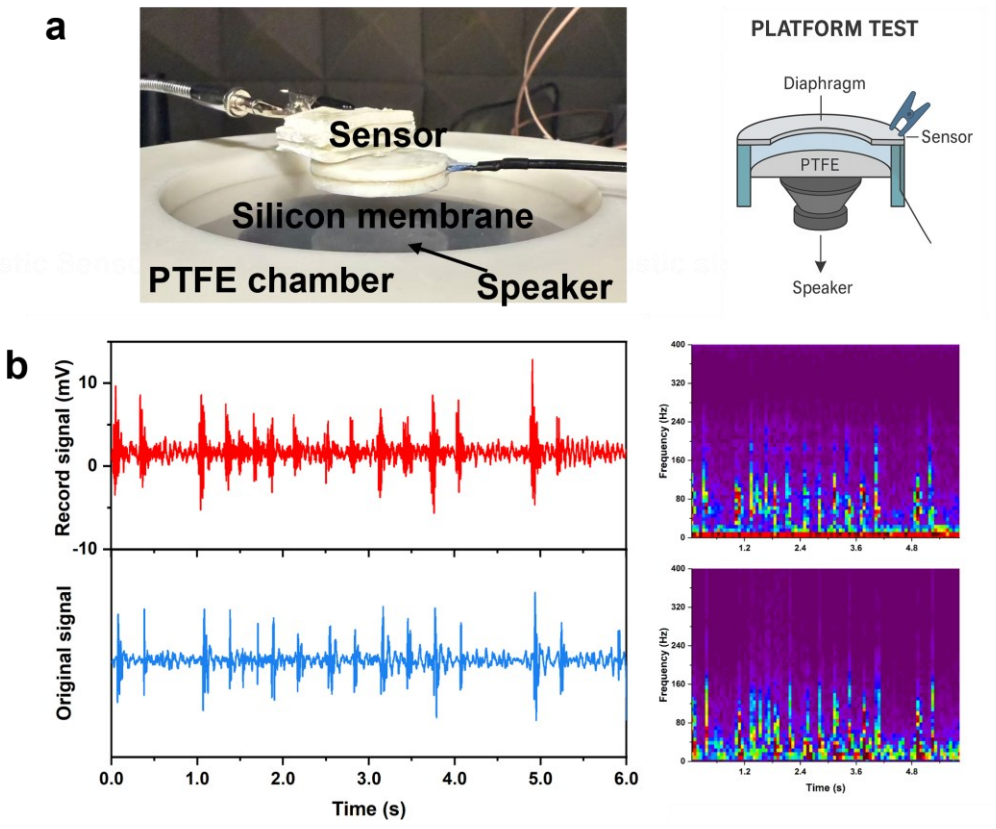

Fig. 5.5 Playback platform and reconstruction of physiological sounds. (a) PTFE chamber with an internal loudspeaker covered by a silicone membrane that emulates skin motion; the sensor is placed on top to sense a mixture of airborne and structure-borne excitations. (b) A segment of normal heart sound was played back at 50 dBZ in the acoustic enclosure. The device output was recorded and compared with the original input. Time-domain traces (left) and STFT spectrograms (right).

5.3.3 Real physiological signal detection

Breath and pulse detection

After calibration, we evaluated performance in practical settings to observe stability under background noise and to verify detectability of physiological signals. We first

selected high-amplitude targets for a detectability check. **Fig. 5.6a-c** reports three placements using an elastic strap: the chest, the carotid site on the neck, and the radial artery on the wrist. The subject sat at rest and performed spontaneous breathing and breath-hold. In **Fig. 5.6a** each thoracic excursion is clearly resolved, and cardiac components remain visible during breath-hold. In **Fig. 5.6b** periodic tracheal breath sounds with fine temporal detail are observed at the neck, and the carotid arterial waveform shows the early systolic peak P1 and the late systolic peak P2, which enable computation of augmentation pressure and augmentation index to assess wave reflection and arterial compliance. In **Fig. 5.6c** the radial pulse is recorded with stable beat-to-beat morphology. The upstroke time (UT) from foot to peak and the normalized mean-level metric (%MAP), defined as the cycle-average level relative to the P1 amplitude, are extracted for peripheral waveform assessment and can indicate changes in peripheral resistance or stenosis risk. These results show that the device acquires cardiopulmonary signals reliably in the presence of background noise and supports downstream feature extraction.

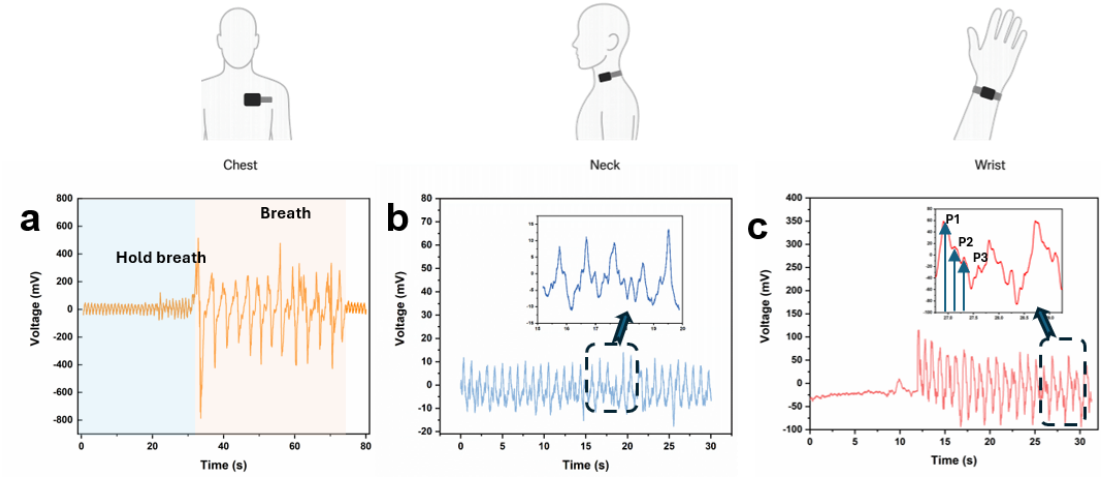

Fig. 5.6 In-vivo recordings at three anatomical sites. Icons on top indicate sensor placement. (a) Chest placement. The blue segment corresponds to breath-hold and the orange segment corresponds to spontaneous breathing. (b) Neck placement. The inset zooms into one breathing cycle. (c) Wrist placement. The inset marks several pulse peaks P for heart rate and rhythm estimation.

Cardiac sound detection

To assess feasibility of detecting heart sounds at rest during normal breathing, we fixed the sensor to the precordium with 3M medical tape at a site midway between the mitral and Erb's auscultation points, targeting the first (S1) and second (S2) heart sounds. As shown in **Fig. 5.7a**, the top panel is the raw chest signal in which the largest amplitude follows thoracic motion with respiration. We then separated physiological components with filtering: the respiratory wave lies mainly below 1 Hz, pulse and body-motion energy occupy 0 to 10 Hz, and heart-sound energy is concentrated from about 20 to 150 Hz. Using high pass filtering we isolated a heart-sound channel (blue) with clear contrast to the low noise floor. The STFT of the original trace (**Fig. 5.7d**) shows periodic broadband bursts time aligned with the heart sounds, with most energy below 200 Hz, confirming the feasibility of heart-sound monitoring. **Fig. 5.7b** zooms a five-second segment of the separated channel and reveals S1 and S2 in each cardiac cycle. S1 corresponds to atrioventricular valve closure and marks the onset of systole, while S2 corresponds to aortic and pulmonic valve closure and marks the end of systole. A further zoom in **Fig. 5.7c** allows direct reading of the S1–S2 interval and the S2–S1 interval,

which represent systolic and diastolic durations, respectively; the individual durations of S1 and S2 can also be measured for later feature extraction. Inspiratory splitting of S2 is visible and phase-locked to the breathing cycle. Taken together, these results show stable detection of heart sounds in the target band and enable extraction of rhythm, systolic and diastolic timing, and S2 splitting.

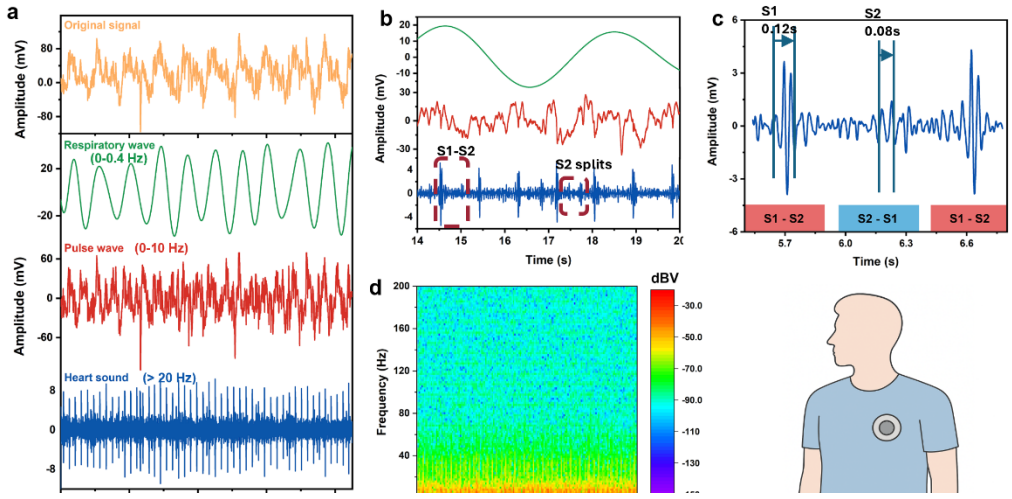

Fig. 5.7 Cardiac sound detection and band separation in vivo. (a) Chest recording and three-band decomposition: original trace (top), respiratory component (≈0–0.4 Hz, green), pulse/BCG band (≈0–10 Hz, red), and heart-sound band (>20 Hz, blue). (b) Overlay of the bands. The heart-sound channel resolves S1–S2 pairs and shows an instance of S2 splitting during inspiration. (c) Zoomed segment of the heart-sound channel with S1 and S2 labels; example S1–S2 and S2–S1 intervals are indicated. (d) STFT spectrogram (0–200 Hz, color in dBV).

Lungs sound detection

To validate the device's capability for respiratory monitoring, in-vivo lung sound

recordings were conducted at the right middle lobe, a region commonly used for bronchial breath sound auscultation. As illustrated in **Fig. 5.8a**, the raw signal (blue curve) exhibits broadband voltage fluctuations corresponding to airflow and tissue vibration during respiration. To minimize low-frequency artifacts from chest wall movement, a high-pass filter was applied (red curve), which preserved the dominant broadband respiratory components while effectively suppressing motion-induced baseline drift. The corresponding STFT spectrogram (**Fig. 5.8b**) reveals a continuous spectral distribution primarily in the 100–1000 Hz range, consistent with characteristic lung sound signatures. The relatively flat noise floor without strong tonal peaks indicates that the sensor offers stable and clean respiratory signal acquisition, supporting its application in wearable pulmonary health monitoring.

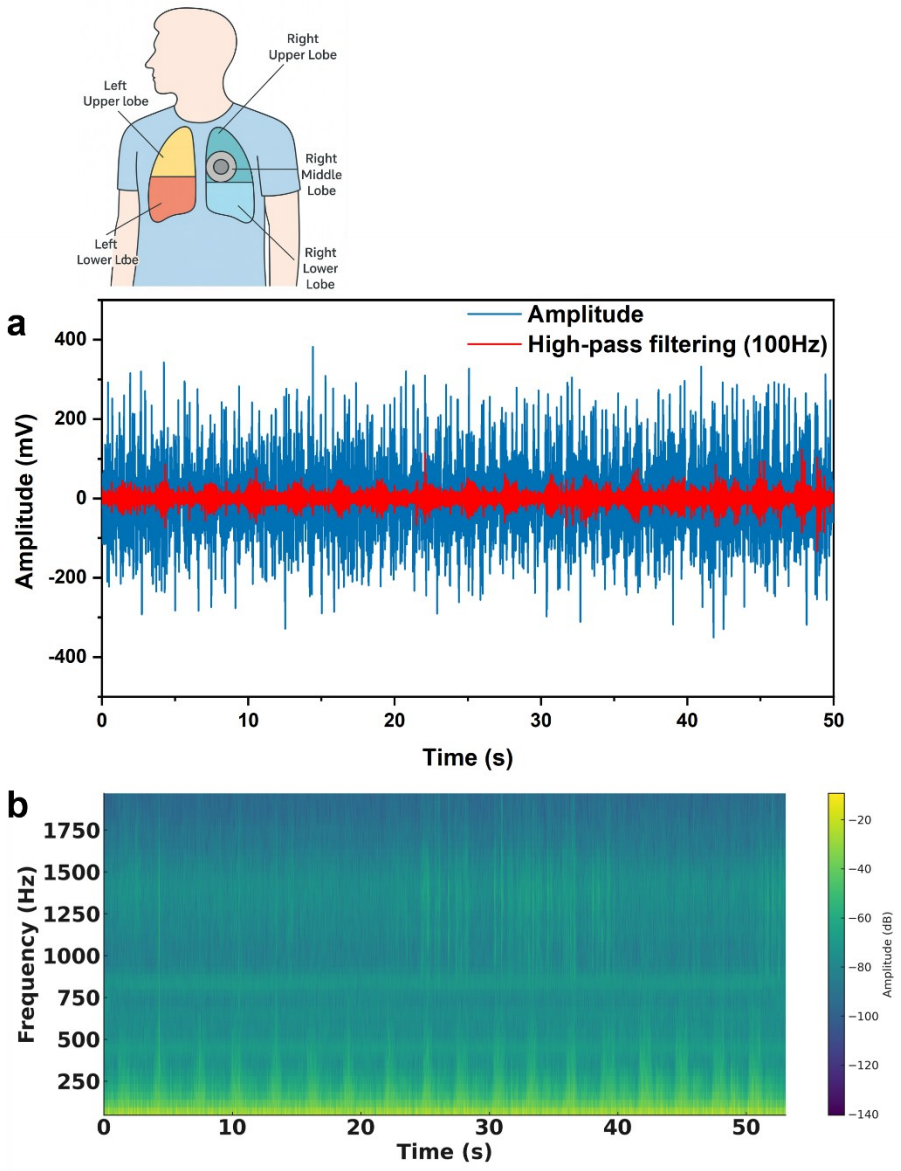

Fig. 5.8 In-vivo lung sound recording at the right middle lobe. (a) Time-domain signal from the chest: the blue trace is the raw voltage and the red trace is the same signal after a high-pass filter (>100 Hz), which suppresses low-frequency chest motion while preserving the broadband lung component, and (b) corresponding STFT spectrogram. The noise floor is relatively flat with no strong tonal artifacts.

5.3.4 Benchmark with other electronic stethoscopes

To assess the relative merits of our device, we compared it with commercial electronic stethoscopes and representative acoustic sensors reported in recent literature (**Table 5.1**). The set includes different transduction mechanisms, namely piezoresistive, piezoelectric, MEMS capacitive, and triboelectric. We summarized device size and mass, frequency-response range, voltage sensitivity under a unified calibration, and end-to-end SNR. Because application targets differ, the intended bandwidths are not identical across devices. Within the same mechanism class and comparable target band, our sensor achieves higher sensitivity, smaller form factor and mass, and a superior SNR while maintaining a practical bandwidth, indicating suitability for wearable cardiopulmonary monitoring.

Table 5.1 Performance comparison of reported acoustic sensors (Piezoelectric, Triboelectric, Capacitive).

Device / Material	Prin-ciple	Structure / Type	Size	Frequency (Hz)	Sensitivity (mV/Pa)	SNR (dB)	Notes	Ref
Shure SM81	C	Condenser mic	—	—	5.6	—	Commercial	[238]
MEMS	P	MEMS mic	—	—	1.77	—	—	[238]
Stacked cellular polymer film	P	Stacked cellular polymer	—	—	2	—	—	[239]
AlN	P	Film	7.05 mm²	2.6–13.3k	1.67	—	—	[240]
P(VDF-TrFE) /$BaTiO_3$	P	Thermal drawn	80×80× 0.46 mm	0.8–1k	19.6	—	Acoustic sensing	[4]
PZT	P	Ceramic film	130 mm²	0.1–4k	52	92		[241]
PZT	P	Ceramic film	100 mm²	<240	~250	—	Acoustic sensing	[242]
Nb-doped PZT	P	Bulk microstructure	0.173 mm³	0.1–8k	30	94		[243]
PVDF	P	Film	799 mm²	1.4–4.9k	0.0253	—	—	[126]
AlN	P	Film	7.05 mm²	2.6–13.3k	1.67	—	—	[244]
PVDF-TrFE nanofibers	P	Electrospun nanofiber mat	1.8 cm²	0.2–5k	71	—	Acoustic sensing	[145]
PVDF-TrFE/ BTO NPs nanofibers	P	Electrospun nanofiber mat	7.5 cm² effective electrode area	<1500	1532.9	—	Direction prediction; sound recognition (attention-bas	[88]

Device / Material	Prin-ciple	Structure / Type	Size	Frequency (Hz)	Sensitivity (mV/Pa)	SNR (dB)	Notes	Ref
							ed model)	
PVDF film	P	MIM + cylinder-shape encapsulation	50 mm²	resonant	0.045	—	—	[8]
PVDF-nanoweb	P	MIM + substrate with through-hole	40 mm²	0.2 Hz–1 kHz	266 resonance frequency 8.9 1kHz	—	—	[245]
PTFE/graphite	T	Membrane	40 mm × 40 mm, t ≥0.35 mm	0.1–20k	3.2		Speech/voice tasks	[246]
PVDF/ZnO	T	Nanofiber membrane	100×35 mm	<200	3000	—	Acoustic sensing	[247]
SU-8	C	Micro structure	<9 mm³	0.015–10k	100	—	Voice recognition	[248]
PVDF-Trfe-CFE /BTO	P	MIM with alignment fiber	140 mm²	20–1000 Hz	75.6 <150Hz 36 150–1000Hz	>16	Bioacoustics sensing	Our work

P: piezoelectric; **T:** triboelectric; **C:** capacitive.

5.4 Conclusion

This chapter addresses structural refinement of the device, performance calibration, and tests on real physiological signals. Motivated by the limited bandwidth in the previous chapter and guided by theory and simulation, the effective stiffness of the thin-plate model was increased. A hard and soft composite ring clamping strategy was implemented: a high-modulus PC inner shoulder, a TPU outer ring for conformity and sealing, and a Cu upper ring that clamps the PI diaphragm from above and below, which markedly raises the equivalent boundary stiffness. Compared with elastic support, the improved device shows clearer boundary vibration, suppressed in-band ripples, and a frequency response extended to 1 kHz.

Sensitivity was reported under a unified calibration. At 150 Hz the low-frequency sensitivity reaches 76.6 mV/Pa. In the mid-to-high band, aside from the second resonance, the response is relatively flat with an average sensitivity of 36 mV/Pa. Consistent with the design expectation, the dynamic response within 50–90 dB follows an exponential law, with a relatively high SNR. Directivity measurements indicate an approximately omnidirectional yet asymmetric azimuthal pattern which informs array zoning and beamforming in future auscultation matrices.

In vivo recordings demonstrate stable pulse amplitudes with clear pulse-wave features. Heart sounds can be stably separated and analyzed, enabling extraction of the durations of the first and second heart sounds and the observation of S2 splitting. Lung-sound measurements on the back yield stable broadband energy with the main band at 100–

800 Hz. Overall, the proposed boundary structure and calibration workflow deliver high sensitivity, good linearity, and usable SNR in the target band, and they enable comprehensive validation on heart sounds, arterial pulses, and lung sounds under realistic conditions.

CHAPTER 6 CONCLUSION AND SUGGESTIONS FOR FUTURE WORK

6.1 Conclusions

This thesis presents a comprehensive study on the design, fabrication, optimization, and validation of flexible piezoelectric acoustic sensors for bioacoustics monitoring applications, addressing critical challenges in sensitivity, stability, mechanical compliance, and long-term wearability. Through the integration of material innovation, device architecture design, and theoretical modeling, a high-performance platform for continuous and reliable physiological sound monitoring has been successfully established.

The work began with the development of a low-density, anisotropic piezoelectric nanofiber membrane fabricated via electrospinning. By utilizing PVDF-TER as a flexible polymer matrix and incorporating BTO nanoparticles, the film achieved high β-phase crystallinity with an all-trans (*TTTT'*) phase content of ~92%. This high crystallinity, combined with the synergistic effects of BTO-induced heterogeneous nucleation and interfacial polarization, significantly enhanced the piezoelectric response. The nanofiber alignment and secondary stretching during fabrication further boosted the piezoelectric coefficients, achieving a d_{33} of -30.9 $pC \cdot N^{-1}$ and a remarkably high d_{31} of 45.5 $pC \cdot N^{-1}$. The porous structure of the electrospun membrane effectively lowered the apparent dielectric constant, allowing a simultaneously high g_{33}. Under low mechanical loading, the film exhibited a stable and linear voltage output, with strong

in-plane directional sensitivity, laying the foundation for its use as a core unit in acoustic sensing.

Building upon this optimized piezoelectric membrane, a flexible acoustic sensor with integrated AgNW-based electrodes was developed. The electrosprayed AgNW network formed a conformal, conductive, and mechanically stable interface with the fibrous substrate, maintaining stable conductivity even after 10,000 bending cycles. Compared with rigid metal electrodes deposited by sputtering, this flexible electrode design ensured excellent adhesion and fatigue resistance, enabling reliable signal transduction under dynamic deformation. Structural integration into a multilayer diaphragm-cavity architecture further enhanced acoustic impedance matching and low-frequency amplification. This design endowed the device with excellent conformability to curved skin surfaces and reliable signal stability. Acoustic characterization demonstrated a relatively flat sensitivity of ~47 $mV \cdot Pa^{-1}$ above 100 Hz, with effective dynamic response across 20–600 Hz, highlighting its potential in wearable stethoscopes and health-monitoring applications.

To address the limited bandwidth observed in the initial prototype, structural refinements were introduced by engineering the effective boundary stiffness of the vibrating membrane. A hybrid hard-soft clamping strategy-comprising a high-modulus PC inner shoulder, TPU outer sealing ring, and a Cu upper clamp-significantly increased the equivalent stiffness of the diaphragm edges. This optimization resulted in clearer boundary vibrations and an extended frequency response up to 1 kHz. Unified

acoustic calibration revealed a low-frequency sensitivity of 76.6 $mV \cdot Pa^{-1}$ at 150 Hz, while maintaining a relatively flat response in the mid-to-high band with an average sensitivity of 36 $mV \cdot Pa^{-1}$. The device demonstrated stable dynamic response over a 50–90 dB SPL range, with high SNR, and near-omnidirectional but slightly asymmetric directivity, making it valuable for future array-based beamforming applications.

The final validation stage involved in vivo monitoring of physiological signals under realistic conditions. Pulse recordings showed stable amplitude and clear pulse-wave morphologies, enabling the extraction of temporal parameters of arterial pulses. Heart sound monitoring demonstrated reliable detection and separation of S1 and S2, with the capability to observe physiological splitting of S2. Lung sound auscultation yielded broadband energy distributions, with dominant frequencies between 100–800 Hz, consistent with clinical standards. These results highlight the robustness, high fidelity, and practical applicability of the developed sensor system for continuous bioacoustics monitoring.

In summary, this thesis establishes a materials-to-system framework for the creation of wearable, high-performance piezoelectric acoustic sensors. By enhancing the piezoelectric response of PVDF terpolymer-based membranes, integrating durable and conformal AgNW electrodes, and optimizing the structural stiffness of the diaphragm-cavity architecture, the proposed devices achieve high sensitivity, wide bandwidth, mechanical robustness, and environmental stability. These advances not only validate the feasibility of real-time, long-term physiological signal acquisition but also pave the

way for future innovations in multi-modal wearable sensing platforms, intelligent health monitoring, and personalized diagnostic systems.

6.2 Limitations

Despite the significant advancements achieved in this work, several limitations remain that warrant further attention:

1. Influence of structural deformation.

   Although the sensor exhibits excellent skin conformity, its performance under complex curvature or micro-strain induced by body movements has not been systematically studied. Potential shifts in resonance modes or frequency response under bending and stretching may affect consistency in practical applications.

2. Signal reproducibility and validation.

   The sensing platform demonstrated stable in vivo detection of heart sounds, lung sounds, and pulse waves. However, large-scale testing with diverse subjects and repeated trials has not been performed, limiting the statistical robustness and generalizability of the results, especially under varying physiological and environmental conditions.

3. Bandwidth limitations.

   The hybrid clamping strategy effectively expanded the sensor bandwidth to 1 kHz, which is suitable for most low-frequency physiological signals. Nevertheless,

certain gastrointestinal sounds and higher-frequency components in biomedical acoustics extend beyond this range, and further structural optimization is needed to extend the operational frequency up to 2 kHz or higher.

4. Integration with advanced analytics

Although the sensor demonstrated high sensitivity and clear signal outputs, the current study did not integrate advanced signal processing or machine learning techniques for automated feature extraction and diagnostic analysis. This limits the immediate translation of the platform into intelligent, data-driven health monitoring systems.

6.3 Suggestions for Future Work

Building upon the achievements and limitations of this thesis, several directions are proposed to further refine the performance, reliability, and application scope of the developed flexible piezoelectric acoustic sensors for bioacoustics monitoring.

First, it is essential to conduct a systematic evaluation of long-term durability and environmental stability. This includes assessing the fatigue characteristics and creep behavior of the piezoelectric nanofiber membranes and flexible electrodes under repeated mechanical deformation, as well as examining sensor stability under varied humidity and temperature conditions. Such testing would provide critical insights into material degradation mechanisms and guide design improvements for real-world wearable applications.

Second, more in-depth studies should focus on the mechanical-acoustic interactions under curved surface conditions, which are highly relevant to skin-mounted wearable sensors. By developing a controlled setup to simulate the curvature of different body parts and employing laser Doppler vibrometer, the vibration modes of the sensor under soft-shell deformation can be precisely analyzed. This will help clarify how bending-induced micro-strains affect the resonant modes and frequency response, enabling more accurate structural optimization for stable signal performance across diverse anatomical locations.

Third, to improve clinical relevance and reproducibility, the repeatability and reliability of sensor output should be thoroughly evaluated. By stimulating the sensor with a library of standardized physiological acoustic signals and performing repeated measurements, the waveform consistency and signal features can be quantified. Coupled with machine learning-based feature extraction and classification, this approach could enhance diagnostic accuracy and enable intelligent bioacoustic monitoring systems.

Finally, further structural optimization should be explored to broaden the operational bandwidth of the sensor beyond 2 kHz, facilitating the precise detection and analysis of higher frequency bioacoustic signals, such as bowel sounds and other complex physiological events. Advanced finite element modeling and iterative prototyping could be employed to fine-tune the diaphragm–cavity design, balancing bandwidth expansion with mechanical compliance and wearability.

Collectively, these efforts will strengthen the robustness, versatility, and diagnostic capabilities of the developed sensors, paving the way toward their translation into next-generation wearable platforms for continuous, high-fidelity bioacoustics health monitoring.

References

1. Guo, H., et al., *A highly sensitive, self-powered triboelectric auditory sensor for social robotics and hearing aids.* Science robotics, 2018. **3**(20): p. eaat2516.

2. Weigold, J., et al. *A MEMS condenser microphone for consumer applications*. in *19th IEEE International Conference on Micro Electro Mechanical Systems*. 2006. IEEE.

3. Hu, H., et al., *A wearable cardiac ultrasound imager.* Nature, 2023. **613**(7945): p. 667-675.

4. Yan, W., et al., *Single fibre enables acoustic fabrics via nanometre-scale vibrations.* Nature, 2022. **603**(7902): p. 616-623.

5. Yin, R., et al., *Wearable sensors-enabled human–machine interaction systems: from design to application.* Advanced Functional Materials, 2021. **31**(11): p. 2008936.

6. Shi, J., et al., *Smart textile-integrated microelectronic systems for wearable applications.* Advanced materials, 2020. **32**(5): p. 1901958.

7. Song, E., et al., *Miniaturized electromechanical devices for the characterization of the biomechanics of deep tissue.* Nature Biomedical Engineering, 2021. **5**(7): p. 759-771.

8. Zhao, Y., et al., *Fully Flexible Electromagnetic Vibration Sensors with Annular Field Confinement Origami Magnetic Membranes.* Advanced Functional Materials, 2020. **30**(25): p. 2001553.

9. Yun, H.R., et al., *Ferrohydrodynamic energy harvesting based on air droplet movement.* Nano Energy, 2015. **11**: p. 171-178.

10. Farrar, J.T. and F.J. Ingelfinger, *Gastrointestinal motility as revealed by study of*

abdominal sounds. Gastroenterology, 1955. **29**(5): p. 789-802.

11. Watson, W. and E. Knox, *Phonoenterography: the recording and analysis of bowel sounds.* Gut, 1967. **8**(1): p. 88.

12. Dalle, D., et al., *Computer analysis of bowel sounds.* Computers in biology and medicine, 1975. **4**(3-4): p. 247-256.

13. Chan, D.K. and A. Hudspeth, *Ca2+ current–driven nonlinear amplification by the mammalian cochlea in vitro.* Nature neuroscience, 2005. **8**(2): p. 149-155.

14. voN BékésY, G., *Travelling waves as frequency analysers in the cochlea.* Nature, 1970. **225**(5239): p. 1207-1209.

15. Fu, H. and R.E. Cohen, *Polarization rotation mechanism for ultrahigh electromechanical response in single-crystal piezoelectrics.* Nature, 2000. **403**(6767): p. 281-283.

16. Zhi, C., et al., *Emerging Trends of Nanofibrous Piezoelectric and Triboelectric Applications: Mechanisms, Electroactive Materials, and Designed Architectures.* Advanced Materials, 2024. **36**(26): p. 2401264.

17. Meng, Y., et al., *Nano-fiber based self-powered flexible vibration sensor for rail fasteners tightness safety detection.* Nano Energy, 2022. **102**: p. 107667.

18. Amjadi, M., et al., *Stretchable, skin-mountable, and wearable strain sensors and their potential applications: a review.* Advanced Functional Materials, 2016. **26**(11): p. 1678-1698.

19. Lee, K., et al., *Carbon nanotube film piezoresistors embedded in polymer membranes.* Applied Physics Letters, 2010. **96**(1).

20. Zheng, Q., et al., *Graphene-based wearable piezoresistive physical sensors.* Materials Today, 2020. **36**: p. 158-179.

21. Miles, R.N., et al., *A MEMS low-noise sound pressure gradient microphone with capacitive sensing.* Journal of Microelectromechanical Systems, 2014. **24**(1): p. 241-248.

22. Chiang, C.-T. and Y.-C. Huang, *A semicylindrical capacitive sensor with interface circuit used for flow rate measurement.* IEEE Sensors Journal, 2006. **6**(6): p. 1564-1570.

23. Zawawi, S.A., et al., *A review of MEMS capacitive microphones.* Micromachines, 2020. **11**(5): p. 484.

24. Nicollini, G. and D. Devecchi, *MEMS capacitive microphones: Acoustical, electrical, and hidden thermal-related issues.* IEEE Sensors Journal, 2018. **18**(13): p. 5386-5394.

25. Sedaghat, S.B. and B.A. Ganji, *A novel MEMS capacitive microphone using spring-type diaphragm.* Microsystem Technologies, 2019. **25**: p. 217-224.

26. Kubba, A.E., et al., *A micro-capacitive pressure sensor design and modelling.* Journal of Sensors and Sensor Systems, 2016. **5**(1): p. 95-112.

27. Pei, G., *A micro capacitive pressure sensor with two deformable electrodes: design, optimization and fabrication*. 2006, Ph. D. dissertation, Department of electrical and coputer engineering ….

28. Lipomi, D.J., et al., *Skin-like pressure and strain sensors based on transparent elastic films of carbon nanotubes.* Nature nanotechnology, 2011. **6**(12): p. 788-792.

29. Smith, A.T., et al., *Synthesis, properties, and applications of graphene oxide/reduced graphene oxide and their nanocomposites.* Nano Materials Science, 2019. **1**(1): p. 31-47.

30. Kim, J., et al., *Soft wearable pressure sensors for beat-to-beat blood pressure*

monitoring. Advanced healthcare materials, 2019. **8**(13): p. 1900109.

31. Zhang, Y., et al., *Ultrafast piezocapacitive soft pressure sensors with over 10 kHz bandwidth via bonded microstructured interfaces.* Nature Communications, 2024. **15**(1): p. 3048.

32. Ha, K.-H., et al., *Soft capacitive pressure sensors: trends, challenges, and perspectives.* ACS nano, 2022. **16**(3): p. 3442-3448.

33. Yoon, S.G. and S.T. Chang, *Microfluidic capacitive sensors with ionic liquid electrodes and CNT/PDMS nanocomposites for simultaneous sensing of pressure and temperature.* Journal of Materials Chemistry C, 2017. **5**(8): p. 1910-1919.

34. Mu, C., et al., *Enhanced piezocapacitive effect in CaCu3Ti4O12–polydimethylsiloxane composited sponge for ultrasensitive flexible capacitive sensor.* ACS Applied Nano Materials, 2017. **1**(1): p. 274-283.

35. Lai, P.-C. and S.-S. Yu, *Cationic cellulose nanocrystals-based nanocomposite hydrogels: Achieving 3D printable capacitive sensors with high transparency and mechanical strength.* Polymers, 2021. **13**(5): p. 688.

36. Wang, M., et al., *Ionogel microphones detect underwater sound with directivity and exceptional stability.* ACS Applied Electronic Materials, 2020. **2**(5): p. 1295-1303.

37. Noman, M.T., et al., *Aerogels for biomedical, energy and sensing applications.* Gels, 2021. **7**(4): p. 264.

38. Kwon, D., et al. *Porous dielectric elastomer based ultra-sensitive capacitive pressure sensor and its application to wearable sensing device*. in *2015 Transducers-2015 18th International Conference on Solid-State Sensors, Actuators and Microsystems (TRANSDUCERS)*. 2015. IEEE.

39. Fan, F.-R., Z.-Q. Tian, and Z.L. Wang, *Flexible triboelectric generator.* Nano energy, 2012. **1**(2): p. 328-334.

40. Zhao, Z., et al., *Selection rules of triboelectric materials for direct-current triboelectric nanogenerator.* Nature communications, 2021. **12**(1): p. 4686.

41. Guan, Q., et al., *Highly efficient self-healable and dual responsive hydrogel-based deformable triboelectric nanogenerators for wearable electronics.* Journal of Materials Chemistry A, 2019. **7**(23): p. 13948-13955.

42. Chen, J. and Z.L. Wang, *Reviving vibration energy harvesting and self-powered sensing by a triboelectric nanogenerator.* Joule, 2017. **1**(3): p. 480-521.

43. Wang, S., L. Lin, and Z.L. Wang, *Triboelectric nanogenerators as self-powered active sensors.* Nano Energy, 2015. **11**: p. 436-462.

44. Zhang, D., et al., *Oriented Proton-Conductive Nanochannels Boosting a Highly Conductive Proton-Exchange Membrane for a Vanadium Redox Flow Battery.* ACS Applied Materials & Interfaces, 2021. **13**(3): p. 4051-4061.

45. Wu, X., et al., *A single-mode, self-adapting, and self-powered mechanoreceptor based on a potentiometric–triboelectric hybridized sensing mechanism for resolving complex stimuli.* Advanced Materials, 2020. **32**(50): p. 2005970.

46. Ahmed, A., et al., *Integrated triboelectric nanogenerators in the era of the internet of things.* Advanced Science, 2019. **6**(24): p. 1802230.

47. Ding, W., et al., *Human–machine interfacing enabled by triboelectric nanogenerators and tribotronics.* Advanced Materials Technologies, 2019. **4**(1): p. 1800487.

48. Wu, C., et al., *Triboelectric nanogenerator: a foundation of the energy for the new era.* Advanced Energy Materials, 2019. **9**(1): p. 1802906.

49. Li, Z., et al., *Multilayered fiber-based triboelectric nanogenerator with high performance for biomechanical energy harvesting.* Nano Energy, 2018. **53**: p. 726-733.

50. Bai, P., et al., *Integrated multilayered triboelectric nanogenerator for harvesting biomechanical energy from human motions.* ACS nano, 2013. **7**(4): p. 3713-3719.

51. Yang, J., et al., *Broadband vibrational energy harvesting based on a triboelectric nanogenerator.* Advanced Energy Materials, 2014. **4**(6): p. 1301322.

52. Wang, Z.L., T. Jiang, and L. Xu, *Toward the blue energy dream by triboelectric nanogenerator networks.* Nano energy, 2017. **39**: p. 9-23.

53. Guo, R., et al., *A Voiceprint Recognition Sensor Based on a Fully 3D-Printed Triboelectric Nanogenerator via a One-Step Molding Route.* Advanced Engineering Materials, 2020. **22**(5): p. 1901560.

54. Cui, M., et al., *Template-assisted electrospun ordered hierarchical microhump arrays-based multifunctional triboelectric nanogenerator for tactile sensing and animal voice-emotion identification.* Advanced Functional Materials, 2023. **33**(46): p. 2301589.

55. Luo, H., et al., *Human–machine interaction via dual modes of voice and gesture enabled by triboelectric nanogenerator and machine learning.* ACS Applied Materials & Interfaces, 2023. **15**(13): p. 17009-17018.

56. Li, Y., Y. Huang, and N. Zhao, *Low-intensity sensitive and high stability flexible heart sound sensor enabled by hybrid near-field/far-field electrospinning.* Advanced Functional Materials, 2023. **33**(29): p. 2300666.

57. He, D., et al., *Physically doped and printed elastomer films as flexible high-*

performance triboelectric nanogenerator for self-powered mechanoelectric sensor for recovering voice and monitoring heart rate. Chemical Engineering Journal, 2023. **456**: p. 141012.

58. Kang, D.h., et al., *A Self-Powered, Highly Sensitive, and Frequency-Tunable Triboelectric Acoustic Sensor Inspired by the Human Cochlea.* Advanced Functional Materials, 2024. **34**(48): p. 2408344.

59. Yang, H., et al., *High-sensitive and ultra-wide spectrum multifunctional triboelectric acoustic sensor for broad scenario applications.* Nano Energy, 2022. **104**: p. 107932.

60. Hui, X., et al., *Acoustically enhanced triboelectric stethoscope for ultrasensitive cardiac sounds sensing and disease diagnosis.* Advanced Materials, 2024. **36**(29): p. 2401508.

61. Nayeem, M.O.G., et al., *All-nanofiber–based, ultrasensitive, gas-permeable mechanoacoustic sensors for continuous long-term heart monitoring.* Proceedings of the National Academy of Sciences, 2020. **117**(13): p. 7063-7070.

62. Park, J., et al., *Frequency-selective acoustic and haptic smart skin for dual-mode dynamic/static human-machine interface.* Science advances, 2022. **8**(12): p. eabj9220.

63. Zheng, J., et al., *Acoustic core–shell resonance harvester for application of artificial cochlea based on the piezo-triboelectric effect.* ACS nano, 2021. **15**(11): p. 17499-17507.

64. Shamos, M.H., L.S. Lavine, and M.I. Shamos, *Piezoelectric effect in bone.* Nature, 1963. **197**(4862): p. 81-81.

65. Jaffe, B., W.R. Cook, and H. Jaffe, *The piezoelectric effect in ceramics.* Piezoelectric ceramics, 1971: p. 7-21.

66. Damjanovic, D., *Stress and frequency dependence of the direct piezoelectric effect in ferroelectric ceramics.* Journal of Applied Physics, 1997. **82**(4): p. 1788-1797.

67. Lewis, T. *The piezoelectric effect*. in *CEIDP'05. 2005 Annual Report Conference on Electrical Insulation and Dielectric Phenomena, 2005.* 2005. IEEE.

68. Athenstaedt, H., *Pyroelectric and piezoelectric properties of vertebrates.* Annals of the New York Academy of Sciences, 1974. **238**(1): p. 68-94.

69. Aschero, G., et al., *Converse piezoelectric effect detected in fresh cow femur bone.* Journal of biomechanics, 1996. **29**(9): p. 1169-1174.

70. Mazzalai, A., et al., *Characterization and fatigue of the converse piezoelectric effect in PZT films for MEMS applications.* Journal of Microelectromechanical systems, 2014. **24**(4): p. 831-838.

71. Yamagata, Y., et al. *A micro mobile mechanism using thermal expansion and its theoretical analysis. A comparison with impact drive mechanism using piezoelectric elements*. in *Proceedings IEEE Micro Electro Mechanical Systems An Investigation of Micro Structures, Sensors, Actuators, Machines and Robotic Systems*. 1994. IEEE.

72. Dagdeviren, C., et al., *Conformable amplified lead zirconate titanate sensors with enhanced piezoelectric response for cutaneous pressure monitoring.* Nature communications, 2014. **5**(1): p. 4496.

73. Xiang, Z., et al., *High-performance microcone-array flexible piezoelectric acoustic sensor based on multicomponent lead-free perovskite rods.* Matter, 2023. **6**(2): p. 554-569.

74. Cao, X., et al., *Piezoelectric nanogenerators derived self-powered sensors for*

multifunctional applications and artificial intelligence. Advanced Functional Materials, 2021. **31**(33): p. 2102983.

75. Smits, J.G., S.I. Dalke, and T.K. Cooney, *The constituent equations of piezoelectric bimorphs.* Sensors and actuators A: Physical, 1991. **28**(1): p. 41-61.

76. Jung, Y.H., et al., *Flexible piezoelectric acoustic sensors and machine learning for speech processing.* Advanced Materials, 2020. **32**(35): p. 1904020.

77. Wang, S., et al., *Flexible piezoelectric fibers for acoustic sensing and positioning.* Advanced electronic materials, 2017. **3**(3): p. 1600449.

78. Nguyen, V., R. Zhu, and R. Yang, *Environmental effects on nanogenerators.* Nano Energy, 2015. **14**: p. 49-61.

79. Wang, Z., et al., *Voltage generation from individual BaTiO3 nanowires under periodic tensile mechanical load.* Nano letters, 2007. **7**(10): p. 2966-2969.

80. Kim, S.-B., et al., *Comparison of MEMS PZT cantilevers based on $ d_ {31} $ and $ d_ {33} $ modes for vibration energy harvesting.* Journal of microelectromechanical systems, 2012. **22**(1): p. 26-33.

81. Hwang, G.T., et al., *Nanogenerators: Self-Powered Cardiac Pacemaker Enabled by Flexible Single Crystalline PMN-PT Piezoelectric Energy Harvester (Adv. Mater. 28/2014).* Advanced Materials, 2014. **26**(28): p. 4754-4754.

82. Roscow, J.I., et al., *Modified energy harvesting figures of merit for stress-and strain-driven piezoelectric systems.* The European Physical Journal Special Topics, 2019. **228**: p. 1537-1554.

83. Chocat, N., et al., *Piezoelectric fibers for conformal acoustics.* Advanced materials, 2012. **24**(39): p. 5327.

84. Yao, D., et al., *Achieving the upper bound of piezoelectric response in tunable, wearable 3D printed nanocomposites.* Advanced Functional Materials, 2019. **29**(42): p. 1903866.

85. Kiat, J.-M., et al., *Monoclinic structure of unpoled morphotropic high piezoelectric PMN-PT and PZN-PT compounds.* Physical Review B, 2002. **65**(6): p. 064106.

86. Yamashita, Y., et al., *A review of lead perovskite piezoelectric single crystals and their medical transducers application.* IEEE Transactions on Ultrasonics, Ferroelectrics, and Frequency Control, 2022. **69**(11): p. 3048-3056.

87. Chi, C., et al., *Selectively tuning ionic thermopower in all-solid-state flexible polymer composites for thermal sensing.* Nature Communications, 2022. **13**(1): p. 221.

88. Chang, J., et al., *Piezoelectric nanofiber–based intelligent hearing system.* Science Advances, 2025. **11**(19): p. eadl2741.

89. Chen, X., et al., *Relaxor ferroelectric polymer exhibits ultrahigh electromechanical coupling at low electric field.* Science, 2022. **375**(6587): p. 1418-1422.

90. Zhai, Y., et al., *Sandwich-structured PVdF/PMIA/PVdF nanofibrous separators with robust mechanical strength and thermal stability for lithium ion batteries.* Journal of Materials Chemistry A, 2014. **2**(35): p. 14511-14518.

91. Yang, T., et al., *Hierarchically structured PVDF/ZnO core-shell nanofibers for self-powered physiological monitoring electronics.* Nano Energy, 2020. **72**: p. 104706.

92. Abbasipour, M., et al., *The piezoelectric response of electrospun PVDF nanofibers with graphene oxide, graphene, and halloysite nanofillers: a*

comparative study. Journal of Materials Science: Materials in Electronics, 2017. **28**: p. 15942-15952.

93. Kim, H., et al., *3D printing of BaTiO3/PVDF composites with electric in situ poling for pressure sensor applications.* Macromolecular Materials and Engineering, 2017. **302**(11): p. 1700229.

94. Han, L., et al., *Health monitoring via heart, breath, and Korotkoff sounds by wearable Piezoelectret patches.* Advanced Science, 2023. **10**(28): p. 2301180.

95. Gong, Y., et al., *Advances in Piezoelectret Materials-Based Bidirectional Haptic Communication Devices.* Advanced Materials, 2024. **36**(33): p. 2405308.

96. Jaffe, H., *Piezoelectric ceramics.* Journal of the American Ceramic Society, 1958. **41**(11): p. 494-498.

97. Shrout, T.R. and S.J. Zhang, *Lead-free piezoelectric ceramics: Alternatives for PZT?* Journal of Electroceramics, 2007. **19**: p. 113-126.

98. Tressler, J.F., S. Alkoy, and R.E. Newnham, *Piezoelectric sensors and sensor materials.* Journal of electroceramics, 1998. **2**: p. 257-272.

99. Karaki, T., et al., *Lead-free piezoelectric ceramics with large dielectric and piezoelectric constants manufactured from BaTiO3 nano-powder.* Japanese Journal of Applied Physics, 2007. **46**(2L): p. L97.

100. Acosta, M., et al., *BaTiO3-based piezoelectrics: Fundamentals, current status, and perspectives.* Applied Physics Reviews, 2017. **4**(4).

101. Akdogan, E.K., M. Allahverdi, and A. Safari, *Piezoelectric composites for sensor and actuator applications.* IEEE transactions on ultrasonics, ferroelectrics, and frequency control, 2005. **52**(5): p. 746-775.

102. Allil, R.C. and M.M. Werneck, *Optical high-voltage sensor based on fiber*

Bragg grating and PZT piezoelectric ceramics. IEEE Transactions on instrumentation and measurement, 2011. **60**(6): p. 2118-2125.

103. Lous, G.M., et al., *Fabrication of piezoelectric ceramic/polymer composite transducers using fused deposition of ceramics.* Journal of the American Ceramic Society, 2000. **83**(1): p. 124-28.

104. Zhong, J. and B. Yao, *Adaptive robust precision motion control of a piezoelectric positioning stage.* IEEE Transactions on Control Systems Technology, 2008. **16**(5): p. 1039-1046.

105. Mohith, S., et al., *Recent trends in piezoelectric actuators for precision motion and their applications: A review.* Smart Materials and Structures, 2020. **30**(1): p. 013002.

106. Chu, B., et al., *A dielectric polymer with high electric energy density and fast discharge speed.* Science, 2006. **313**(5785): p. 334-336.

107. Takenaka, T., et al., *Lead-free piezoelectric ceramics based on perovskite structures.* Journal of Electroceramics, 2007. **19**: p. 259-265.

108. Hao, J., et al., *Progress in high-strain perovskite piezoelectric ceramics.* Materials Science and Engineering: R: Reports, 2019. **135**: p. 1-57.

109. Ma, N., et al., *Phase structure and nano-domain in high performance of BaTiO3 piezoelectric ceramics.* Journal of the European Ceramic Society, 2012. **32**(5): p. 1059-1066.

110. Nagata, H., et al., *Large piezoelectric constant and high Curie temperature of lead-free piezoelectric ceramic ternary system based on bismuth sodium titanate-bismuth potassium titanate-barium titanate near the morphotropic phase boundary.* Japanese journal of applied physics, 2003. **42**(12R): p. 7401.

111. Hiruma, Y., et al., *Piezoelectric properties of BaTiO3–(Bi1/2K1/2) TiO3*

ferroelectric ceramics. Japanese journal of applied physics, 2004. **43**(11R): p. 7556.

112. Broadhurst, M. and G. Davis, *Physical basis for piezoelectricity in PVDF.* Ferroelectrics, 1984. **60**(1): p. 3-13.

113. Vinogradov, A.M., et al., *Damping and electromechanical energy losses in the piezoelectric polymer PVDF.* Mechanics of Materials, 2004. **36**(10): p. 1007-1016.

114. Li, L., et al., *Studies on the transformation process of PVDF from α to β phase by stretching.* Rsc Advances, 2014. **4**(8): p. 3938-3943.

115. Mohammadi, B., A.A. Yousefi, and S.M. Bellah, *Effect of tensile strain rate and elongation on crystalline structure and piezoelectric properties of PVDF thin films.* Polymer testing, 2007. **26**(1): p. 42-50.

116. Tarbuttona, J., et al., *Phase transformation and shock sensor response of additively manufactured piezoelectric PVDF.* Procedia Manufacturing, 2017. **10**: p. 982-989.

117. Sharma, T., et al., *Patterning piezoelectric thin film PVDF–TrFE based pressure sensor for catheter application.* Sensors and Actuators A: physical, 2012. **177**: p. 87-92.

118. Bhavanasi, V., et al., *Enhanced piezoelectric energy harvesting performance of flexible PVDF-TrFE bilayer films with graphene oxide.* ACS applied materials & interfaces, 2016. **8**(1): p. 521-529.

119. Huang, Y.-F., et al., *A relaxor ferroelectric polymer with an ultrahigh dielectric constant largely promotes the dissociation of lithium salts to achieve high ionic conductivity.* Energy & Environmental Science, 2021. **14**(11): p. 6021-6029.

120. Wang, Z.-X. and W.-Q. Liao, *Giant electromechanical effects in polymers.*

Science, 2022. **375**(6587): p. 1353-1354.

121. Li, Y., et al., *Multilayer assembly of electrospun/electrosprayed PVDF-based nanofibers and beads with enhanced piezoelectricity and high sensitivity.* Chemical Engineering Journal, 2020. **388**: p. 124205.

122. Ramadan, K.S., D. Sameoto, and S. Evoy, *A review of piezoelectric polymers as functional materials for electromechanical transducers.* Smart Materials and Structures, 2014. **23**(3): p. 033001.

123. Liu, Y., et al., *Ferroelectric polymers exhibiting behaviour reminiscent of a morphotropic phase boundary.* Nature, 2018. **562**(7725): p. 96-100.

124. Xia, F., et al., *High electromechanical responses in a poly (vinylidene fluoride–trifluoroethylene–chlorofluoroethylene) terpolymer.* Advanced materials, 2002. **14**(21): p. 1574-1577.

125. Habib, M., et al., *Enhancement of Piezoelectricity by Novel Poling Method of the Rare-Earth Modified BiFeO3–BaTiO3 Lead-Free Ceramics.* Advanced Electronic Materials, 2023. **9**(5): p. 2201210.

126. Shintaku, H., et al., *Development of piezoelectric acoustic sensor with frequency selectivity for artificial cochlea.* Sensors and Actuators A: Physical, 2010. **158**(2): p. 183-192.

127. Park, S., et al., *PVDF-based piezoelectric microphone for sound detection inside the cochlea: toward totally implantable cochlear implants.* Trends in hearing, 2018. **22**: p. 2331216518774450.

128. Lee, H.S., et al., *Flexible inorganic piezoelectric acoustic nanosensors for biomimetic artificial hair cells.* Advanced Functional Materials, 2014. **24**(44): p. 6914-6921.

129. Coté, G.L., R.M. Lec, and M.V. Pishko, *Emerging biomedical sensing*

technologies and their applications. IEEE sensors journal, 2003. **3**(3): p. 251-266.

130. Basaeri, H., D.B. Christensen, and S. Roundy, *A review of acoustic power transfer for bio-medical implants.* Smart Materials and Structures, 2016. **25**(12): p. 123001.

131. Li, S.-H., et al., *Design of wearable breathing sound monitoring system for real-time wheeze detection.* Sensors, 2017. **17**(1): p. 171.

132. Shih, C.-H., et al., *Breeze: Smartphone-based acoustic real-time detection of breathing phases for a gamified biofeedback breathing training.* Proceedings of the ACM on interactive, mobile, wearable and ubiquitous technologies, 2019. **3**(4): p. 1-30.

133. Qu, M., et al., *Monitoring of physiological sounds with wearable device based on piezoelectric MEMS acoustic sensor.* Journal of Micromechanics and Microengineering, 2021. **32**(1): p. 014001.

134. Chauhan, J., et al. *BreathPrint: Breathing acoustics-based user authentication*. in *Proceedings of the 15th Annual International Conference on Mobile Systems, Applications, and Services*. 2017.

135. Monson, B.B., et al., *The perceptual significance of high-frequency energy in the human voice.* Frontiers in psychology, 2014. **5**: p. 587.

136. Lukáš, D., et al., *Physical principles of electrospinning (electrospinning as a nano-scale technology of the twenty-first century).* Textile progress, 2009. **41**(2): p. 59-140.

137. Mohammadzadehmoghadam, S., et al., *Electrospinning: Current status and future trends.* Nano-Size Polymers: Preparation, Properties, Applications, 2016: p. 89-154.

138. Park, J.-S., *Electrospinning and its applications.* Advances in Natural Sciences: Nanoscience and Nanotechnology, 2010. **1**(4): p. 043002.

139. Rutledge, G.C. and S.V. Fridrikh, *Formation of fibers by electrospinning.* Advanced drug delivery reviews, 2007. **59**(14): p. 1384-1391.

140. Li, D. and Y. Xia, *Electrospinning of nanofibers: reinventing the wheel?* Advanced materials, 2004. **16**(14): p. 1151-1170.

141. Tian, Z., et al., *Underwater Self-Powered All-Optical Wireless Ultrasonic Sensing, Positioning and Communication with Ultrafast Response Time and Ultrahigh Sensitivity.* Advanced Optical Materials, 2022. **10**(5): p. 2102091.

142. Wu, Y., et al., *Biomimetic Heteromodulus All-Fluoropolymer Piezoelectric Nanofiber Mats for Highly Sensitive Acoustic Detection.* ACS Applied Materials & Interfaces, 2025. **17**(14): p. 21808-21818.

143. Chen, X., et al., *PZT Nanoactive Fiber Composites for Acoustic Emission Detection.* Advanced Materials, 2011. **23**(34): p. 3965-3969.

144. Jiang, Y., et al., *Ultrathin Eardrum-Inspired Self-Powered Acoustic Sensor for Vocal Synchronization Recognition with the Assistance of Machine Learning.* Small, 2022. **18**(13): p. 2106960.

145. Wang, W., et al., *Broad Bandwidth, Self-Powered Acoustic Sensor Created by Dynamic Near-Field Electrospinning of Suspended, Transparent Piezoelectric Nanofiber Mesh.* Small, 2020. **16**(28): p. 2000581.

146. Lang, C., et al., *High-sensitivity acoustic sensors from nanofibre webs.* Nature Communications, 2016. **7**(1): p. 11108.

147. Yang, T., et al., *Moth-inspired isolated venation network nanofiber-based multi-resonant acoustic sensor for enhanced broadband perception.* Chemical Engineering Journal, 2025. **521**: p. 166250.

148. Zhen, L., et al., *Flexible inorganic piezoelectric functional films and their applications.* Journal of Advanced Ceramics, 2023. **12**(3): p. 433-462.

149. Xia, G., B. Song, and J. Fang, *Electrical Stimulation Enabled via Electrospun Piezoelectric Polymeric Nanofibers for Tissue Regeneration.* Research. **2022**.

150. Shao, H., et al., *Electrosprayed boron nitride nanosheet aggregates for enhanced acoustic energy harvesting with poly(vinylidene fluoride) nanofiber membranes.* Nano Energy, 2024. **121**: p. 109195.

151. Joshi, B., et al., *Supersonically sprayed PVDF and ZnO flowers with built-in nanocuboids for wearable piezoelectric nanogenerators.* Nano Energy, 2023. **112**: p. 108447.

152. Su, C., et al., *Robust superhydrophobic wearable piezoelectric nanogenerators for self-powered body motion sensors.* Nano Energy, 2023. **107**: p. 108095.

153. Jakobsen, L., S. Brinkløv, and A. Surlykke, *Intensity and directionality of bat echolocation signals.* Frontiers in physiology, 2013. **4**: p. 89.

154. Corcoran, A.J. and C.F. Moss, *Sensing in a noisy world: lessons from auditory specialists, echolocating bats.* Journal of Experimental Biology, 2017. **220**(24): p. 4554-4566.

155. Yanagisawa, R., et al., *Wearable vibration sensor for measuring the wing flapping of insects.* Sensors, 2021. **21**(2): p. 593.

156. Du, X., et al., *Bowel sounds identification and migrating motor complex detection with low-cost piezoelectric acoustic sensing device.* Sensors, 2018. **18**(12): p. 4240.

157. Dang, T.B., et al., *Flexible, wearable mechano-acoustic sensors for body sound monitoring applications.* Nanoscale, 2025.

158. Horne, J.K., *Acoustic approaches to remote species identification: a review.* Fisheries oceanography, 2000. **9**(4): p. 356-371.

159. Su, L., et al., *Self-powered visualized tactile-acoustic sensor for accurate artificial perception with high brightness and record-low detection limit.* Science Advances, 2024. **10**(44): p. eadq8989.

160. Zhou, Q., et al., *Piezoelectric single crystal ultrasonic transducers for biomedical applications.* Progress in materials science, 2014. **66**: p. 87-111.

161. Rathod, V.T., *A review of acoustic impedance matching techniques for piezoelectric sensors and transducers.* Sensors, 2020. **20**(14): p. 4051.

162. Chung, H.U., et al., *Skin-interfaced biosensors for advanced wireless physiological monitoring in neonatal and pediatric intensive-care units.* Nature medicine, 2020. **26**(3): p. 418-429.

163. Yoo, J.-Y., et al., *Wireless broadband acousto-mechanical sensing system for continuous physiological monitoring.* Nature Medicine, 2023. **29**(12): p. 3137-3148.

164. Park, J., et al., *Fingertip skin–inspired microstructured ferroelectric skins discriminate static/dynamic pressure and temperature stimuli.* Science advances, 2015. **1**(9): p. e1500661.

165. Ward, J.J. and B.A. Wattier, *Technology for enhancing chest auscultation in clinical simulation.* Respiratory care, 2011. **56**(6): p. 834-845.

166. Luo, Y., et al., *Technology Roadmap for Flexible Sensors.* ACS Nano, 2023. **17**(6): p. 5211-5295.

167. Zhao, C., et al., *Ionic Flexible Sensors: Mechanisms, Materials, Structures, and Applications.* Advanced Functional Materials, 2022. **32**(17): p. 2110417.

168. Lee, J.-H., K. Cho, and J.-K. Kim, *Age of Flexible Electronics: Emerging Trends in Soft Multifunctional Sensors.* Advanced Materials, 2024. **36**(16): p. 2310505.

169. Niu, H., et al., *Advances in flexible sensors for intelligent perception system enhanced by artificial intelligence.* InfoMat, 2023. **5**(5): p. e12412.

170. Pyo, S., et al., *Recent Progress in Flexible Tactile Sensors for Human-Interactive Systems: From Sensors to Advanced Applications.* Advanced Materials, 2021. **33**(47): p. 2005902.

171. Liu, T., et al., *Emerging Wearable Acoustic Sensing Technologies.* Advanced Science, 2025. **12**(6): p. 2408653.

172. Ghazali, M.F., et al., *State-of-The-Art application and challenges of optical fibre distributed acoustic sensing in civil engineering.* Optical Fiber Technology, 2024. **87**: p. 103911.

173. Rahman, M.A., et al., *A review of distributed acoustic sensing applications for railroad condition monitoring.* Mechanical Systems and Signal Processing, 2024. **208**: p. 110983.

174. Lin, Z., et al., *Insights into Materials, Physics, and Applications in Flexible and Wearable Acoustic Sensing Technology.* Advanced Materials, 2024. **36**(9): p. 2306880.

175. Liu, T., et al., *Machine learning-assisted wearable sensing systems for speech recognition and interaction.* Nature Communications, 2025. **16**(1): p. 2363.

176. Wang, Y., C. Sun, and D. Ahmed, *A smart acoustic textile for health monitoring.* Nature Electronics, 2025. **8**(6): p. 485-495.

177. Jung, Y.H., et al., *Theoretical Basis of Biomimetic Flexible Piezoelectric Acoustic Sensors for Future Customized Auditory Systems.* Advanced Functional Materials, 2024. **34**(10): p. 2309316.

178. Liu, Y.-X., et al., *Multi-Length Engineering of (K, Na)NbO3 Films for Lead-Free Piezoelectric Acoustic Sensors with High Sensitivity.* Advanced Functional Materials, 2024. **34**(12): p. 2312699.

179. Sasikumar, R., et al., *Microcrack-assisted piezoelectric acoustic sensor based on f-MWCNTs/BaTiO3@PDMS nanocomposite and its self-powered voice recognition applications.* Chemical Engineering Journal, 2024. **479**: p. 147297.

180. Gaudio, A., et al., *Diaphragm Design for an Electret Microphone Stethoscope.* IEEE Sensors Journal, 2025. **25**(14): p. 26711-26722.

181. Han, L., et al., *Stretchable piezoelectret electronic stethoscope for phonocardiography and lung sound detection in motion and noise conditions.* Applied Materials Today, 2024. **36**: p. 102077.

182. Parlato, S., et al. *A Flexible PVDF Sensor for Forcecardiography*. Sensors, 2025. **25**, DOI: 10.3390/s25051608.

183. Andrey, V., et al., *Piezoelectric PVDF and its copolymers in biomedicine: innovations and applications.* Biomaterials Science, 2024. **12**(20): p. 5164-5185.

184. Riwa, I.O., et al., *Advances in copolymers based on polyvinylidene fluoride (PVDF) and their composites for piezoelectric energy harvesting.* Resources Chemicals and Materials, 2025: p. 100124.

185. Peng, R., et al., *Enhanced Piezoelectric Energy Harvester by Employing Freestanding Single-Crystal BaTiO3 Films in PVDF-TrFE Based Composites.* Advanced Functional Materials, 2024. **34**(27): p. 2316519.

186. Ao, Y., et al., *Dual Structure Reinforces Interfacial Polarized MXene/PVDF-TrFE Piezoelectric Nanocomposite for Pressure Monitoring.* Nano-Micro Letters, 2025. **17**(1): p. 320.

187. Persano, L., et al., *Advanced Materials for Energy Harvesting and Soft Robotics:*

Emerging Frontiers to Enhance Piezoelectric Performance and Functionality. Advanced Materials, 2024. **36**(45): p. 2405363.

188. Emanov, D.P., et al. *Measuring Hydrostatic Piezoelectric Voltage Coefficient of PVDF Films for Biomedical Applications*. in *2025 7th International Youth Conference on Radio Electronics, Electrical and Power Engineering (REEPE)*. 2025.

189. Zhou, X., et al., *All 3D-printed stretchable piezoelectric nanogenerator with non-protruding kirigami structure.* Nano Energy, 2020. **72**: p. 104676.

190. Mirjalali, S., et al., *Enhanced Piezoelectricity of PVDF-TrFE Nanofibers by Intercalating with Electrosprayed BaTiO3.* ACS Applied Materials & Interfaces, 2023. **15**(35): p. 41806-41816.

191. Cho, Y., et al., *BaTiO3@PVDF-TrFE nanocomposites with efficient orientation prepared via phase separation nano-coating method for piezoelectric performance improvement and application to 3D-PENG.* Chemical Engineering Journal, 2022. **427**: p. 131030.

192. Wang, P., et al., *A flexible magneto-electric sensor with enhanced performance through flower-shaped BTO fillers in P(VDF-TrFE) matrix.* Sensors and Actuators A: Physical, 2024. **373**: p. 115426.

193. Kim, K., et al., *Highly Transparent and Flexible All-Nanofiber-Based Piezocomposite Containing BaTiO3-Embedded P(VDF-TrFE) Nanofibers for Harvesting and Monitoring Human Kinetic Movements.* Advanced Fiber Materials, 2024. **6**(5): p. 1369-1386.

194. Hong, C.-C., et al., *Enhanced Piezoelectricity of Nanoimprinted Sub-20 nm Poly(vinylidene fluoride–trifluoroethylene) Copolymer Nanograss.* Macromolecules, 2012. **45**(3): p. 1580-1586.

195. Yang, J.H., et al., *Shear stress-induced enhancement of the piezoelectric properties of PVDF-TrFE thin films.* Organic Electronics, 2016. **28**: p. 67-72.

196. Maturi, M., et al., *3D-Printing of Highly Piezoelectric Barium Titanate Polymer Nanocomposites with Surface-Modified Nanoparticles at Low Loadings.* Advanced Functional Materials, 2025. **35**(1): p. 2407077.

197. Zhou, Z., H. Tang, and H.A. Sodano, *Vertically Aligned Arrays of BaTiO3 Nanowires.* ACS Applied Materials & Interfaces, 2013. **5**(22): p. 11894-11899.

198. Senan, E.M., et al., *Early diagnosis of brain tumour mri images using hybrid techniques between deep and machine learning.* Computational and mathematical methods in medicine, 2022. **2022**(1): p. 8330833.

199. Hunter, B., S. Hindocha, and R.W. Lee, *The role of artificial intelligence in early cancer diagnosis.* Cancers, 2022. **14**(6): p. 1524.

200. Welch, D., et al., *Health effects of transport noise.* Transport Reviews, 2023. **43**(6): p. 1190-1210.

201. Yao, H., et al., *Intelligent sound monitoring and identification system combining triboelectric nanogenerator-based self-powered sensor with deep learning technique.* Advanced functional materials, 2022. **32**(15): p. 2112155.

202. Zhang, X., et al., *Acoustoelectric materials & devices in biomedicine.* Chemical Engineering Journal, 2024. **483**: p. 149314.

203. Gao, W., et al., *Fully integrated wearable sensor arrays for multiplexed in situ perspiration analysis.* Nature, 2016. **529**(7587): p. 509-514.

204. Jiang, Z. and S. Choi, *A cardiac sound characteristic waveform method for in-home heart disorder monitoring with electric stethoscope.* Expert Systems with Applications, 2006. **31**(2): p. 286-298.

205. Seah, J.J., et al., *Review on the advancements of stethoscope types in chest auscultation.* Diagnostics, 2023. **13**(9): p. 1545.

206. Leng, S., et al., *The electronic stethoscope.* Biomedical engineering online, 2015. **14**(1): p. 66.

207. Zhong, J., et al., *A flexible piezoelectret actuator/sensor patch for mechanical human–machine interfaces.* ACS nano, 2019. **13**(6): p. 7107-7116.

208. Luo, N., et al., *Flexible piezoresistive sensor patch enabling ultralow power cuffless blood pressure measurement.* Advanced Functional Materials, 2016. **26**(8): p. 1178-1187.

209. Zang, S., et al., *A flexible and skin-mountable elastic fiber-based sensor patch for healthcare monitoring.* Biomedical Physics & Engineering Express, 2019. **5**(4): p. 045011.

210. Yamamoto, Y., et al., *Efficient skin temperature sensor and stable gel-less sticky ECG sensor for a wearable flexible healthcare patch.* Advanced healthcare materials, 2017. **6**(17): p. 1700495.

211. Vempati, S., et al., *Electrospinning combined with atomic layer deposition to generate applied nanomaterials: a review.* ACS Applied Nano Materials, 2020. **3**(7): p. 6186-6209.

212. Sophocleous, M. and J.K. Atkinson, *A review of screen-printed silver/silver chloride (Ag/AgCl) reference electrodes potentially suitable for environmental potentiometric sensors.* Sensors and Actuators A: Physical, 2017. **267**: p. 106-120.

213. Yoon, S. and H.-K. Kim, *Cost-effective stretchable Ag nanoparticles electrodes fabrication by screen printing for wearable strain sensors.* Surface and Coatings Technology, 2020. **384**: p. 125308.

214. Maddipatla, D., et al., *A polyimide based force sensor fabricated using additive screen-printing process for flexible electronics.* IEEE access, 2020. **8**: p. 207813-207821.

215. Chang, W.-Y., et al., *A large area flexible array sensors using screen printing technology.* Journal of display technology, 2009. **5**(6): p. 178-183.

216. Hu, Z., et al., *Electro-spraying/spinning: A novel battery manufacturing technology.* Green Energy & Environment, 2024. **9**(1): p. 81-88.

217. Jung, J., et al., *Stretchable/flexible silver nanowire electrodes for energy device applications.* Nanoscale, 2019. **11**(43): p. 20356-20378.

218. Kim, T., et al., *Electrostatic spray deposition of highly transparent silver nanowire electrode on flexible substrate.* ACS applied materials & interfaces, 2013. **5**(3): p. 788-794.

219. Ashby, M., *Selecting the components of composites.* Le Journal de Physique IV, 1993. **3**(C7): p. C7-1595-C7-1600.

220. Popov, V.L., M. Heß, and E. Willert, *Handbook of contact mechanics: exact solutions of axisymmetric contact problems*. 2019: Springer Nature.

221. Blevins, R.D. and R. Plunkett, *Formulas for natural frequency and mode shape.* Journal of Applied Mechanics, 1980. **47**(2): p. 461.

222. Wen, Z., et al., *Principles and Applications of Acoustic Monitoring of Coal Rock Bodies*, in *Creep Effect and Prediction Method of Dynamic Disaster of Surrounding Rock*, Z. Wen, et al., Editors. 2025, Springer Nature Singapore: Singapore. p. 283-334.

223. Yong, Q. and Y. Zhao, *A contactless human vital sign monitoring system using a Doppler radar.* Biomedical Signal Processing and Control, 2025. **110**: p. 108223.

224. Alali, S.A., et al., *Optimized CNN-based denoising strategy for enhancing longitudinal monitoring of heart failure.* Computers in Biology and Medicine, 2025. **184**: p. 109430.

225. Lee, K.-R., et al., *A Wearable Stethoscope for Accurate Real-Time Lung Sound Monitoring and Automatic Wheezing Detection Based on an AI Algorithm.* Engineering, 2025.

226. Chen, H. and W. Gu, *A dual branch feature extraction network for heart sound signal analysis.* Scientific Reports, 2025. **15**(1): p. 27557.

227. Xiong, W., et al., *Multichannel feature fusion network-based technique for heart sound signal classification and recognition.* Expert Systems with Applications, 2025. **273**: p. 126839.

228. Bi, X., et al., *A Systematic Review of Heart Sound Detection Algorithms: Experimental Results and Insights.* IEEE Transactions on Instrumentation and Measurement, 2025. **74**: p. 1-16.

229. Al-Shannaq, M.a.A., et al., *Abnormal heart sound recognition using SVM and LSTM models in real-time mode.* Scientific Reports, 2025. **15**(1): p. 9129.

230. Torabi, Y., S. Shirani, and J.P. Reilly, *Descriptor: Heart and Lung Sounds Dataset Recorded From a Clinical Manikin Using Digital Stethoscope (HLS-CMDS).* IEEE Data Descriptions, 2025. **2**: p. 133-140.

231. Devaki, M., et al. *Real-Time Heart Sound Analysis and Abnormality Detection using Deep Learning Algorithms in a Digital Stethoscope*. in *2025 7th International Conference on Inventive Material Science and Applications (ICIMA)*. 2025.

232. Zhang, B., et al., *JASSNet: Heart and lung sound separation network based on joint attention mechanism and Semi-Supervised learning.* Biomedical Signal

Processing and Control, 2025. **104**: p. 107525.

233. Mendes, J., et al., *Hamman's Sign and Syndrome: A Reminder of Important Clinical Clues.* Pediatric Pulmonology, 2025. **60**(2): p. e27502.

234. Weaver, L. and B. Weaver, *Examining the Cardiovascular and Respiratory Systems of the Ruminant*, in *Performing the Large Animal Physical Examination*. 2025. p. 445-454.

235. Giannini, L., et al. *Multi-Modal Respiratory Monitoring Using SENSIPLUS Chip Bioimpedance Measurements and Acoustic Sensors*. in *2025 IEEE Medical Measurements & Applications (MeMeA)*. 2025.

236. Mao, J.-H., et al., *Machine Learning-Enabled Emotion Recognition by Multisource Throat Signals.* ACS Nano, 2025. **19**(19): p. 18397-18408.

237. Guo, K., Q. Zhang, and D. Wang, *EchoBreath: Continuous Respiratory Behavior Recognition in the Wild via Acoustic Sensing on Smart Glasses*, in *Proceedings of the 2025 CHI Conference on Human Factors in Computing Systems*. 2025, Association for Computing Machinery. p. Article 348.

238. Mohebbi, A., et al., *Cellular Polymer Ferroelectret: A Review on Their Development and Their Piezoelectric Properties.* Advances in Polymer Technology, 2018. **37**(2): p. 468-483.

239. Darabi, A., et al., *Broadband Bending of Flexural Waves: Acoustic Shapes and Patterns.* Scientific Reports, 2018. **8**(1): p. 11219.

240. Wang, W., et al., *Recent Progress of Functional Fiber and Textile Triboelectric Nanogenerators: Towards Electricity Power Generation and Intelligent Sensing.* Advanced Fiber Materials, 2021. **3**(6): p. 394-412.

241. Wang, H.S., et al., *Biomimetic and flexible piezoelectric mobile acoustic sensors with multiresonant ultrathin structures for machine learning biometrics.*

Science Advances. **7**(7): p. eabe5683.

242. Park, D.Y., et al., *Self-Powered Real-Time Arterial Pulse Monitoring Using Ultrathin Epidermal Piezoelectric Sensors.* Advanced Materials, 2017. **29**(37): p. 1702308.

243. Jung, Y.H., et al., *Deep learning-based noise robust flexible piezoelectric acoustic sensors for speech processing.* Nano Energy, 2022. **101**: p. 107610.

244. Jang, J., et al., *A microelectromechanical system artificial basilar membrane based on a piezoelectric cantilever array and its characterization using an animal model.* Scientific Reports, 2015. **5**(1): p. 12447.

245. Festen, J.M. and R. Plomp, *Effects of fluctuating noise and interfering speech on the speech-reception threshold for impaired and normal hearing.* The Journal of the Acoustical Society of America, 1990. **88**(4): p. 1725-1736.

246. Lin, Z., et al., *A Personalized Acoustic Interface for Wearable Human–Machine Interaction.* Advanced Functional Materials, 2022. **32**(9): p. 2109430.

247. Sultana, A., et al., *Energy harvesting and self-powered microphone application on multifunctional inorganic-organic hybrid nanogenerator.* Energy, 2019. **166**: p. 963-971.

248. Lee, S., et al., *A High-Fidelity Skin-Attachable Acoustic Sensor for Realizing Auditory Electronic Skin.* Advanced Materials, 2022. **34**(21): p. 2109545.